

Contents

1	The secrets of nature	1
2	1.1 The Standard Model	2
3	1.1.1 Introduction	2
4	1.1.2 Quantum Field Theory	5
5	1.2 The Glashow-Weinberg-Salam model	9
6	1.2.1 Symmetry Breaking mechanism and Goldston theorem	11
7	1.2.2 Higgs mechanism	12
8	1.3 Beyond the Standard Model	14
9	1.3.1 Limitations of the Standard Model	15
10	1.3.2 Theories beyond the Standard Model	17
11	1.4 Conclusions	19
2	The ILC	21
12	2.1 To a linear lepton collider	22
13	2.1.1 Advantages of a linear lepton collider	22
14	2.1.2 Future linear lepton collider	24
15	2.2 The ILC machine	24
16	2.2.1 Baseline design	25
17	2.2.2 Machine design and beam parameters	25
18	2.2.3 Beam backgrounds	28
19	2.3 The ILC detectors concept	29
20	2.3.1 Overview of the two experiments	29

23	2.3.2 Particle flow algorithm	30
24	2.3.3 The ILD detector	31
25	2.4 Conclusions	37
26	3 Physics at the ILC	39
27	3.1 Potential studies	40
28	3.2 Higgs physics	41
29	3.2.1 Production of the Higgs at the ILC	42
30	3.2.2 Decays of the Higgs	44
31	3.2.3 Higgs studies	44
32	3.3 Analysis of simulated data	45
33	3.4 Simulation set-up	45
34	3.4.1 Signal	46
35	3.4.2 Background processes	47
36	3.4.3 Event reconstruction	47
37	3.4.4 Event selection	47
38	4 Double-sided VXD: PLUME	49
39	4.1 The ILD vertex detector specifications	50
40	4.1.1 Physics requirements	50
41	4.1.2 Layout of the vertex detector	52
42	4.2 PLUME	54
43	4.2.1 Design and goals	55
44	4.2.2 Prototypes	56
45	4.2.3 Perspectives	57
46	4.3 Integration of CMOS sensors	59
47	4.3.1 Charges creation and signal collection	60
48	4.3.2 Pros and cons of the technology	61
49	4.3.3 Signal processing	62
50	4.3.4 State of the art in high energy physics	66

51	5 Basic assessments	69
52	5.1 PLUME assembly procedures	70
53	5.1.1 Module and ladder assembly	70
54	5.1.2 Visual inspections	72
55	5.2 Electrical validation	73
56	5.2.1 Auxiliary board	73
57	5.2.2 Smoke test	75
58	5.2.3 JTAG communication	78
59	5.3 Noise measurements	79
60	5.3.1 Characterisation bench	79
61	5.3.2 Threshold scan	81
62	5.3.3 Noise measurements	84
63	5.4 Conclusions	86
64	6 Deformation studies of a ladder under the test beam	89
65	6.1 Test beam of the full complete PLUME ladder at CERN	90
66	6.1.1 Test beam facility and beam test set-up	90
67	6.1.2 Cartesian coordinate systems	90
68	6.1.3 Measurements	91
69	6.2 Spatial resolution studies	93
70	6.2.1 Normal incidence track	93
71	6.2.2 Ladder tilted in one direction	97
72	6.3 Benefits of double-sided measurement	105
73	6.3.1 Spatial resolution with mini-vectors	106
74	6.3.2 Angular resolution	107
75	6.4 Conclusions	109

76	7 Determination of the material budget	113
77	7.1 Preparation of the test beam	114
78	7.1.1 Measurements and telescope configuration	114
79	7.1.2 Acquisition system	117
80	7.1.3 experimental set-up	119
81	7.1.4 Software analysis chain	120
82	7.2 Measuring the radiation length	121
83	7.2.1 Introduction	121
84	7.2.2 Motivation	122
85	7.2.3 The DESY II test beam facility	122
86	7.3 Analysis	123
87	Acronyms	125
88	Bibliography	129

₈₉ **List of Figures**

90	1.1	Summary of the Standard Model particles with their interactions[44].	2
91	1.2	Scalar potential: ADD A GOOD CAPTION.	15
92	2.1	Schematic layout of the International Linear Collider (ILC).[9]	25
93	2.2	Representation of the bunch structure at the ILC. One bunch 94 train is made of 2625 bunch crossings and lasts 0.95 ms. Each 95 bunch crossing is spaced out by 337 ns. Two bunch trains are 96 of 0.2s apart from each other.[34]	27
97	2.3	Overview of the two detectors designs at the ILC. The figure a 98 represents the SiD design while the figure b shows the ILD 99 approach.[10]	29
100	2.4	Two different approaches for calorimetry. On the left is the tra- 101 ditional calorimetry method used on most of the experiments, 102 the right one is the particle flow approach for calorimetry. 103 The particle track is taken into account to calculate the jet 104 energy.[24]	31
105	2.5	Quadrant view of the ILD detector concept with its subdetec- 106 tor system [10]	32
107	3.1	Feynman diagrams of the main Higgs production at the ILC[5][45].	42
108	3.2	The cross section production of the Higgs boson with a mass 109 of 125 GeV[5].	43
110	3.3	The Higgs branching ratio with the branching ratio uncertain- 111 ties for the Higgs mass varying from 80 to 200 GeV[14].	43
112	3.4	Mass-coupling relation of the Higgs boson to the particles de- 113 fined in the standard model[45].	44

114	4.1	Overview of the two vertex detector option for the ILC. On the left, it is made of five single sided layers, whereas the right one represents three double-sided layers.	52
117	4.2	Side view (transversal and longitudinal) of the PLUME mechanical structure.	55
119	4.3	Microscopical view of the silicon carbide foam structure.	56
120	4.4	Front view of the ladder version-1 made in 2010 in its holding box. On the left, there is the connector to the output board servicing; on the right a connection to blow air on the module. As this version was not made with a mirrored design, the flexible cables are not entirely overlapping and the SiC foam can be seen (in black here).	57
126	4.5	Picture of the first mirrored module made with aluminum traces. The cable width is adjusted to the size of the sensor.	58
128	4.6	Drawing of MAPS structure representing the different layers of the sensor and the path of charge carriers in the epitaxial layer.	61
131	4.7	Two different architectures of pixel.	63
132	4.8	Parallel column readout.	64
133	4.9	Principle of the zero suppression logic.	65
134	4.10	Plots representing the efficiency, the fake hit rate per pixel and the spatial resolution as a function of the discriminator threshold.	66
137	4.11	Block-diagram and a picture of the MIMOSA-26	67
138	4.12	Pictures of the STAR vertex detector and an ULTIMATE chip	68
139	5.1	Drawing of the ladder assembly. The modules are first placed on the jigs, sensors facing the grooves 5.1a, then the foam and the bate are glued between the two modules 5.1b.	71
142	5.2	Visualisation of the alignment. The distance between the two edges is $\sim 51 \mu\text{m}$	72
144	5.3	Picture taken with a microscope showing wire-bonds crashed due to a falling cable. Some of the wire-bonds are in contact leading to a shortcut and a non-functional module.	73
147	5.4	Sketch of the PLUME connection.	76

148	5.5	Picture of a aluminum mirrored module with the points of measurement for V_{DD_D} , V_{DD_A} and V_{clp}	76
150	5.6	MIMOSA-26 output from oscilloscope. The top yellow line corresponds to the clock, the blue line below to the marker (which last 4 clock cycles), and the green and purple line are the data output containing the hit information	78
154	5.7	Matrix response for the discriminators half activated.	80
155	5.8	Matrix response in discriminator mode, where all the discriminators are opened. On the right of the matrix, one line is not working correctly and some pixels are never activated	81
158	5.9	Matrix response in discriminator mode, where all the discriminators are closed. One line of pixels is always activated, as well as few pixels in the same column. This will increase the fake hit rate of the sensor.	82
162	5.10	Pixels response of a threshold scan around the middle-point of discriminators for a sub-matrix.	83
164	5.11	Noise performances of a sub-matrix for the discriminators and the pixel array output. The temporal noise is plotted on the left plot, whereas the fixed pattern noise is represented on the right plot.	83
168	5.12	Accumulation of 10k events at a thresholds of 5 times the noise acquired in the dark.	84
170	5.13	Accumulation of 10k events at a thresholds of 5 times the noise with ^{55}Fe radiation source.	85
172	5.14	Results of the fake hit rate measurement for a threshold three times bigger than the noise. The top left plot represents a raw picture of the million events accumulated over the whole matrix. The top right one is the distribution of the number of pixels hit per event. The bottom left plot is the fake hit rate per pixel distribution, while the bottom right one is the fake hit rate relative to the average rate distribution.	86
179	5.15	Distribution of the fake hit rate per pixel.	87
180	6.1	Drawing of the laboratory coordinates.	91
181	6.2	Top view sketches of the test beam configuration for different ladder positions: 6.2a is for normal incidence, 6.2b and 6.2c are for tilted ladder.	92

184	6.3	Residual distributions in the u and v directions for the middle telescope planes.	94
185			
186	6.4	Results of the DUT alignment: 6.4a is the residual ΔU as a function of the hit position on the v -direction, 6.4b is the residual ΔV as a function of the hit position on the u -direction, 6.4c is the residual ΔU as a function of the hit position on the same direction, 6.4d is the same plot for the other direction, 6.4e and 6.4f are the residuals distributions in the two directions.	96
187			
188			
189			
190			
191			
192			
193	6.5	Distribution of the residuals obtained for the front sensor with a tilt of 36° : 6.5a $\Delta u = f(v_{hit})$, 6.5b $\Delta v = f(u_{hit})$, 6.5c $\Delta u = f(u_{hit})$, 6.5d $\Delta v = f(v_{hit})$, 6.5e distribution of the residual Δu and 6.5f distribution of the residual Δv	98
194			
195			
196			
197	6.6	Distribution of the residuals obtained for the back sensor with a tilt of 36° : 6.6a $\Delta u = f(v_{hit})$, 6.6b $\Delta v = f(u_{hit})$, 6.6c $\Delta u = f(u_{hit})$, 6.6d $\Delta v = f(v_{hit})$, 6.6e distribution of the residual Δu and 6.6f distribution of the residual Δv	99
198			
199			
200			
201	6.7	Results of the mechanical survey of each side of the PLUME mechanical prototype.	100
202			
203	6.8	Side view of the sensor's deformation.	101
204	6.9	Profile of the scatter plot showing the track-hit residual in the u -direction as a function of the hit position on the plane for the same direction: 6.9a is the profile of the front plane and 6.9b is the profile of the back plane. Both profiles were fitted with a sum of Legendre polynomials up to the eleventh order.	102
205			
206			
207			
208			
209	6.10	Results of the alignment after applying the Legendre polynomials correction and taking into account the angle of the incoming particles for the front sensor: ?? $\Delta u = f(u_{hit})$ and 6.10d distribution of the residuals.	104
210			
211			
212			
213	6.11	Results of the alignment after applying the Legendre polynomials correction and taking into account the angle of the incoming particles for the back sensor: ?? $\Delta u = f(u_{hit})$ and 6.11d distribution of the residuals.	105
214			
215			
216			
217	6.12	Principle of the mini-vector. The two hits (in red) on the planes x_1 and x_2 are connected and the intersection on virtual intermediate plane x_m is then determined. The blue points represents the track extrapolated through the DUT.	106
218			
219			
220			

221	6.13	Residual distribution for both side of the ladder in the <i>u</i> -direction	107
222	6.14	Residual distribution of the mini-vector measured on the intermediate plane.	108
223	6.15	Distribution of the angle between the tracks direction and the mini-vectors direction.	109
224	6.16	Minimum distance between the cluster projected on one side to the position of the cluster of this side.	110
225	6.17	Minimum distance between the cluster projected on one side to the position of the cluster of this side.	111
226	7.1	Estimation of the resolution measured at the DUT position as a function of the distance between two telescope planes of the same arm. The blue lines is the results for six planes, whereas the red line is for four planes. The dashed lines are the maximal distance between two planes due to the rail limitation of the telescope frame.	116
227	7.2	TCAD model of the mechanical structure designed for the test beam in April. The ladder is hold on a circular frame fixed to a PI rotation stage, mounted onto a XY-table.	118
228	7.3	Schematic of the test beam set-up. The PMTs are used for triggering. The clock and marker are read from only one sensor, here it comes from one PLUME sensor.	119
229	7.4	Test beam set-up.....	120
230	7.5	Schematic layout of the DESY-II test beam facility[16].	122
231	7.6	Rate for different momentum and with different converter targets[16].	123

²⁴⁶ List of Tables

247	1.1	Summary of the 12 types fermions. L is a quantum number 248 associated to the leptons. Its value is 1 for leptons and -1 249 for anti-leptons. B is a quantum number associated to the 250 baryons. It is equal to 1 for a baryon and to -1 for an anti- 251 baryon. [39]	4
252	1.2	Summary of the interactions and the bosons defined in the 253 Standard Model[39]. The range corresponds to the distance 254 on which the interaction is still effective. As the gravitational 255 interaction is not part of the SM, the graviton is not included 256 in this table.	5
257	2.1	Parameters aimed for the silicon tracker using micro-strips 258 sensors.	34
259	3.1	Summary of the major processes that will be studied at the 260 ILC for different energies[6].	41
261	3.2	Cut flow chart with different cuts applied.	48
262	4.1	Estimation of the material budget for the different prototypes 263 of the PLUME ladder.	58
264	6.1	Fit results of the scatter plot $\Delta U = f(U)$ for Legendre poly- 265 nomials order and the residual obtained on each side of the 266 PLUME ladder.	103
267	6.2	Alignment results for different angles before and after using 268 the correction based on Legendre polynomials.	105
269	7.1	Estimation of the resolution measured σ_{res} at the DUT posi- 270 tion for a telescope with four planes and six planes.	115

²⁷¹ Todo list

²⁷² Keep going to introduce all the quantum numbers	2
²⁷³ Conservation laws and invariance	4
²⁷⁴ Subsubsection: symmetries	5
²⁷⁵ Add details on the QED: coupling...	6
²⁷⁶ Rephrase the section title	9
²⁷⁷ Yukawa couplings with fermions	14
²⁷⁸ Paper on ILC	24
²⁷⁹ Paper on CLIC	24
²⁸⁰ Check the table and values....	34
²⁸¹ H decays at LHC: bb, WW, tau tau, gamma gamma, gg and ZZ	44
²⁸² Not clear enough	44
²⁸³ Cooling system, integration time, radiation tolerance, electromagnetic interference	54
²⁸⁵ REF: EUDAQ	54
²⁸⁶ REF Joel paper	55
²⁸⁷ Figure: Rolling shutter	64
²⁸⁸ Citation to a glob-top paper	70
²⁸⁹ Draw a better figure	91
²⁹⁰ REF TO EUTEL	120

²⁹¹ **Chapter 1**

²⁹² **The secrets of nature**

²⁹³ This chapter attempts to understand the world around us using a mathematical framework which describes the matter and its interaction. Firstly, ²⁹⁴ the laws that rule the Universe will be presented. Then, it will focus on ²⁹⁵ the mathematical framework itself with the description of three interactions: ²⁹⁶ the electromagnetic interaction (EM), the weak and the strong interaction. ²⁹⁷ Afterward, a framework that unifies the EM and weak interaction, as well ²⁹⁸ as the spontaneous symmetry breaking will be studied. Finally, the limits of ²⁹⁹ this theory and the possible solution to overcome these issues will be tackled. ³⁰⁰

³⁰¹ **Contents**

³⁰² 1.1 The Standard Model	³⁰³	³⁰⁴ 2
³⁰⁵ 1.1.1 Introduction	³⁰⁶	³⁰⁷ 2
³⁰⁸ 1.1.2 Quantum Field Theory	³⁰⁹	³¹⁰ 5
³¹¹ 1.2 The Glashow-Weinberg-Salam model	³¹²	³¹³ 9
³¹⁴ 1.2.1 Symmetry Breaking mechanism and Goldston theorem	³¹⁵	³¹⁶ 11
³¹⁷ 1.2.2 Higgs mechanism	³¹⁸	³¹⁹ 12
³²⁰ 1.3 Beyond the Standard Model	³²¹	³²² 14
³²³ 1.3.1 Limitations of the Standard Model	³²⁴	³²⁵ 15
³²⁶ 1.3.2 Theories beyond the Standard Model	³²⁷	³²⁸ 17
³²⁹ 1.4 Conclusions	³³⁰	³³¹ 19

³¹⁷ 1.1 The Standard Model

³¹⁸ 1.1.1 Introduction

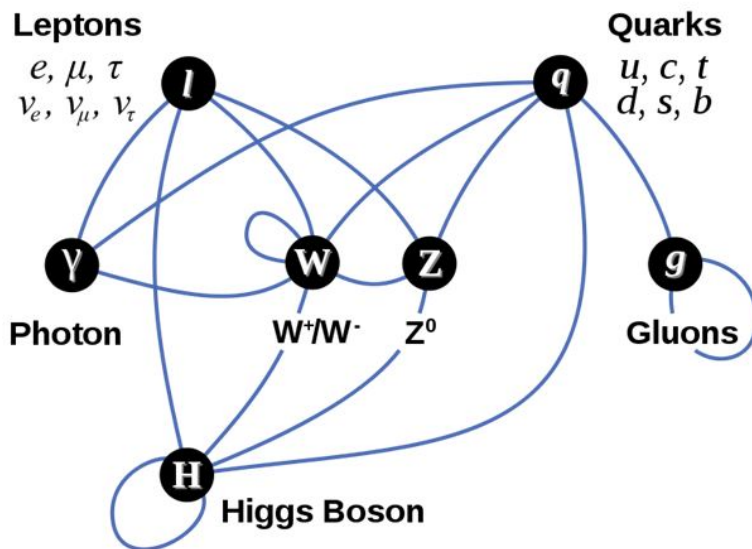


Figure 1.1 – Summary of the Standard Model particles with their interactions[44].

³¹⁹ The Standard Model (SM) is a theory that describes the elementary structure of the matter. It is one of the most successful achievements in modern ³²⁰ physics. The elegant theoretical framework of the SM is able to explain experimental results but is also able to predict a wide variety of phenomena. ³²¹ It depicts the interactions between the fundamental constituents of matter, called elementary particles. A quantum formalism describes an elementary particle with a set of quantum numbers, that are the spin, or the intrinsic angular momentum, the parity P, the electric charge...³²² The distinction between the 'matter' particles and the 'force carrier' particles is done thanks to the ³²³ quantum numbers.³²⁴

Keep going to introduce all the quantum numbers

³²⁵ ³²⁶ ³²⁷ ³²⁸ The half-integer spin particles obey to the Fermi-Dirac statistics and are

submitted to the Pauli exclusion principle: they can not occupy the same quantum state at the same time. These particles are called fermions. They are the constituents of the matter and are to the number of twelve.

The fermions are divided into two categories: the leptons and the quarks. The leptons are to the number of six: three charged particles and three neutral particles called neutrino. The first fundamental particle discovered in particle physics was the electron (e^-) at the end of the 19th century. The two other charged leptons were discovered in 1937 for the muon (μ) and in 1975 for the tau (τ). Three neutrinos are associated to the three flavored leptons: the electron neutrino (ν_e) discovered in 1953, the muon neutrino (ν_μ) in 1962[19] and the tau neutrino (ν_τ) discovered in 2000[13].

The quarks are to the number of six. They can not be found alone in nature. They are carrying a quantum number: the color. The color quantum numbers are green, blue and red (and the anti-color associated). They are always in a bounded state to form composite particles that are colorless and are called hadrons. A quark and an anti-quark form an integer spin composite particle, called a meson. Three quarks bounded together are called baryons. The most known baryons are the proton and the neutron. They are made of the up quarks (u) and the down quarks (d). The other quarks were discovered in the second half of the 20th century. The strange quark (s) was discovered in 1968, followed by the charm quark (c) in 1974. Then, the bottom quark or beauty quark (b) was discovered in 1977. The last quark discovered was the top quark (t) in 1995.

The fermions are thus divided into three categories which depend on the mass of the particle. They are called generations. The first generation of particles is composed of the electron, the electron neutrino, the u and d quarks. They form the ordinary matter. The two other generations are particles found in cosmic rays or in collisions with accelerators. All the fermions and their properties are summarised in the table 1.1.

The second kind of particles are integer spins particles and are called bosons or gauge bosons. They follow the Bose-Einstein statistics. Contrary to the fermions, the bosons are not limited to a single occupancy of the same state. The bosons are the mediators of the fundamental interactions.

The EM is mediated by the photon γ , a massless and chargeless particle of spin 1. The EM is responsible for the interaction between two charged particles. The weak interaction which is responsible for the β radioactive decay (a nucleon decays into another one with the emission of a lepton and a neutrino). The gauge bosons associated with the weak interaction are the neutral electrical charged boson Z^0 , and two electrical charged one: the W^+ and W^- bosons. The strong interaction is mediated by eight gauge bosons:

Type	Family	Particle	L	B	Q_e	Mass (MeV)
Leptons	1 st	e	1	0	-1	0.511
		ν_e	1	0	0	$< 2 \times 10^{-6}$
	2 nd	μ	1	0	-1	105.66
		ν_μ	1	0	0	$< 2 \times 10^{-6}$
	3 rd	τ	1	0	-1	1.78×10^3
		ν_τ	1	0	0	$< 2 \times 10^{-6}$
Quarks	1 st	u	0	1	2/3	$2.3^{+0.7}_{-0.5}$
		d	0	1	-1/3	$4.8^{+0.5}_{-0.3}$
	2 nd	s	0	1	-1/3	95 ± 5
		c	0	1	2/3	$1.275 \times 10^3 \pm 2.5$
	3 rd	b	0	1	-1/3	$4.66 \times 10^3 \pm 30$
		t	0	1	2/3	$173.21 \times 10^3 \pm 511 \pm 711$

Table 1.1 – Summary of the 12 types fermions. L is a quantum number associated to the leptons. Its value is 1 for leptons and -1 for anti-leptons. B is a quantum number associated to the baryons. It is equal to 1 for a baryon and to -1 for an anti-baryon. [39]

370 the gluons. The cohesion of the hadrons and the cohesion of the atom's nu-
 371 cleus is lead by the strong interaction. The last force is the gravitational
 372 interaction but it is not included into the SM. Trying to find a framework
 373 where the equation of the general relativity used to describe the macroscopic
 374 world and the equation of the quantum mechanics describing the microscopic
 375 world is a difficult challenge. A quantum theory intends to associate a bo-
 376 son to the gravitational force. This boson is a spin 2 particle and is called
 377 graviton.

378 The Higgs boson (H) is a particle predicted by the SM and has been
 379 discovered in 2012 at the Large Hadron Collider (LHC). It is the gauge boson
 380 of the Higgs mechanism. This mechanism is the mass generator of particles
 381 and is presented in section 1.2.2.

382 The table 1.2 summarises the different bosons of the SM.

Conservation
laws and invari-
ance

383 The particle physics is based on the conservation laws as well as the
 384 invariance. The invariance means that the physics is the same on every
 385 point of the Universe. For example, the speed of light is always $\sim 3.0 \text{ m.s}^{-1}$.

Force	Gauge bosons	Mass (GeV/c^2)	Electric charge	Range
Electromagnetic	γ	0	0	∞
Weak	Z^0	91.1876 ± 0.0021	0	10^{-18} m
	W^\pm	80.3980 ± 0.0250	± 1	
Strong	g (8 gluons)	0	0	10^{-15} m
	H	125 GeV	0	

Table 1.2 – Summary of the interactions and the bosons defined in the Standard Model[39]. The range corresponds to the distance on which the interaction is still effective. As the gravitational interaction is not part of the SM, the graviton is not included in this table.

386 1.1.2 Quantum Field Theory

387 The mathematical basis of the SM is the Quantum Field Theory (QFT). All
 388 the interactions are described by the gauge group:

$$SU_C(3) \otimes SU_L(2) \otimes U_Y(1). \quad (1.1)$$

389 The gauge theory is invariant under a continuous set of local transfor-
 390 mation. Taking the gauge symmetries and the least action into account,
 391 physicists were able to set up equations that describe the dynamic of the
 392 interactions by a Lagrangian. The steps to build Lagrangian for the three
 393 forces and the unification of the EM and weak interactions are going to be
 394 presented.

395 Subsubsection:
 symmetries

396 Quantum Electrodynamics

397 The Quantum Electrodynamics (QED) is the QFT that combines the elec-
 398 tromagnetism and the quantum mechanics formalisms to describe the inter-
 399 action thanks to a relativistic Lagrangian. As the charge Q_e of the electron
 400 is invariant on every part of the Universe, the QED Lagrangian should be
 401 invariant under some transformations too. The $U(1)$ gauge group is a unitary
 402 group of one dimension which is invariant under space transformations.

403 Firstly, the Dirac Lagrangian \mathcal{L}_{Dirac} for a free fermion with a mass m is:

$$\mathcal{L}_{Dirac} = \bar{\Psi}(x) (i\gamma^\mu \partial_\mu - m) \Psi(x), \quad (1.2)$$

404 with $\Psi(x)$ the spinor field describing the fermion and γ^μ are the Dirac
405 matrices. The Lagrangian is invariant under global $U(1)$ transformation:

$$\begin{aligned}\Psi(x) &\rightarrow \Psi'(x) = e^{-i\alpha}\Psi(x) \\ \bar{\Psi}(x) &\rightarrow \bar{\Psi}'(x) = e^{i\alpha}\bar{\Psi}(x)\end{aligned}\tag{1.3}$$

406 The corresponding local symmetry is:

$$\begin{aligned}\Psi(x) &\rightarrow \Psi'(x) = e^{-i\alpha(x)}\Psi(x) \\ \bar{\Psi}(x) &\rightarrow \bar{\Psi}'(x) = e^{i\alpha(x)}\bar{\Psi}(x)\end{aligned}\tag{1.4}$$

407 Although the mass term of the Lagrangian in the equation 1.2 stays in-
408 variant under the local symmetry, the term containing a partial derivative is
409 not anymore. A gauge field A_μ has to be added to the derivative to keep it
410 invariant under local gauge transformation. The covariant derivative will be
411 then:

$$D_\mu\Psi(x) = (\partial_\mu - iQ_eA_\mu)\Psi(x)\tag{1.5}$$

412 The gauge field is not yet a dynamic field. To get a physical gauge field,
413 a kinetic term should be added to the equation. This gauge invariant term
414 that includes derivative from the A_μ field is:

$$F_{\mu\nu} = \partial_\mu A_\nu - \partial_\nu A_\mu\tag{1.6}$$

415 The Lagrangian, which is local invariant, is the one that describes the
416 QED:

$$\mathcal{L}_{QED} = \bar{\Psi}(x)(i\gamma^\mu D_\mu - m)\Psi(x) - \frac{1}{4}F_{\mu\nu}(x)F^{\mu\nu}(x)\tag{1.7}$$

417 A mass term $m A_\mu A^\mu$ for the field A_μ is missing because it is not gauge in-
418 variant. That consideration matches to the fact that the photon is a massless
419 boson.

Add details on 420
the QED: cou-
pling...

421 **Weak interaction**

422 In 1930, Pauli assumed that the continuous energy spectrum of the electron in
 423 the β decay could be explained by the existence of a new particle to respect
 424 the principle of energy conservation. It is a light particle, which does not
 425 interact so much with matter.

426 After the discovery of the neutron by Chadwick in 1932, Fermi wrote a
 427 theory on weak interaction to explain the β decay. [20] He postulated that
 428 the neutron is decaying into a proton by emitting an electron and a light
 429 neutral particle, called neutrino. In analogy to the electromagnetism, he
 430 proposed a current-current Lagrangian to describe the β decay.

$$\mathcal{L}_{weak} = \frac{G_F}{\sqrt{2}} (\bar{p}\gamma_\mu n) (\bar{e}\gamma_\mu\nu) \quad (1.8)$$

431 where the G_F is the Fermi constant $G_F = 1.166 \cdot 10^{-5} GeV^{-2}$.

432 Nevertheless, the non-relativistic limit leads to an incomplete theory. The
 433 interaction considered with a 2-components spinor transforms a proton into
 434 a neutron without changing the position, the spin or the parity. However,
 435 Lee and Yang have postulated in 1956 that the weak interactions violate
 436 the parity after analysing the decays of the τ and θ particles [33]. The Wu
 437 experiment [47] confirmed this hypothesis in 1957 by studying the decay of
 438 ^{60}Co .

439 The Fermi interaction was modified by Feynman and Gell-Mann[21] to a
 440 $V - A$ theory¹. The vector current is now subtracted by an axial vector
 441 current. For example, the neutrino current is replaced by:

$$\begin{aligned} \bar{e}(x)\gamma_\mu\nu &\rightarrow \bar{e}\gamma_\mu(1 - \gamma_5)\nu \\ &= \bar{e}\gamma_\mu\nu - \bar{e}\gamma_\mu\gamma_5\nu \end{aligned} \quad (1.9)$$

442 It was established that the weak current has the form $V - A$ instead
 443 of $V + A$. The weak interaction is only coupling left-handed particles and
 444 right-handed anti-particles.

445 The lagrangian describing the weak interactions can be written as a cur-
 446 rents interaction:

$$\mathcal{L}_{weak} = -\frac{G_F}{\sqrt{2}} J^\mu J_\mu^\dagger \quad (1.10)$$

¹ V stands for vector and A for axial-vector

⁴⁴⁷ and J^μ is a combination of leptonic and hadronic currents.

⁴⁴⁸ Contrary to the QED, the weak interaction obeys to a non-Abelian sym-
⁴⁴⁹ metry group², the SU(2) symmetry group. The matter field could be repre-
⁴⁵⁰ sented as a doublet Ψ_L and a singlet Ψ_R of this group.

$$\Psi_L = \begin{pmatrix} \nu_{eL} \\ e_L \end{pmatrix}, \quad \Psi_R = e_R \quad (1.11)$$

⁴⁵¹ The generators of the group are the three Pauli matrices σ_i , associated
⁴⁵² with a gauge field W_μ^i . The bosons of the weak interactions are the W^\pm and
⁴⁵³ Z .

⁴⁵⁴ As the left-handed leptons are combined into a doublet, a quantum num-
⁴⁵⁵ ber called weak isospin (I_3) is associated with them. The charged leptons
⁴⁵⁶ have a weak isospin $I_3 = \frac{-1}{2}$ and for the neutrinos $I_3 = \frac{1}{2}$. Concerning the
⁴⁵⁷ gauge bosons W^\pm and Z , the weak isospin is respectively $I_3 = \pm 1, 0$.

⁴⁵⁸ Quantum Chromodynamics

⁴⁵⁹ The Quantum Chromodynamics (QCD) is the quantum field theory of the
⁴⁶⁰ strong interaction. In this model, the interaction is due to an $SU(3)$ gauge
⁴⁶¹ group. It produces 8 gauge fields called gluons. The spinors of this theory
⁴⁶² are the six quarks that form a triplet with respect to the gauge symmetry.

⁴⁶³ The $SU(3)$ gauge group is a group of $9 - 1 = 8$ real parameters and of 8
⁴⁶⁴ generators. Those generators are the Gell-Mann matrices. The normalised
⁴⁶⁵ generators are defined by:

$$T^a = \frac{1}{2} \lambda^a \quad (1.12)$$

⁴⁶⁶ The structure constant f^{abc} can be expressed as:

$$if^{abc} = 2Tr([T^a, T^b]T^c) \quad (1.13)$$

⁴⁶⁷ Each of them is considered as a triplet state with respect to the $SU(3)$
⁴⁶⁸ group:

²A group is non-Abelian when the elements of the group are not commutating.

$$q_i = \begin{pmatrix} q_i^1 \\ q_i^2 \\ q_i^3 \end{pmatrix} \quad (1.14)$$

469 where q_i are the six quarks. These quarks can appear in three different
 470 states, called color and that are named red, blue and green.

471 The local gauge symmetry $U(1)$ should be included into the $SU(3)$ group.
 472 The gauge field A_μ can be introduced in the group:

$$A_\mu = g_S A_\mu^a \frac{\lambda^a}{2} \quad (1.15)$$

473 with $a = 1, \dots, 8$ and corresponds to the 8 gluons. A mass term $m_g A_a^\mu A_\mu^a$
 474 would not be gauge invariant, it implies that the gluons have to be massless.

475 The covariant derivative is then:

$$\begin{aligned} D_\mu &= \partial_\mu - iA_\mu \\ &= \partial_\mu - ig_S A_\mu^a \frac{\lambda^a}{2} \end{aligned} \quad (1.16)$$

476 The QED field $F_{\mu\nu}$ is not gauge invariant in QCD. Nevertheless, an ad-
 477 ditional term to obtain gauge invariant field tensor can be introduced:

$$G_{\mu\nu}^a = (\partial_\mu A_\nu^a - \partial_\nu A_\mu^a) + g_S f^{abc} A_\mu^b A_\nu^c \quad (1.17)$$

478 Finally, the QCD Lagrangian is given by:

$$\mathcal{L} = \sum_{i=1}^6 \bar{q}_i (i\gamma^\mu D_\mu - m_i) q_i - \frac{1}{4} G_{\mu\nu}^a G_a^{\mu\nu} \quad (1.18)$$

479 1.2 The Glashow-Weinberg-Salam model

480 Late 1960, a model of unification was postulated by Glashow, Weinberg,
 481 and Salam to describe the electroweak interaction (EW). The theory rests
 482 on a $SU(2)_L \otimes U(1)_Y$ symmetry group. It is the simplest group which con-
 483 serves the properties of EM charge conversion and parity violation of weak
 484 interaction.
 485

Rephrase the
section title

For the EW unification, the $U(1)_{EM}$ symmetry group describing the EM has to be rewritten. As the fermions are considered by left-handed doublets and right-handed singlets, the $U(1)_{EM}$ breaks the gauge invariance. The weak isospin group $SU(2)_L$ is combined with the EM charge to create the hypercharge give by the Gell-Mann-Nishijima relation:

$$Q = I_3 + \frac{1}{2}Y \quad (1.19)$$

The I_3 term is the third component of the weak isospin. With the introduction of the hypercharge, the EM gauge invariance is conserved.

The EW Lagrangian is:

$$\mathcal{L}_{EW} = \mathcal{L}_{YM} + \mathcal{L}_{fermions} ?? \quad (1.20)$$

The first term \mathcal{L}_{YM} is the Yang-Mills Lagrangian that describes the bosons gauges interactions (kinetic term + interaction between bosons). It has the form below:

$$\mathcal{L}_{YM} = -\frac{1}{4}\mathbf{W}_{\mu\nu}^a\mathbf{W}^{a\mu\nu} - \frac{1}{4}\mathbf{B}_{\mu\nu}\mathbf{B}^{\mu\nu} \quad (1.21)$$

With

$$\mathbf{W}_{\mu\nu} = \partial_\mu \mathbf{W}_\nu - \partial_\nu \mathbf{W}_\mu - ig[\mathbf{W}_\mu, \mathbf{W}_\nu] \quad (1.22)$$

$$\mathbf{B}_{\mu\nu} = \partial_\mu \mathbf{B}_\nu - \partial_\nu \mathbf{B}_\mu \quad (1.23)$$

In the equation 1.22, $\mathbf{W}_\mu = \sum W_\mu^i \sigma^i / 2$ is a vector of three gauge fields associated to $SU(2)_L$ and σ^i are the Pauli matrices. The term $[\mathbf{W}_\mu, \mathbf{W}_\nu]$ is associated to the interactions between the gauge fields. In the equation 1.23, \mathbf{B}_μ is the only gauge field associated to the $U(1)_Y$.

The Lagrangian describing the fermions field is given by:

$$\mathcal{L}_{fermions} = \bar{\Psi}_L \gamma^\mu D_\mu \Psi_L + \bar{\Psi}_R \gamma^\mu D_\mu \Psi_R \quad (1.24)$$

With $D_\mu \Psi_L = \left(\partial_\mu + ig\mathbf{W}_\mu - i\frac{g'}{2}Y\mathbf{B}_\mu \right) \Psi_L$ and $D_\mu \Psi_R = \left(\partial_\mu - i\frac{g'}{2}Y\mathbf{B}_\mu \right) \Psi_R$

In the equation 1.25, the covariant derivative has two forms. The weak interaction does not allow coupling of the W bosons to right-handed fermions whereas the γ and Z bosons do.

With the EW Lagrangian described above, the gauge bosons are considered as massless fields. The electroweak interaction does not allow a $m\bar{\Psi}\Psi$ term because it does not transform as a scalar under $SU(2)_L \otimes U(1)_Y$. Moreover, the $m^2 \mathbf{W}_\mu \mathbf{W}^\mu$ violates the $SU(2)_L$ gauge invariance of the Lagrangian. The mass terms associated with the physical fields of the gauge bosons are given by spontaneous symmetry breaking via the Higgs mechanism.

1.2.1 Symmetry Breaking mechanism and Goldston theorem

Before introducing the Higgs mechanism, we will study the spontaneous symmetry breaking for a global symmetry. This phenomenon is also seen in phase transitions or laser theory.

Let's consider first the Lagrangian density for a complex scalar field ϕ :

$$\mathcal{L} = \partial^\mu \phi^* \partial_\mu \phi - \mu^2 \phi^* \phi - \lambda(\phi^* \phi)^2 \quad (1.26)$$

The first component of the Lagrangian density corresponds to the kinetic term of a complex scalar field, while the second component is related to a scalar potential. The coefficient μ^2 is a real parameter. Nevertheless, depending on its sign, the potential can take two forms.

If $\mu^2 > 0$, the symmetry is unbroken and the potential has a minimum at $\phi = 0$ which does not degenerate. It describes a particle with a mass μ and a quartic self-coupling. As the transformation $\phi \rightarrow -\phi$ is respected, this solution is a symmetric one.

When $\mu^2 < 0$, there is not a unique ground state for this system but multiple states with the same vacuum energy. The minima is located on a circle of radius:

$$v = \sqrt{\frac{-\mu^2}{2\lambda}} > 0 \quad (1.27)$$

By choosing a particular solution as the ground state, the symmetry gets spontaneously broken.

A parametrisation of the excitations around the ground state is possible by introducing a new field ϕ :

$$\phi(x) = \frac{1}{\sqrt{2}} (v + \rho(x) + i\Theta(x)) \quad (1.28)$$

533 The value v is given by one of the solution from equation 1.32, $\rho(x)$ and
 534 $\Theta(x)$ are real fields.

535 By adding the new field in the equation 1.26, the Lagrangian becomes:

$$\mathcal{L} = \frac{1}{2}(\partial_\mu\rho)^2 + \frac{1}{2}(\partial_\mu\Theta)^2 - \lambda v^2\rho^2 - \lambda v(\rho^3 + \rho\Theta^2) - \frac{\lambda}{4}(\rho^2 + \Theta^2)^2 \quad (1.29)$$

536 The field $\rho(x)$ describes a state of mass $m_\rho = 2\mu^2$, coupled to the massless
 537 field $\Theta(x)$.

538 The field $\Theta(x)$ describes excitations around a direction in the potential.
 539 The excitations are not costing any energy, so they correspond to massless
 540 bosons called Goldstone bosons.

541 1.2.2 Higgs mechanism

542 As we have seen with the Lagrangian of the QED and QCD, the bosons
 543 generated are massless. Nevertheless, the W^\pm and the Z bosons have a mass
 544 and the equation ?? of the EW interaction does not include a mass generator.
 545 The origin of the fermions masses is solved in the SM thanks to the Higgs-
 546 Englert-Brout mechanism [25][18].

547 Lets consider first a doublet of complex scalar fields Φ :

$$\Phi = \begin{pmatrix} \phi^+ \\ \phi^0 \end{pmatrix} \quad (1.30)$$

548 The invariant Lagrangian density under $SU(2)_L \otimes U(1)_Y$ gauge transfor-
 549 mation is:

$$\mathcal{L} = (D^\mu\phi)^\dagger(D_\mu\phi) - V(\phi) \quad (1.31)$$

550 The covariant derivative is the one of $SU(2)_L \otimes U(1)_Y$ given by the equa-
 551 tion 1.25 and represents the kinetic term. The Higgs potential is similar to
 552 the one considered first and has also two solutions depending on the sign

of μ^2 . Let's focus only on the negative solution. There is an infinite set of degenerated states with minimum energy:

$$\phi_0 = \sqrt{\frac{1}{2}} \begin{pmatrix} 0 \\ v \end{pmatrix} \text{ with } v = \sqrt{\frac{-\mu^2}{\lambda}} > 0 \quad (1.32)$$

Let's expand the field Φ around its minima by including a field $h(x)$ which describes quantum fluctuations and three massless Goldstone fields, denoted $\theta^i(x)$:

$$\Phi(x) = e^{i\frac{\sigma_i}{2}\theta^i(x)} \frac{1}{\sqrt{2}} \begin{pmatrix} 0 \\ v + h(x) \end{pmatrix} \quad (1.33)$$

A particular gauge can be defined in a way that the Goldstone fields are absorbed by the physical field of $SU(2)_L \otimes U(1)_Y$. It implies the apparition of mass terms in equation 1.31. First, we are interested in the mass generation mechanism. We consider only on the impact of the new field on the derivative covariant and omit any terms containing h and remove down the partial derivative:

$$\left| \left(i\frac{g}{2}\mathbf{W}_\mu + i\frac{g'}{2}Y\mathbf{B}_\mu \right) \Phi \right|^2 = \frac{1}{8} \left| \begin{pmatrix} gW_\mu^3 + g'B_\mu & g(W_\mu^1 - iW_\mu^2) \\ g(W_\mu^1 + iW_\mu^2) & -gW_\mu^3 + g'B_\mu \end{pmatrix} \begin{pmatrix} 0 \\ v + h(x) \end{pmatrix} \right|^2 \quad (1.34)$$

The charged fields can be expressed as a linear combination of gauge fields:

$$W_\mu^\pm = \frac{W_\mu^1 \mp iW_\mu^2}{\sqrt{2}} \quad (1.35)$$

The eigenstates are rewritten as decorrelated terms representing the neutral fields from the EW symmetry group:

$$Z_\mu = \cos \theta_w W_\mu^3 - \sin \theta_w B_\mu \quad (1.36)$$

$$A_\mu = \sin \theta_w W_\mu^3 + \cos \theta_w B_\mu \quad (1.37)$$

θ_w is the Weinberg angle and represent a bound between the coupling g and g' :

$$\sin \theta_w = \frac{g'}{\sqrt{g^2 + g'^2}} \text{ and } \cos \theta_w = \frac{g}{\sqrt{g^2 + g'^2}} \quad (1.38)$$

571 The equation 1.34 becomes:

$$\begin{aligned} \left| \left(i\frac{g}{2}\mathbf{W}_\mu + i\frac{g'}{2}Y\mathbf{B}_\mu \right) \Phi \right|^2 &= \frac{1}{8} \left| \begin{pmatrix} A_\mu \sqrt{g^2 + g'^2} & gW_\mu^- \\ gW_\mu^+ & -Z_\mu \sqrt{g^2 + g'^2} \end{pmatrix} \right|^2 \\ &= \frac{1}{2} M_Z^2 ZZ^* + \frac{1}{2} M_W^2 W^-W^+ \end{aligned} \quad (1.39)$$

572 With $M_Z = \frac{1}{2}v\sqrt{g^2 + g'^2}$ and $M_W = \frac{1}{2}vg$, the mass of the Z boson and 573 the W^\pm bosons. The mass of the photon is consistent with the expectation 574 and is null.

575 The Higgs mechanism implies the existence of a massive gauge field, the 576 Higgs boson. It is coupled to the other bosons and also to itself. This could 577 be shown by extending the Higgs potential with the field defined in equation 578 1.33:

$$-\lambda v^2 h^2 - \lambda v h^3 - \frac{1}{4} \lambda h^4 \quad (1.40)$$

579 The first term gives the mass of the Higgs boson, $M_H^2 = 2\lambda v^2$, while 580 the second and third terms are the Higgs self-interactions. The Higgs mass 581 can not be predicted by the theory because it is given by a function of the 582 parameter λ , which is one of the free parameters of the SM.

Yukawa cou-
plings with
fermions

583

584 1.3 Beyond the Standard Model

585 The SM constitutes one of the most successful achievements in modern 586 physics. One of its strength is to provide an elegant theoretical framework 587 to describe the known experimental facts about particles, but it is also able 588 to predict the existence of a mechanism to generate the particle masses via 589 the Higgs mechanism. Nevertheless, a lot of mysteries in the Universe are 590 not explained by this theory.

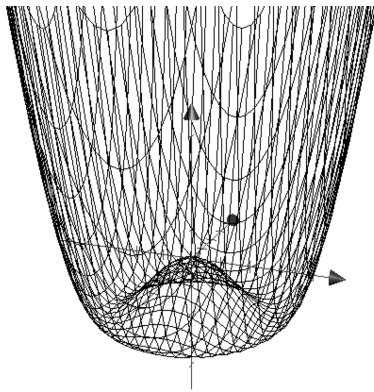


Figure 1.2 – Scalar potential: ADD A GOOD CAPTION.

591 1.3.1 Limitations of the Standard Model

592 Despite the fact that the experimental results are in good agreement with
 593 the SM predictions, this theory does not provide answers to many questions.
 594 The particle physics community tries to unify theories.

595 **Free parameters**

596 Up to 19 free parameters are used in the SM and this theory does not explain
 597 their existence. Even if it is not a major problem for the physics itself, the
 598 particle physics community has a lack of understanding and explaining these
 599 values. The free parameters are:

- 600 • the masses of the nine fermions
- 601 • the coupling constants g and g' of the $U(1)$, $SU(2)$ groups
- 602 • the coupling constant of the strong interaction α_s
- 603 • the mixing angles, as well as the CP-violating phase of the CKM matrix
- 604 • the Higgs boson mass and the v_{ev} parameters that allow CP violation
 in QCD Lagrangian.

606 **Hierarchy problem**

607 The hierarchy problem refers to two main energy scales problem of the SM.

608 First of all, the difference between the energy scale of the SM and the
609 Planck scale is of seventeen orders of magnitude. No "intermediate" physics
610 has been found between the two scales.

611 A second problem occurs while considering the Higgs boson mass. The
612 SM does not predict its mass, but it sets some theoretical bounds with respect
613 to Λ , the energy scale at which the SM is not valid anymore. The theoretical
614 Higgs boson mass is higher than what it should be compared to the EW
615 scale. The Higgs boson interacts with the particles of the SM (fermions, W
616 and Z boson), but it also interacts with itself. Due to the scalar nature of the
617 boson, there are quartic divergences while calculating the loop corrections.
618 The quantum corrections, which take into account the coupling of the Higgs
619 boson, are Λ^2 divergent and lead to a huge Higgs boson mass. To avoid that,
620 delicate cancellations should occur between the quantum corrections. These
621 cancellations are known as the fine-tuning problem.

622 **Gravitation**

623 Although particle physicists are dreaming of a "theory of everything" that
624 will unify the electroweak, strong and gravitational interactions, there is no
625 viable theory to describe the gravity in a quantum point of view to include
626 it in the SM and which would be still valid at a macroscopic scale.

627 **Neutrino mass**

628 The neutrinos defined by the SM are assumed to be exactly massless. Nev-
629 ertheless at the end of the year 1990, the Super Kamiokande experiment had
630 surprising results[22]. The measured flux of solar and atmosphere neutrons
631 was lower than expected. The result was interpreted by an oscillation of neu-
632 trinos between the three leptonic flavors. However, the oscillation is possible
633 only if the neutrino has a mass. That phenomenon could be considered as a
634 proof of physics beyond the SM.

635 **Matter-antimatter asymmetry**

636 As discussed at the beginning of this chapter, the SM defines an equal num-
637 ber of particles and anti-particles. In the case of the Big Bang theory, it is

638 assumed that the matter and antimatter were created in an exactly equal
639 amount, a mechanism has favoured electrons, protons, and neutrons with re-
640 spect to positrons antiprotons and antineutrons. If the amount of matter and
641 antimatter was equal, our Universe would have been completely annihilated.
642 The matter domination could be a local phenomenon with an antimatter
643 surrounding the region. However, the region of contact between matter and
644 antimatter would be a violent place of interaction, which would disturb the
645 cosmic microwave background.

646 An assumption to explain the asymmetry is that the antimatter was pro-
647 duced in an infinity proportion compared to the matter. Hence, the annihi-
648 lation as lead to create a Universe only made of matter. A mechanism which
649 tends to prefer the matter has been observed in the study of the kaon oscilla-
650 tion. This particle is able to transform spontaneously to its own anti-particle
651 and vice-versa. Nevertheless, this transformation is not symmetric: the kaon
652 is slower to turn into an anti-kaon than the inverse transformation.

653 **Dark Matter and dark energy**

654 Several astrophysical observations are indicating that the Universe is made
655 not only of visible matter but also of matter that seems to be invisible to
656 the electromagnetic interaction and is called the dark matter. In 1933, a
657 measurement of the galaxies velocities in the Coma cluster to determine the
658 cluster mass gives a surprising result. The mass was more than two orders
659 of magnitude bigger than the mass of visible stars in the cluster. It was
660 found that the matter of the SM describes only 5% of the Universe content.
661 The rest of the Universe is made of 22% of dark matter and around 73% of
662 dark energy. The neutrinos are possible candidates to dark matter, as they
663 couple to SM matter only via weak interaction, but they cannot account for
664 the entire density of the universe. Nowadays only twelve particles (plus the
665 anti-particles associated) have been observed.

666 **1.3.2 Theories beyond the Standard Model**

667 **Supersymmetry**

668 The Supersymmetry (SUSY) is a QFT, that relates the elementary fermions
669 known to corresponding bosons, called sfermions and the bosons to corre-
670 sponding fermions, called sbosons [43]. The new particles introduced are

671 called super-partners. They have the same mass, the same quantum numbers
 672 but the spin is differing by a half factor. SUSY is a broken symmetry.
 673 This will allow the super-particles to acquire very high masses.

674 SUSY is a good candidate for physics beyond the SM, as it could solve
 675 the hierarchy problem without any fine tuning. For example, the loop contribu-
 676 tions of one particle to the Higgs are cancelled by the loop contributions of
 677 its super-partner. It would be able to provide a framework for the unification
 678 of the three gauge interactions at a GUT scale. The lightest super-particle
 679 is a good candidate for the Dark Matter.

680 Despite it will answer many questions from the SM, there is a lack of
 681 understanding why SUSY is a broken symmetry.

682 Grand unification theory

683 After the success of the electroweak unification, the next step is to include the
 684 strong interaction to build the Grand Unification Theory (GUT), an exten-
 685 sion of the SM. In this framework, the three forces are different manifesta-
 686 tions of a single interaction. It includes the $SU(3)_C \otimes SU(2)_L \otimes U(1)_Y$ symmetry
 687 group into a larger $SU(5)$ group. The quarks and leptons are ordered in left
 688 decuplets and right quintets. The coupling constants are described by only
 689 one parameter. There are 24 mediators, the 12 mediators of the SM plus 6 X
 690 mediators (charge $\pm 4/3$ and 3 colors) and 6 Y mediators (charge $\pm 1/3$ and
 691 3 colors). It predicts the existence of new particles as leptoquarks³, multiple
 692 Higgs bosons and new currents.

693 Unfortunately, the theory is not validated because of its prediction of the
 694 proton lifetime. The first GUT was introduced by Georgi and Glashow in
 695 1974 and predicted the decay of the proton. The actual experimental limit of
 696 the proton lifetime is of 5×10^{32} years, whereas the predicted lifetime defined
 697 by the $SU(5)$ group is one order of magnitude lower. [39]

698 Technicolor

699 The technicolor is a theory that explains the mass generation. Contrary to
 700 the EW symmetry, the masses of particles are not generated by the spon-
 701 taneous symmetry breaking but they are generated by a strong gauge inter-
 702 action. This interaction is strong and confined at the energy that has been
 703 experimentally probed. The approach of the theory avoids the hierarchy
 704 problem induced by the SM.

³Coupling between a lepton and a quark

705 **String theory**

706 The particle physicists have the dream of unifying the forces of the nature
707 to have only one single interaction with four different manifestations. The
708 string theory proposes a framework for the "theory of everything". The basic
709 unit of matter is no more considered as particles but one-dimensional strings
710 of which particles are various vibrational modes.

711 The string theory is a theory of quantum gravity. It tries to unify the
712 gravitation to the quantum Extra dimensions of 10 -11 space-time dimen-
713 sions. Possible explanation for the hierarchy problem.

714 **1.4 Conclusions**

715 Along this chapter, the successes and limits of the SM were discussed. The
716 high energy physics community is trying to study as far as possible the limit
717 of the SM and is also trying to find some proof of new physics beyond the
718 SM. The Large Hadron Collider (LHC) at CERN has permitted in 2012 to
719 point out the existence of a Higgs boson. Nevertheless, the beam structure
720 of the LHC is not efficient enough to perform very precise measurements.
721 Because of the collision between protons, the energy of the collision can't
722 be exactly known. The next chapter deals with a future experiment in high
723 energy physics, where electrons and positrons are used to probe the matter
724 instead of protons and anti-protons.

725 **Chapter 2**

726 **The future of high-energy physics:
727 the International Linear Collider**

728 Since 2008, the LHC is actually the most powerful tool in high-energy physics
729 to have a better understanding of the universe, particularly with the dis-
730 covery in 2012 of a new particle compatible to the boson predicted by the
731 spontaneous symmetry breaking of the SM [3, 12]. Although the LHC is an
732 impressive machine able to reach the highest energy scale of collision available
733 on Earth with a centre-of-mass energy of 13 TeV, the complex environment
734 of the events generated hides the access to some fundamental parameters. To
735 achieve more precise measurements of the Higgs boson, but also to test the
736 validity of the SM and other physics theories introduced in the chapter 1, the
737 high energy physics community has merged on the necessity to build a linear
738 electron-positron collider, that will work as a complementary accelerator to
739 the LHC.

740 This chapter will explain the motivations to invest a huge amount of
741 money in a new great world project. It will present the complementary
742 nature of the lepton and hadron colliders and the main advantages of the
743 lepton collisions will be discussed. After giving an overview of the ILC with
744 its basic design and the experiment models, we will focus on the design of
745 one of the detectors: the International Large Detector (ILD).

746 **Contents**

<small>747</small> 2.1 To a linear lepton collider	22
<small>748</small> 2.1.1 Advantages of a linear lepton collider	22
<small>749</small> 2.1.2 Future linear lepton collider	24
<small>750</small> 2.2 The ILC machine	24

752	2.2.1 Baseline design	25
753	2.2.2 Machine design and beam parameters	25
754	2.2.3 Beam backgrounds	28
755	2.3 The ILC detectors concept	29
756	2.3.1 Overview of the two experiments	29
757	2.3.2 Particle flow algorithm	30
758	2.3.3 The ILD detector	31
759	2.4 Conclusions	37
760		
762		

763 2.1 To a linear lepton collider

764 The most impressive accelerator ever built is located at CERN in Geneva,
 765 Switzerland. It is the world largest particle accelerator, with a circumference
 766 ring of nearly 27 kilometers, straddling the Swiss and French borders. It
 767 is designed to collide two counter rotating beams of protons or heavy ions,
 768 with a possibility to reach centre-of-mass energies of 13 TeV with a high peak
 769 luminosity of $10^{34} \text{ cm}^2\text{s}^{-1}$. The goals of the LHC are to perform further tests
 770 on the SM, search for new forces or produce dark matter candidates. Indeed,
 771 the collider covers a wide energy range at the constituent level while running
 772 at a fixed beam energy. Unfortunately, due to the nature of the particles used,
 773 the experiment can not reach the highest precision measurements needed.

774 Complementary to a discovery machine such as the LHC, a machine to
 775 perform precise measurement should be built: the linear lepton collider.

776 2.1.1 Advantages of a linear lepton collider

777 First of all, during each collision at an hadron collider, only a part of the
 778 total centre-of-mass energy is available for the process evolved, therefore the
 779 initial four-vector momentum is not known. By colliding leptons, which
 780 are structureless objects, the full centre-of-mass energy is available for the
 781 elementary process. The initial four-vector momentum of an interaction is
 782 exactly known, hence the event can be fully reconstructed.

783 Secondly, with a lepton collider, the beam energy is tunable and both
 784 electron and positron beams can be polarised. The selection of an appropriate
 785 polarisation can boost the signal and suppress the background cross-section.

786 Thirdly, as seen in the first point, at the LHC, only a fraction of the
 787 partons are contributing to the interesting process. The proton-proton in-
 788 teraction cross section is dominated by inelastic background QCD processes.
 789 The signal event is then accompanied by large backgrounds produced by the
 790 interaction of other parton collisions. This background masks the elementary
 791 process of interests, in order that it has an impact on the detector design,
 792 that should have a high radiation tolerance and implement a selective trigger
 793 to reduce the data rate. The lepton colliders do not suffer from this kind of
 794 background and at similar energies, the event rate is lower as those of hadron
 795 colliders. Moreover, the interaction of electrons and positrons is purely elec-
 796 troweak. In consequence, the detector does not have to handle extreme data
 797 rates and can be used without any trigger. Hence, the sensitivity to any
 798 possible signature of new physics is improved.

799 Although the leptons, in particularly the electron and positron, have
 800 clearer advantages on hadrons to perform a precise measurement, the choice
 801 of a linear collider comes from the physics of accelerating charged particles.
 802 While charged particles are moving in a circular accelerator, they lose some
 803 energy by emitting photons via synchrotron radiation. The equation 2.1
 804 describe the energy loss via synchrotron radiation:

$$\Delta E_{sync} \sim \frac{E^4}{m^4 r} \quad (2.1)$$

805 The radiative energy loss is proportional to the radius r of the accelerator,
 806 the energy of the particle E to the power of the fourth and its mass m to
 807 the power of the fourth. As the electron mass is $\sim 1.8 \times 10^3$ smaller than
 808 the proton mass, the energy loss radiated by the electron is bigger than
 809 the energy loss radiated by proton at the same centre-of-mass energy. To
 810 compensate the energy loss, a circular electron-positron accelerator should
 811 have an extremely big radius (bigger than the actual LHC), increasing the
 812 cost to build the experiment. Another solution to overcome the synchrotron
 813 radiation is to accelerate the particles in a linear collider. Nevertheless, the
 814 centre-of-mass energy has to be reached in only one path, whereas the bunch
 815 of particles in a circular collider is accelerated many times in the ring until the
 816 desired energy of collision is reached. To still get an "affordable" experiment,
 817 the centre-of-mass energy obtained at a linear collider is below to the one
 818 from a circular collider. Indeed, to work at the same energy scale, a linear
 819 collider would require a bigger number of accelerating cavities and would
 820 make a much bigger and more expensive collider than a circular one.

821 2.1.2 Future linear lepton collider

822 As it was mentioned before, the precise measurements offered by lepton col-
 823 linder is one of the key points to constrain the limits of the SM and to char-
 824 acterise precisely all the known particles. Since the 1980's, several linear
 825 collider technologies have been developed, leading in the 1990's to five ma-
 826 jor accelerator technologies: Superconducting Radio-Frequency (SRF), the
 827 Compact LInear Collider (CLIC) technology and three different normal con-
 828 ducting technologies (S-band, C-band, and X-band)[15]. At the beginning
 829 of the 2000's, a committee for the future linear collider was formed and has
 830 chosen in 2004 the SRF technology[26] and since then all the efforts are done

Paper on ILC

831 in that direction to build the International Linear Collider (ILC). The tech-
 832 nology developed for this future experiment is also used for the XFEL at
 833 DESY in Hamburg and at KEK in Japan. Another linear collider project
 834 led by the CERN is being prepared: the CLIC. It has a more challenging
 835 technology to aim a nominal energy of 3 TeV instead of 1 TeV for the ILC.
 836 Contrary to the ILC, CLIC plans to use radio-frequency structures and a two
 beam concept.

Paper on CLIC

837 Another idea would be to develop a muon collider instead of
 838 electron-positron collider[35]. As the electron, the muon is a pointlike par-
 839 ticle, therefore the centre-of-mass energy can be easily adjusted to perform
 840 a precise study. The muon mass is 207 times much bigger than the electron
 841 ones and suffers less of energy loss by synchrotron radiation. Hence, a cir-
 842 cular collider could be more adapted and the beamstrahlung effects would
 843 be smaller in a muon collider than in an e^+e^- machine. Nevertheless, the
 844 muon has a lifetime of only $2.2\ \mu s$ making up a more challenging acceleration
 845 design.

846 For the purpose of this thesis, the CLIC and muon colliders will not be
 847 described more to focus on details on the ILC.

848 2.2 The ILC machine

849 The ILC should be the next lepton collider experiment and will be situated
 850 in Japan. During 2016, the physicists community is waiting for an official
 851 decision of the Japan government concerning final site where the experiment
 852 will be held. At the time this thesis was written, the most likely site candidate
 853 is located in the north of Japan, in the region of Kitakami.

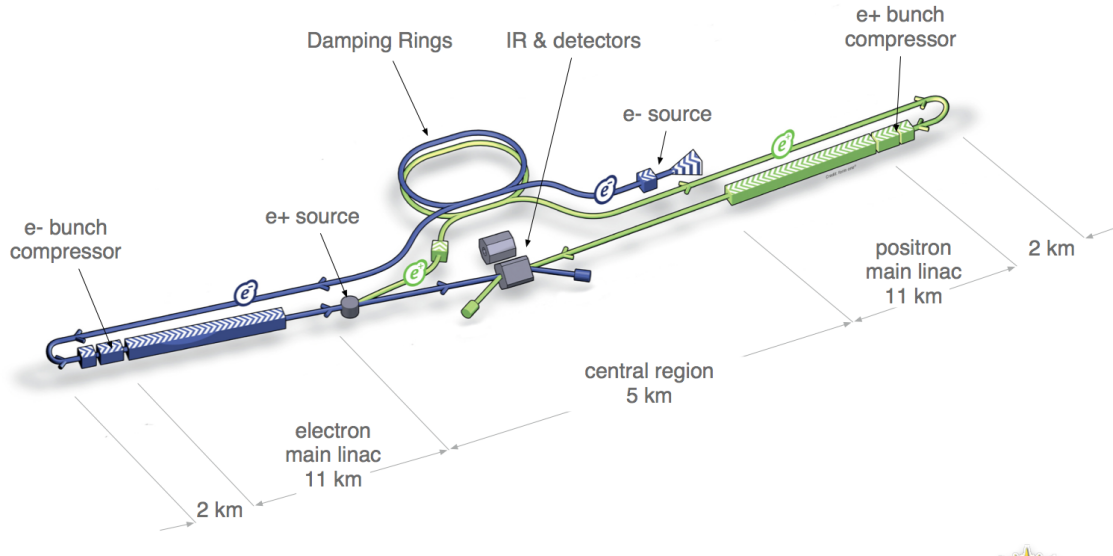


Figure 2.1 – Schematic layout of the International Linear Collider (ILC).[9]

2.2.1 Baseline design

The ILC is planned to collide electrons and positrons at a center-of-mass energy up to 500 GeV, with an energy variability down to 200 GeV for 31 kilometers long accelerator. An upgrade to reach the centre-of-mass energy of 1 TeV is also possible, but the accelerator should be extended to achieve a total length of 50 kilometers. It is designed to generate a total of 500 fb^{-1} of data during the first four years of operation. The luminosity will reach a peak of $2 \times 10^{34} \text{ cm}^{-2} \text{s}^{-1}$ at $\sqrt{s} = 500 \text{ GeV}$.

The main components of the ILC are presented in the following order: first of all, an overview of the electron source and their acceleration via the conducting and superconducting structures, then the role of the damping rings, the injection into the main linacs, followed by the positron source and the Beam Delivery System (BDS) to finally present the interaction region (IR). A detailed description of the ILC could be found in the Technical Design Report[4].

2.2.2 Machine design and beam parameters

The polarised electrons are produced by a laser firing a strained GaAs photocathode in a Direct-current (DC) gun. To implement a redundancy, the

872 electron generation system is made of two lasers and DC guns, providing
 873 bunches with a polarisation of 90 %. The electrons are then pre-accelerate to
 874 76 MeV thanks to non-superconducting accelerating structures. Thereafter,
 875 they are injected into a 250 m long superconducting linac to reach the en-
 876 ergy of 5 GeV. Nevertheless, the dimension and density of bunches are quite
 877 extended, thus their emittance is too wide. Before to inject the bunches
 878 into a damping ring, which is used in order to decrease the emittance and
 879 reach the desired luminosity, superconducting solenoids rotate the spin vec-
 880 tor into the vertical direction, while SRF cryomodules are used for an energy
 881 compression.

882 The damping ring is 6.7 km length and made of magnets and wrigglers
 883 that are going to force the particles to get a bent track. This system is used
 884 to dump the electrons with large transverse and longitudinal emittance to
 885 the low emittance required for the luminosity production. The reduction of
 886 the emittance should be achieved within 200 ms between the machine pulses.
 887 Although the positron source was not yet introduced, their bunches suffer
 888 from the same problems as the electron ones. A second damping ring, placed
 889 in the same cavern as the electron one, is also in charge to get the desired
 890 emittance.

891 The bunches are then extracted from the damping rings and transferred
 892 via the Ring To the Main Linac (RTML) structure, the longest continuous
 893 beam line at the ILC. It is divided into five subsystems to transport the
 894 bunches from the damping rings to the BDS, in order to orient the beam
 895 in the desired polarisation by rotating the spin of the particle, but also to
 896 compress the beam bunch length from several millimeters to a few hundred
 897 microns thanks to a two-stage bunch compressor. At the same time the
 898 bunches are compressed, sections of SRF technology accelerate the bunches
 899 from 5 GeV up to 15 GeV. One of the challenges of the RTML is to preserve
 900 the emittance obtained after the damping rings, while the length and the
 901 energy of the bunches are tunned. Then, the particles are delivered to the
 902 main Linac, an 11 km long accelerator using 1.3 GHz SRF cavities, made of
 903 niobium.

904 Before to reach the interaction region, the primary electron beam is trans-
 905 ported through a 147 m superconducting helical undulator to produce pho-
 906 tons from ~ 10 up to ~ 30 MeV, depending on the energy of the primary
 907 beam. This primary beam is separated from the photons and sent back to
 908 the BDS with an energy loss of ~ 3 GeV. The photons are directed onto a ro-
 909 tating Ti-alloy target to create e^+e^- pairs that are separated. The positrons
 910 collected are accelerated to 125 MeV thanks to a normal conducting linac
 911 and then accelerated to 5 GeV with a superconducting boost linac. Finally,
 912 they are introduced into the damping ring to reduce their emittance.

913 The two beams are transported from the high energy LINACS to the IR
 914 by the BDS, in charge to focus the beams to the sizes required to meet the
 915 ILC luminosity wanted. It is divided into five main subsystems. First, in
 916 the direction of the beam, a system is in charge to perform some emittance
 917 measurement and matching, to give a trajectory feedback, and provide a
 918 polarimetry and energy diagnostic. Then the beam is collimated to remove
 919 the beam-halo particles that would generate a huge amount of background in
 920 the detector. Muons generated during the collimation process are deflected
 921 by magnetised iron shielding. Thereafter, strong compact quadrupoles focus
 922 the beam to the sizes required to meet the desired luminosity. Before the
 923 collisions, crab cavities rotate the bunches in the horizontal plane for effective
 924 collisions and to achieve a 14 mrad total crossing angle. After the collisions,
 925 an extraction line is dedicated to transport the beams into the main beam
 926 dump.

927 Although two experiments will run at the ILC, there will be only one
 928 interaction region due to cost reasons. Indeed, to have two experiments
 929 running at the same time, it requires two separate BDS of 4 km long each.
 930 Thanks to a push-pull scheme, the detectors will work alternatively: while
 931 one is taking data, the other one is sitting in the garage to be maintained.
 932 The two detectors will be presented in more details at section [2.3](#).

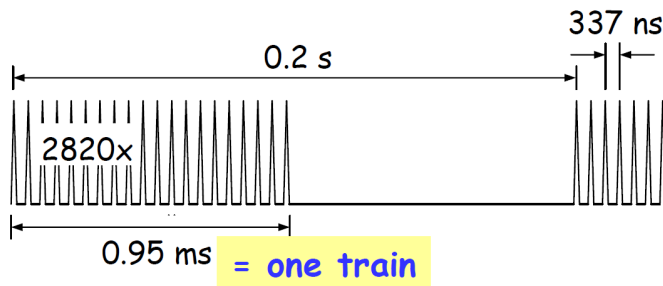


Figure 2.2 – Representation of the bunch structure at the ILC. One bunch train is made of 2625 bunch crossings and lasts 0.95 ms. Each bunch crossing is spaced out by 337 ns. Two bunch trains are of 0.2s apart from each other.[[34](#)]

933 The accelerator described above will create bunch trains at a repetition
 934 rate of 5 Hz. Each train is composed of 2625 bunches that contain 2×10^{10}
 935 particles and lasts 0.95 ms. The interval between two trains is 2 ms long.
 936 This structure is a feature key to develop detectors able to be switched off
 937 during the dead time in order to reduce the power consumption.

938 **2.2.3 Beam backgrounds**

939 To design the detectors of the ILC, the backgrounds must be understood and
 940 taken into account to give optimal performances. The event reconstruction
 941 becomes more complicated with hits caused by background particles. They
 942 are two kinds of background, the one created by the BDS and the one related
 943 to the interaction point. As it was discussed in the subsection 2.2.2, the
 944 collimator placed closed to the interaction point (IP) to purify the beam
 945 can produce muons by an electromagnetic shower. To sweep them away,
 946 iron spoilers are used to create a magnetic field and deflect the muons. A
 947 side effect is to increase the number of neutrons created in photo-nuclear
 948 reactions. A concrete wall placed at the entrance of the experimental hall
 949 vanishes the neutron background.

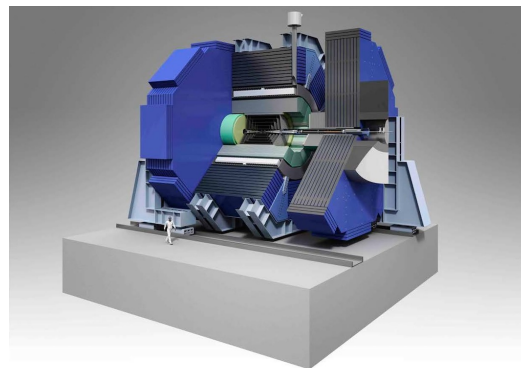
950 Contrary to the LHC, the ILC will not suffer from the QCD background,
 951 as mentioned in subsection 2.1.1 Nevertheless, due to the nature of electrons
 952 and positrons, the two beams will interact each other before they collide.
 953 The electromagnetic beam field of each bunch is high and causes the focus-
 954 ing of the opposite bunch. It is bending the electron/positron trajectories
 955 near the IP. On the one hand, this effect helps to focus the incoming beams
 956 and enhance the luminosity. On the other hand, as the charged particles have
 957 bending track, they are emitting hard photons via beamstrahlung, creating
 958 e^+e^- pairs background. The hard photon is strongly focused in the forward
 959 region and do not contribute strongly to the background in the detector.
 960 However, the e^+e^- pairs created contribute to the background directly or
 961 through backscattered particles. In consequence of the beamstrahlung, the
 962 beam particle energy is reduced, hence the collisions occur at different en-
 963 ergies from the nominal one and this affects the physics cross-section. The
 964 beamstrahlung photons can also produce neutrons by hitting components.
 965 The other source of hard photons is the initial state radiation. With the
 966 beamstrahlung, they contribute reducing the luminosity[37].

967 Different kinds of soft pairs background can be expected at the ILC:
 968 the coherent and incoherent pair production. The coherent pair production
 969 appears when beamstrahlung photons are interacting with the strong elec-
 970 tromagnetic field of the beams. In the ILC environment the coherent pair
 971 background are negligible, whereas the incoherent pair production is dom-
 972 inant. It corresponds to e^+e^- pairs created by the interaction of only two
 973 particles. They are to the number of three depending on the nature of the
 974 scattered photons creating the e^+e^- pair. The Bethe-Heitler process corre-
 975 sponds to the scattering of one real photon while the second one is virtual. It
 976 contributes to approximately two of the third pair production. The second
 977 process is the Landau-Lifshitz, where the two scattered photons are virtuals

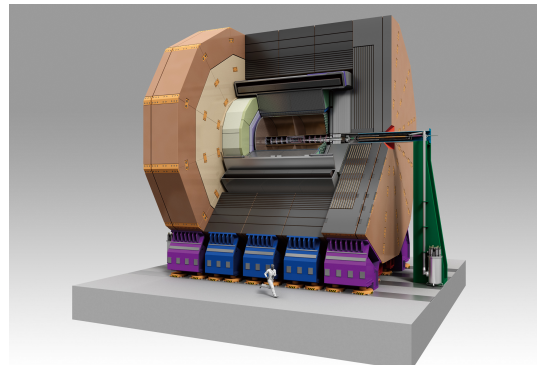
978 and contribute to approximately to the third of the pair creation. The last
 979 production occurred via two real photons (Breit-Wheeler process) and con-
 980 tribute only to a percent level. The incoherent e^+e^- pairs are produced at a
 981 relatively low transverse momentum and are emitted in the forward direction.

982 **2.3 The ILC detectors concept**

983 **2.3.1 Overview of the two experiments**



(a) The Silicon Detector



(b) The International Large Detector

Figure 2.3 – Overview of the two detectors designs at the ILC. The figure [a](#) represents the SiD design while the figure [b](#) shows the ILD approach.[\[10\]](#)

984 As it was presented in the subsection [2.2.2](#), the ILC will be built with
 985 only one interaction region due to cost reasons, whereas two detectors are

expected. The push-pull operation scheme will allow for data taking of one detector, while the second one is out of the beam in a close-by cavern for maintenance. The interval to switch the detectors should be short enough and of the order of one day. This time efficient implementation sets specific requirements for the beam structure but also for the detector design. The detectors should be placed on platforms to preserve the alignment and to distribute the load equally onto the floor. Another requirement on the detector design is that the magnetic fields outside the iron return yokes must be small enough to not disturb the second detector on the parking position. It is assumed that a limit of 5 mT at a lateral distance from the beam line should be sufficient.

The motivation to build two detectors with a different approach is mainly to provide a cross-checking and a confirmation of results and complementary strengths. Both detectors are optimised to study a broad range of precision measurements and search of new physics drove by the ILC expectations. Their performances are driven by the Particle Flow Algorithm (PFA) to be able to measure the final states of events with a high accuracy. To do so, both detectors should have a high hermeticity, high granularity calorimeters and excellent tracking and vertexing. The PFA is shortly presented on subsection 2.3.2.

The Silicon Detector (SiD) is a compact detector made of a silicon tracking and 5 T magnetic field. The tracking system should provide robust performance thanks to the time-stamping on single bunch crossings. The calorimeters should be highly granular to perform the PFA.

The second detector is the ILD. In contrast to the SiD, the tracking system is based on a continuous readout Time-Projection-Chamber (TPC) surrounded by silicon tracking detectors. The magnetic field will be only of 3.5 T combined with granular calorimeters for a good particle-flow reconstruction

2.3.2 Particle flow algorithm

The main purpose of the ILC (or the CLIC) is to achieve precise measurements of physics processes that produce final states with multiple jets. The jet energy resolution at the ILC should be sufficient to cleanly separate W and Z hadronic decays. Typically, the jet energy resolution is deduced from the equation 2.2, where α is the stochastic term usually greater than $\sim 60\%/\sqrt{E(\text{GeV})}$.

$$\frac{\sigma_E}{E} \simeq \frac{\alpha}{\sqrt{E(GeV)}} \oplus \beta \quad (2.2)$$

1022 The PFA approach is the extended version of the Energy Flow approach
 1023 (used at H1, D0, CMS) for a highly granular detector. The goal of this
 1024 framework is to achieve a stochastic term for the energy resolution greater
 1025 than $30\%/\sqrt{E(GeV)}$, not reachable with a traditional calorimeter. Each sub-
 1026 detector should be efficient enough to separate and to reconstruct the four-
 1027 vectors of all visible particles in an event. The energy of charged particle
 1028 is measured in the tracking detectors, while the energy measurements for
 1029 photons are done in the electromagnetic calorimeter and neutral hadrons are
 1030 done in the hadron calorimeter.

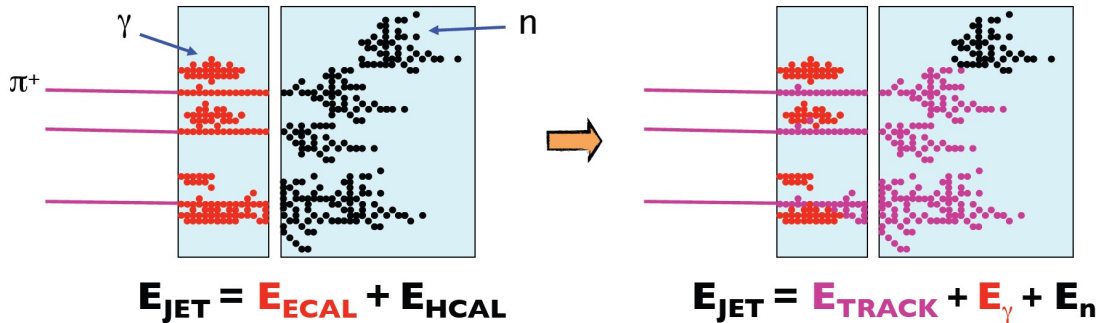


Figure 2.4 – Two different approaches for calorimetry. On the left is the traditional calorimetry method used on most of the experiments, the right one is the particle flow approach for calorimetry. The particle track is taken into account to calculate the jet energy.[24]

1031 The PFA requirements drive the design of the detectors at the ILC. For
 1032 both experiments, the electromagnetic and hadronic calorimeter have to be
 1033 located inside the solenoid. Moreover, each sub-detector must be able to
 1034 distinguish single particle signals, imposing a better tracking precision and
 1035 higher granular calorimeters than the traditional detectors in high energy
 1036 physics.

1037 2.3.3 The ILD detector

1038 The design of ILD follows the requirements for optimal PFA performance.
 1039 In summary, the detector should be highly granular to have a robust three-
 1040 dimensional imaging capability. It will combine a high-precision Vertex De-

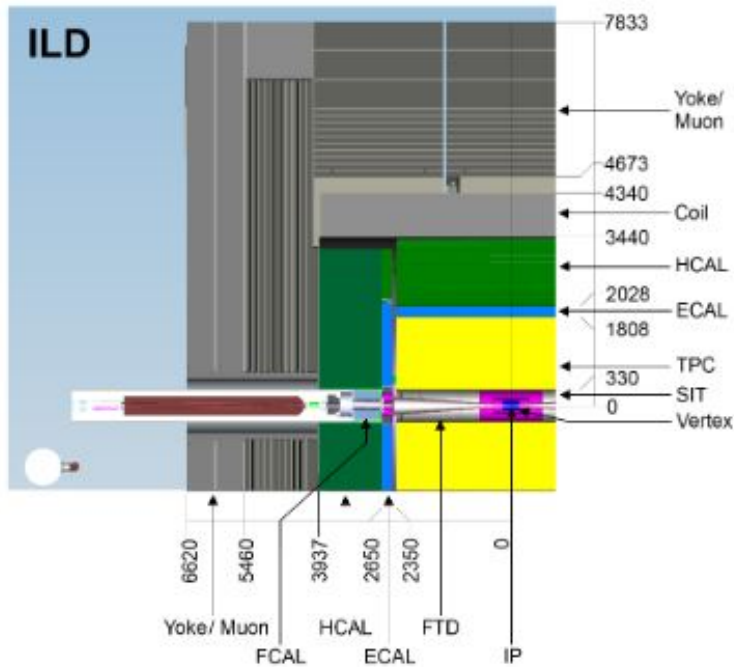


Figure 2.5 – Quadrant view of the ILD detector concept with its subdetector system [10]

1041 tector (VXD) system, a hybrid tracking system and calorimeters inside a 3.5
 1042 T solenoid. On the outside, a coil and iron return yoke will be instrumented
 1043 as a muon system and a tail catcher.

1044 Vertex detector

1045 The VXD is the closest detector to the interaction region and it is in charge
 1046 to the measured to track particles and to measure the decay vertices of the
 1047 particles. For the moment, two vertex detector design are under study, but
 1048 both of them have a pure geometry barrel. One geometry is made of five
 1049 single sided layers, whereas the other one has three double-sided detection
 1050 layers. The chapter ?? will introduce in more details the vertex detector
 1051 requirements for the ILD, such as the material budget and the measurements
 1052 precision aimed. The different design proposals will be presented.

1053 **Tracking**

1054 The main tracking system for the ILD is performed by the TPC. It is a
 1055 gaseous detector with a low material budget designed to measure the parti-
 1056 cles' trajectory. When a particle traverses through the TPC, it ionises the
 1057 gas, creating electrons that are drifting to the anode thanks to a high voltage.
 1058 The anode is the part where the readout plates are installed. It provides a
 1059 3D position of the particles tracks thanks to the wires and the anode (give
 1060 x-y) and the z coordinate is given by the drifting time. In addition to the
 1061 exact position measurement, this detector is also able to measure the en-
 1062 ergy $\frac{dE}{dx}$ deposited by the particle and would be the first step for a particle
 1063 identification.

1064 The requirements to design a TPC at the ILC are given by two main
 1065 values:

- 1066 • The single point resolution $\sigma_{s.p.}$ which should be lower than $100 \mu\text{m}$ in
 1067 the $r\phi$ direction and less than $500 \mu\text{m}$ in the z direction;
- 1068 • The minimum distance to separate two hits which should be lower than
 1069 2 mm.

1070 The TPC thought for the ILD is constituted of a central barrel part,
 1071 with an inner radius of $\simeq 33 \text{ cm}$ and a outer radius of $\simeq 180 \text{ cm}$ and two
 1072 endcaps with a detection area of 10 m^2 . The solid angle coverage is up to
 1073 $|\cos \theta \simeq 0.98|$. The barrel will be filled with a gas mixture called T2K (3 %
 1074 of Ar-CF₄ and 2 % of isobutane). Due to the low material budget and the
 1075 ability to cope with a high magnetic field, the TPC is compliant with the
 1076 PFA [2.3.2](#).

1077 To improve the track reconstruction, the TPC is surrounded by high sil-
 1078 icon detectors: two barrel components, the Silicon Internal Tracker (SIT)
 1079 and the Silicon External Tracking (SET); an end-cap component, the End-
 1080 cap Tracking Detector (ETD) and the Forward Tracking Detector (FTD).
 1081 The SIT is linking the tracking between the VXD and the TPC, whereas the
 1082 SET is giving an entry point to the Electromagnetic CALorimeter (ECAL)
 1083 after the TPC. Both systems provide precise space points and improve the
 1084 overall momentum resolution. The goal of the SIT is to improve the mo-
 1085 mentum resolution, the reconstruction of low p_T charged particles and the
 1086 reconstruction of long-lived particles. The coupling of the SIT and SET
 1087 provide also a time-stamping information.

1088 The ETD is located within the gap separating the TPC and the endcap
 1089 calorimeter. It improves the momentum resolution for charged tracks with

1090 a reduced path in the TPC. It also reduces the effect of the material of the
 1091 TPC end-plate. The material budget of this end-plate is estimated to 15 %
 1092 of X_0 .

1093 As the TPC does not provide any coverage in the forward region, seven
 1094 silicon disks ensure efficient and precise tracking down to very small angles,
 1095 whereas the ETD and the FTD make sure to get a full tracking hermeticity.

1096 To simplify the system layout and the maintenance, the SIT, SET and
 1097 ETD are made of single-sided strip layers tilted by a small angle with respect
 1098 to each other. They are placed in a so-called false double-sided layers. The
 1099 SIT has two layers of microstrip, instead of one layer for the SET. The
 1100 technology studied are microstrip sensors with an area of $10 \times 10 \text{ cm}^2$, with a
 1101 pitch of $50 \mu\text{m}$, a thickness of $200 \mu\text{m}$ and an edgeless. The dead area of the
 1102 sensors will be reduced down to few microns instead of $100 \mu\text{m}$. The spatial
 1103 point resolution aimed for this detectors is $\sim 7.0 \mu\text{m}$ in the $r\phi$ direction.
 1104 The table 2.1 gives the single point resolution aimed, as well as the angular
 1105 coverage and the material budget.

Detector	Single point resolution (μm)	Coverage	material budget X_0 (%)
SIT	$\sigma_{R-\phi} = 7.0$ $\sigma_Z = 50.0$	$\cos \theta \sim 0.91$	0.65
SET	$\sigma_R = 7.0$	$\cos \theta \sim 0.79$	0.65
ETD	$\sigma_X = 7.0$	$\cos \theta \sim 0.799 - 0.985$	0.65

Table 2.1 – Parameters aimed for the silicon tracker using micro-strips sensors.

1106 The FTD is placed in the forward direction, between the beam pipe and
 1107 the inner field cage of the TPC, where the magnetic field becomes less and
 1108 less useful to bend charged tracks and so the determination of a precise
 1109 momentum is more difficult. It consists of seven tracking disks: the two
 1110 firsts are pixel detectors to cope with expected high occupancies and the
 1111 five others are strip detectors. The pointing resolution will vary between
 1112 $3.0 - 6.0 \mu\text{m}$ for the two firsts layers and $7.0 \mu\text{m}$ for the five other ones.

Check the table
and values....

1114 Calorimeters

1115 The calorimeters design is driven by the particle flow requirements. Each
 1116 particle must be reconstructed individually in the detector with a jet energy

1117 measurement equal to:

$$\frac{\Delta E}{E} = 30\% / \sqrt{\frac{E}{GeV}} \quad (2.3)$$

1118 The energy resolution obtained in equation 2.3 is obtained thanks to a
 1119 combination of information from the tracking system and the calorimeters.
 1120 The choice of technology used for the calorimeter will be determined by
 1121 the pattern recognition performance. One of the ILD detector's goal is, for
 1122 example, to be able to get a jet energy resolution sufficient to clean separate
 1123 W and Z hadronic decays.

1124 The average jet energy distribution is roughly:

- 1125 • 62% of charged particles (mainly hadrons)
- 1126 • 27% of γ
- 1127 • 10% of long-lived neutral hadrons
- 1128 • 1.5% of ν

1129 The ECAL is the first calorimeter right after the tracking system. Its role
 1130 is to identify photons and leptons and measure their energy, nevertheless, it
 1131 is also the first section to develop the hadron showers. The fine segmentation
 1132 makes an important contribution to hadron-hadron jet separation. For the
 1133 ILD, a compromise between the performance and the cost has led to use a
 1134 sampling calorimeter realised with tungsten absorber. They are three options
 1135 under study for the active area. The first one called SiW-ECAL, is made of
 1136 silicon pin diodes with a pitch of $5 \times 5\text{mm}^2$. It has the advantage to cover a
 1137 large area, to be reliable and simple to operate, to have thin readout layers
 1138 and can be operated in 3.5 T magnetic field. The second option is made
 1139 of scintillator strips readout by photo-sensors and is called ScECAL. It has
 1140 an active area of $5 \times 45\text{mm}^2$ arranged in alternative directions to achieve an
 1141 effective granularity of $5 \times 5\text{mm}^2$. The weakness of this technology happened
 1142 in dense jets environment, where the reconstruction becomes more and more
 1143 complicated. Some alternatives are also thought, like the Micromegas cham-
 1144 bers. Nevertheless, this technology is less advanced compared to the others.
 1145 One other good candidate could be the use of Monolithic Active Pixel Sensor
 1146 (MAPS) sensors. They have the advantage to get the signal sensing and pro-
 1147 cessing on the same substrate and by choosing standard CMOS processes,
 1148 the cost of fabrication would be reduced.

1149 The HAdronic CALanalogue HCALorimeter (HCAL) has the role to sep-
 1150 arate the deposits energy of charged and neutral hadrons and to precisely

measure the energy deposited. It is also a sampling calorimeter using stainless steel instead of tungsten as an absorber. The rigidity of stainless steel makes possible to get a self-supporting structure limiting the dead areas. Two baseline technologies for the active medium area are studied. The Analogue HCAL (AHCAL) is made of scintillator tiles, whereas the semi-digital, called Glass Resistive Plate Chamber (GRPC), is based on the Semi-Digital HCAL (SDHCAL).

In order to monitor the luminosity and the beamstrahlung, the calorimeter system is completed in the very forward region by three different subsystems covering very small angles also for neutral hadrons: the LumiCal, the BeamCAL, and the Low angle Hadron CALorimeter (LHCAL). The LumiCAL is placed in a circular hole of the end-cap ECAL and covers polar angles between 31 and 77 mrad. It serves as luminosity monitor by measuring the Bhabha scattering $e^+e^- \rightarrow e^+e^-$ via emission of virtual γ . Indeed, the luminosity \mathcal{L} is determined by measuring the ratio of the number of counted events N_B in a considered polar angle ranged and the integral of the differential cross-section σ_B in the same region. The measurement precision should be better than 10^{-3} at 500 GeV. After each bunch crossing, the beamstrahlung pairs hit the BeamCal. This would permit to get an estimation of the bunch-by-bunch luminosity, but also to determine the beam parameters. It is placed in front of the final focus quadrupole and covers polar angles between 5 and 40 mrad. The third system, the LHCAL, ensure the coverage of the hadron calorimeter to small polar angles.

Magnetic Field and yoke

By applying a high magnetic field inside the detector, the charged particles have a bent track helping in the identification and the energy measurement. At the ILD, the nominal magnetic field is 3.5 T and should have a high homogeneity inside the TPC. Moreover, as mentioned in subsection 2.2.2, the magnetic beyond the coil has to be reduced to avoid any perturbations with the second detector in its parking position. A superconducting coil surrounding the tracking and calorimetric system generate the magnetic field. It has a diameter of 6.88 m, a length of 7.35 m and made of three modules.

Surrounding the coil, an iron yoke ensures to return the magnetic flux. It is constituted by a barrel of 2.88 m thickness and 2 end-caps of 2.12 m thickness. Muon detectors are inserted inside the iron yoke in a sandwich-like structure. They're performing measurement on muons but they are also used as tail catchers, to improve the energy resolution of high energetic jets escaping the calorimeters.

2.4 Conclusions

In this chapter, the reasons to build a linear electron/positron collider were discussed by introducing the pros and cons of such a big experiment. In order to reduce the costs, only one interaction region is planned but two detectors are going to operate alternately. The design of the detectors is driven by the particle flow approach to reach a ... energy resolution. In particularly, the onion structure of ILD was peeled. The different sub-detectors and the technology options were introduced, except for the vertex detector. Indeed, the chapter 4 will be dedicated to the vertex detector at the ILD.

The next chapter will introduce the physics cases at the ILC, especially by describing an approach to a physics analysis to study the $H \rightarrow c\bar{c}$.

1200 Chapter 3

1201 Physics at the ILC

1202 In the chapter 1, the framework of particles physics was described. Since
1203 the beginning of High Energy Physics, different experiments have been done
1204 to confirm the exactness of the SM but also to find new physics beyond the
1205 SM. The beam structure of the different colliders allow to perform different
1206 measurements with different precision. For example, the LHC has a high
1207 luminosity and high energy beam, able to reach new energy scales on earth,
1208 whereas the ILC is trying to reach more precise results, with less energy.
1209 Along this chapter, the physics scenarios that are going to be studied at the
1210 ILC are discussed. Afterward, the emphasis will be on the Higgs physics and
1211 the measurement that would be performed at the ILC. The last section aims
1212 to introduce a physics analysis scenario to study the processes which have a
1213 Higgs boson and two neutrinos in the final state.

1214 Contents

<small>1215</small> 3.1 Potential studies	<small>40</small>
<small>1216</small> 3.2 Higgs physics	<small>41</small>
<small>1217</small> 3.2.1 Production of the Higgs at the ILC	<small>42</small>
<small>1218</small> 3.2.2 Decays of the Higgs	<small>44</small>
<small>1219</small> 3.2.3 Higgs studies	<small>44</small>
<small>1220</small> 3.3 Analysis of simulated data	<small>45</small>
<small>1221</small> 3.4 Simulation set-up	<small>45</small>
<small>1222</small> 3.4.1 Signal	<small>46</small>
<small>1223</small> 3.4.2 Background processes	<small>47</small>
<small>1224</small> 3.4.3 Event reconstruction	<small>47</small>
<small>1225</small>	

1226	3.4.4 Event selection	47
1227		

1230 3.1 Potential studies

1231 As seen in chapter 2, the ILC will have a vast and variable tunable centre-
 1232 of-mass energy. Due to the features of an e^+e^- collider, the initial state of
 1233 collision is well defined. Contrary to the LHC, there are no strong interac-
 1234 tion backgrounds and the electroweak background is controlled and calcula-
 1235 ble. This conditions will help to perform precise measurements and looking
 1236 for new physics. The different measurements which will be performed are
 1237 presented below.

1238 First of all, a study of the Z boson at the centre-of-mass energy of
 1239 $\sqrt{s} = 91$ GeV around the Z resonance is scheduled. This program called
 1240 *GigaZ* will be able to collect more Z boson events than the Large Electron
 1241 Positron collider (LEP) did, because of a luminosity two to three times higher
 1242 than what was achieved. The data collected will allow a study on the asym-
 1243 metries of the Z boson couplings. A second program, called *MegaZ*, will be
 1244 performed at the centre-of-mass energy of $\sqrt{s} = 160$ GeV reaching the WW
 1245 production threshold and trying to measure the W boson mass with a pre-
 1246 cision of MeV/c^2 . At higher energy, it will also be possible to measure more
 1247 precisely the W boson couplings.

1248 Afterward, the centre-of-mass energy will be adjusted to $\sqrt{s} = 250$ GeV
 1249 to perform a study on the Higgs boson couplings, as well to measure its
 1250 the quantum numbers. At this energy, the Higgs boson is mainly produced
 1251 via Higgs-strahlung. The measurement is done thanks to the recoil mass
 1252 independently of the Higgs decay products.

1253 Then, for a centre-of-mass energy between 350 and 400 GeV, two studies
 1254 are achievable. The WW-fusion process starts to rise and permits to measure
 1255 the couplings of the Higgs boson to the W ones in order to look for deviation
 1256 from the Standard Model. Moreover, this channel allows to study some rare
 1257 decays. This energy range corresponds also to the threshold of the top quark
 1258 pairs production. Because of the top quark life-time, the two quarks created
 1259 are not in a bounded-state. By performing a threshold scan, the mass of the
 1260 top quark can be measured with a precision reaching $100 \text{ MeV}/c^2$.

1261 The nominal energy of the ILC is achieved at $\sqrt{s} = 500$ GeV. This energy
 1262 scale is suitable to look for supersymmetry candidates and possible extended
 1263 states of the Higgs boson.

An upgrade of the ILC to reach the centre-of-mass energy $\sqrt{s} = 1$ TeV is also scheduled. Up to 1 TeV, new measurements are possible, such as the coupling of the Higgs boson to the top quark, the Higgs boson self-coupling, or its compositeness. Although, search for new exotic particles and physics beyond the SM is possible.

The table 3.1 summarises the different physics programs at the ILC for the different energy reachable.

Energy (GeV)	Reaction	Physics Goal
91	$e^+e^- \rightarrow Z$	ultra-precision electroweak
160	$e^+e^- \rightarrow WW$	ultra-precision W mass
250	$e^+e^- \rightarrow Zh$	precision Higgs coupling
	$e^+e^- \rightarrow t\bar{t}$	top quark mass and couplings
350 - 400	$e^+e^- \rightarrow WW$	precision W couplings
	$e^+e^- \rightarrow \nu\bar{\nu}h$	precision Higgs couplings
	$e^+e^- \rightarrow f\bar{f}$	precision search for Z'
	$e^+e^- \rightarrow t\bar{t}h$	Higgs coupling to top
500	$e^+e^- \rightarrow Zh h$	Higgs self-coupling
	$e^+e^- \rightarrow \tilde{\chi}\tilde{\chi}$	search for supersymmetry
	$e^+e^- \rightarrow AH, H^+H^-$	search for extended Higgs states
	$e^+e^- \rightarrow \nu\bar{\nu}hh$	Higgs self-coupling
700-1000	$e^+e^- \rightarrow \nu\bar{\nu}VV$	composite Higgs sector
	$e^+e^- \rightarrow \nu\bar{\nu}t\bar{t}$	composite Higgs and top
	$e^+e^- \rightarrow t\bar{t}^*$	search for supersymmetry

Table 3.1 – Summary of the major processes that will be studied at the ILC for different energies[6].

3.2 Higgs physics

The Higgs boson found at the LHC has to be characterised more precisely. One of the goal study at the ILC is to determine if the particle found is compatible with the one defined by the Standard Model, or if other states exist. The measurement of the Higgs boson couplings to the Standard Model particle is one of the key to verify the exactness of the mass generation mechanism described by this theory and to open the door to any proof of physics beyond the Standard Model. The production, the decay modes of

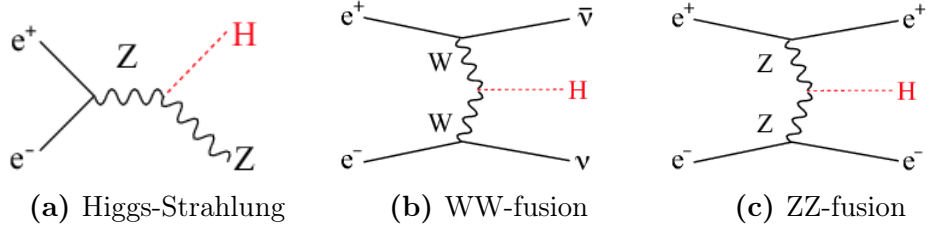


Figure 3.1 – Feynman diagrams of the main Higgs production at the ILC[5][45].

1279 the Higgs boson, as well as the measurement feasible are presented below in
 1280 the case of the ILC.

1281 3.2.1 Production of the Higgs at the ILC

1282 Due to the beam structure at the ILC, the Higgs boson is accessible by di-
 1283 rect measurement. The production of the Higgs boson defined by the Stan-
 1284 dard Model is done via three major processes: the Higgs-strahlung (see fig-
 1285 ure 3.1a), the WW-fusion (see figure 3.1b) and the ZZ-fusion (see figure 3.1c).

1286 **Higgs-strahlung:** $e^+e^- \rightarrow ZH \rightarrow f\bar{f}X$

1287 **WW-fusion:** $e^+e^- \rightarrow \nu\bar{\nu}W^+W^- \rightarrow \nu\bar{\nu}H$

1288 **ZZ-fusion:** $e^+e^- \rightarrow e^+e^-ZZ \rightarrow e^+e^-H$

1289 The figure 3.1 summarises the different Feynman diagrams of the Higgs
 1290 boson production.

1291 At the centre-of-mass energy $\sqrt{s} = 250$ GeV, the Higgs-strahlung is the
 1292 dominant process and occurs via a s-channel. Its cross-section falls off as $1/s$
 1293 as the centre-of-mass energy \sqrt{s} increases. Contrary to the Higgs-strahlung,
 1294 the WW-fusion and the ZZ-fusion are t-channel processes which have a cross-
 1295 section growing logarithmically with the centre-of-mass energy. Thus, at
 1296 250 GeV, the cross-section of the WW-fusion is one order smaller than
 1297 the Higgs-strahlung and the ZZ-fusion is negligible. Nevertheless, around
 1298 500 GeV, the WW-fusion and the Higgs-strahlung have the same cross-
 1299 section, which is around 120 fb. The figure 3.2 shows the cross-section pro-
 1300 duction of the Higgs at the ILC regarding the energy of the collision.

1301 The WW-fusion occurs only with left-handed electrons associated to right-
 1302 handed positrons. Thus, by modifying the beam's polarisation, the signal
 1303 mixture can be changed, as well as the background processes.

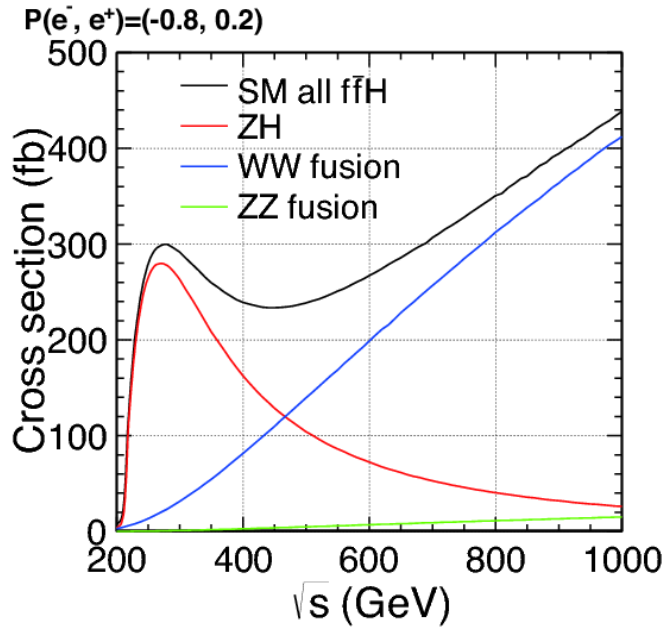


Figure 3.2 – The cross section production of the Higgs boson with a mass of 125 GeV[5].

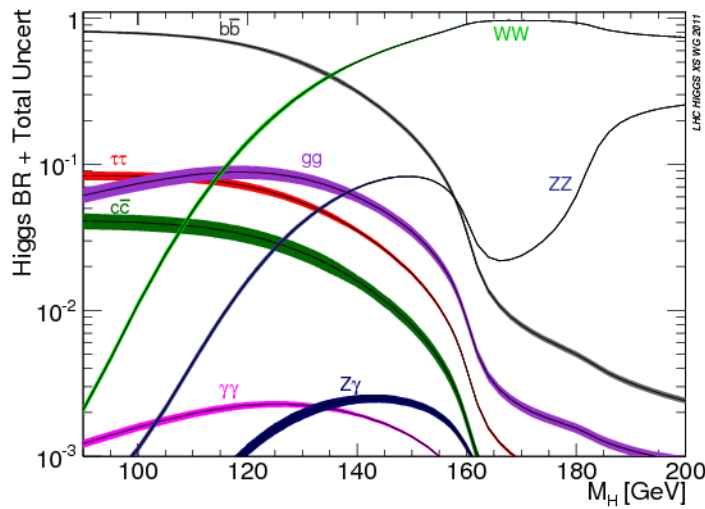


Figure 3.3 – The Higgs branching ratio with the branching ratio uncertainties for the Higgs mass varying from 80 to 200 GeV[14].

3.2.2 Decays of the Higgs

1304 Although the decay $H \rightarrow b\bar{b}$ is the dominant decay mode of the Higgs at
 1305 hadrons colliders, the boson was observed by studying its decay to two photons.
 1306 The other decay states are challenging to separate from the background.
 1307 Thanks to the properties of the ILC beams, the couplings of the Higgs to the
 1308 particles of the SM is measurable. Thus, the following decay are available:
 1309 $b\bar{b}$, WW , ZZ , gg , $c\bar{c}$, $\tau\tau$, $\gamma\gamma$, γZ . The observation of the $H \rightarrow c\bar{c}$ is one of the
 1310 constraint parameter to build the detectors, specifically, the vertex detector
 1311 that should be able to distinguish the vertices coming from the b -quarks to
 1312 the ones coming from the c -quarks. The figure 3.4 depicts the mass-coupling
 1313 relation of the Higgs boson to the particles of the SM. The SM nature of the
 1314 Higgs boson will be tested by looking for any deviations from its fermionic
 1315 coupling. A deviation might indicate multiple states for the Higgs boson.

1304 H decays at LHC: bb, WW, tau tau, gamma gamma, gg and ZZ
 1305 1306 1307 1308 1309 1310 1311
 1312 Not clear enough

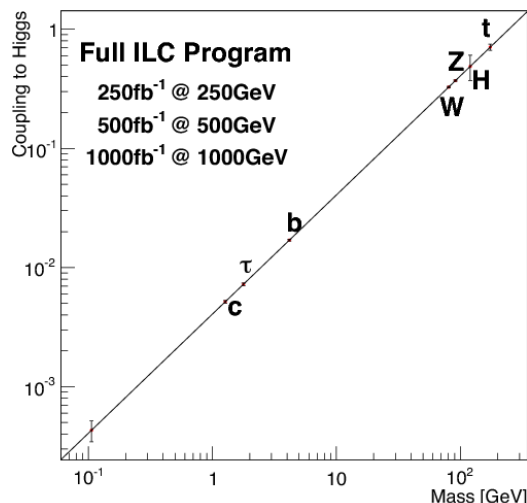


Figure 3.4 – Mass-coupling relation of the Higgs boson to the particles defined in the standard model[45].

3.2.3 Higgs studies

1317 The first study will be at the peak production of the Higgs-strahlung. The
 1318 well defined four-momentum initial state allows to measure the Higgs boson
 1319 mass regardless its decay products. The Higgs invariant mass M_H can be
 1320 calculated by using the recoil technique:

$$M_H^2 = s + M_Z^2 - 2\sqrt{s}(E_1 + E_2), \quad (3.1)$$

Where M_Z is the mass of the Z boson, E_1 and E_2 are the energy of the Z decay products. This technique works well for the Z boson decaying into leptons at the centre-of-mass energy $\sqrt{s} = 250$ GeV. However, at this centre-of-mass energy, this method can not be performed for a Higgs decaying into quarks. The Z boson and the Higgs boson are produced almost at rest, thus, the identification of the jets coming from the Z boson to the ones coming from the Higgs boson is more difficult. Nevertheless, at higher energy ($\sqrt{s} = 500$ GeV), the two bosons are enough boosted to separate their jets and then to apply again the recoil mass. Depending on the decay channel of the Z bosons, the statistical precision on the mass measurement varies between 40 MeV (for $Z \rightarrow \mu^+ \mu^-$) to 80 MeV (for $Z \rightarrow e^+ e^-$) and can reach 32 MeV by combining the two results.

The spin and CP measurement are also going to be performed. The LHC has excluded the possibility of spin 1 boson, thanks to the measurement of the di-photon channel. At a centre-of-mass energy $\sqrt{s} = 250$ GeV, the cross-section of the higgs-strahlung depends on the spin and CP numbers. For example, if the spin is 0 and the CP even, the cross-section is If spin 0 and CP-odd: cross section

3.3 Analysis of simulated data

Due to the restricted time to conduct the thesis, this section is introducing the tools to perform an analysis of some simulated data at the ILD. The results shown are not the latest and were already demonstrated. Nevertheless, the philosophy to perform a study of the Higgs production at the center-of-mass energy $\sqrt{s} = 350$ GeV and a luminosity of 250 fb^{-1} is here presented.

3.4 Simulation set-up

Monte Carlo simulation and analysis software framework were developed for the linear collider community.

ILCSoft

The ILCSoft provides a large variety of software packages which were developed for the linear collider community[27]. It includes software for Monte-

1352 Carlo simulation, as software for test beam analysis (see section ??) and other
 1353 tools. The main package is the Linear Collider I/O (LCIO), a persistency
 1354 framework and event data model for the linear collider detector studies[32].
 1355 It provides a common data format and event data model for both the sim-
 1356 ulation studies and the analysis framework in order to share results and
 1357 compare reconstruction algorithms. A C++ software framework called Mod-
 1358 ular Analysis and Reconstruction for the LINear collider (Marlin) is used for
 1359 the reconstruction and the analysis by using the LCIO data format. Each
 1360 tasks are structured into module called processors. A steering file written in
 1361 XML is used to select the processors to use and the order of their execution
 1362 time. An other package is GEometry Api for Reconstruction (GEAR). It is
 1363 use as a geometry detector toolkit. A steering file is in charge to perform the
 1364 interface of the detector geometry during the data reconstruction and the
 1365 analysis.

1366 The Monte-Carlo simulation is performed in three steps. The first one
 1367 consists to generate the physics events of electron/positron collisions. The
 1368 generation of Mont-Carlo events are performed with WHIZARD. This soft-
 1369 ware includes Standard Model processes, as well as a large variety of BSM
 1370 models. For the purpose of the ILC, it can simulate the beamstrahlung,
 1371 the Initial State Radiation (ISR) and the beam polarisation. Although the
 1372 hard interaction are simulated thanks to WHIZARD, the hadronisation and
 1373 fragmentation are implemented via PYTHIA.

1374 Afterward the physics events are generated, the particle interaction inside
 1375 the detector is simulated with MOKKA. The software is based on GEANT4
 1376 simulation toolkit and is par of the ILCSoft. For the analysis, the detector
 1377 model used is ILD_o1_v05. This model simulates the dead areas due to
 1378 cabling, cooling system and mechanical structure and has a silicon-tungsten
 1379 electromagnetic calorimeter, as well as an analog hadronic calorimeter.

1380 Finally, the events are reconstructed thanks to Marlin.

1381 3.4.1 Signal

1382 The two dominant production processes leading to the $\nu\nu H$ final state are the
 1383 Higgs-strahlung and the WW-fusion. The leading order Feynman diagrams
 1384 are displayed on figures 3.1a and 3.1b. Although only ν_e are produced in the
 1385 WW-fusion process, the neutrinos does no interact inside the detector and
 1386 the flavor of the neutrinos cannot be studied.

3.4.2 Background processes

The hypothesis is to have a final state consisting of two jets coming from the decay of the Higgs boson plus missing energy from two neutrinos. Are considered as background, the events with the same final states as the signal and the events with a similar detector response.

W-boson pair production • Semi-leptonic decay
• Hadronic decay

Z-boson pair production • Hadronic decay
• Leptonic decay
• Hadronic decay with missing energy

Single W-boson production

Single Z-boson production • Hadronic decay
• Hadronic and electron/positron decay

Higgs-strahlung • Hadronic decay
• Leptonic decay

3.4.3 Event reconstruction

- Identification of isolated leptons to remove some of the background processes
- Look for jet-like objects in the forward region corresponding to low pT hadrons coming from $\gamma\gamma$ interactions.
- Jet clustering and flavor tagging

3.4.4 Event selection

Process	Cross Section (fb)	Events number	Isolated leptons = 0	$35 < P_t^{\text{vis}} < 155 \text{ GeV}$	$95 < m_{\text{vis}} < 140 \text{ GeV}$	$-1 < \cos \alpha < 0.22$
Zhad	3.86×10^4	1.27×10^7	1.26×10^7	1.09×10^5	5.79×10^2	5.05×10^2
WW had	6.53×10^3	2.16×10^6	2.14×10^6	5.27×10^3	6.29	6.29
WW semilep	8.16×10^3	2.69×10^6	1.17×10^6	6.38×10^5	1.13×10^5	6.26×10^4
ZZ had	6.01×10^2	1.98×10^5	1.97×10^5	2.74×10^3	1.20	6.20×10^{-1}
ZZ semilep	5.65×10^2	1.86×10^5	1.40×10^5	7.49×10^4	1.46×10^4	8.20×10^3
singleW semilep	1.63×10^3	5.36×10^5	2.24×10^4	8.79×10^3	1.65×10^3	1.63×10^3
singleZee semi	3.10×10^2	1.02×10^5	1.30×10^4	2.17×10^1	7.00×10^{-2}	7.00×10^{-2}
singleZnn semi	3.55×10^2	1.17×10^5	1.17×10^5	8.38×10^4	1.62×10^4	1.19×10^4
Higgs BG	1.62×10^2	5.34×10^4	4.19×10^4	4.59×10^3	1.93×10^2	1.43×10^2
HiggsToOther	3.05×10^1	1.01×10^4	6.66×10^3	4.95×10^3	3.45×10^3	2.64×10^3
Background	5.69×10^4	1.88×10^7	1.65×10^7	9.31×10^5	1.50×10^5	8.76×10^4
Signal	6.82×10^2	2.25×10^4	2.23×10^4	1.82×10^4	1.66×10^4	1.57×10^4
Significance		5.19	5.48	1.87×10^1	4.06×10^1	4.88×10^1

Table 3.2 – Cut flow chart with different cuts applied.

¹⁴⁰⁹

Chapter 4

¹⁴¹⁰

Double-sided VXD: PLUME

¹⁴¹¹ Since the end of the 1960's, the development of position sensitive silicon
¹⁴¹² sensors has permitted to confirm the prediction of the Standard Model (SM)
¹⁴¹³ with a high precision, as well as the discovery of the top quark. These
¹⁴¹⁴ sensors, called Vertex Detector (VXD), are in charge to track the particles
¹⁴¹⁵ down to their decay vertices. The design of such device is driven by the
¹⁴¹⁶ physics requirement of the experiment and is playing a crucial role at the
¹⁴¹⁷ International Linear Collider (ILC). For example, one flagship measurement
¹⁴¹⁸ is the study of the Higgs boson couplings to the fermions and other bosons.
¹⁴¹⁹ This can be achieved only with a precise heavy flavor tagging and the ability
¹⁴²⁰ to separate the b quarks from the c quarks. Actually, the lifetime of the two
¹⁴²¹ quarks is of the same magnitude (1.3^{-12} s for the b quark and 1.1^{-12} s for
¹⁴²² the c quarks), leading to very close decay vertices.

¹⁴²³ Along this chapter, the role of the vertex detector and the physics re-
¹⁴²⁴ quirements to develop one for the ILC environment will be presented. Then,
¹⁴²⁵ the different options of the International Large Detector (ILD) are shown, to
¹⁴²⁶ focus on the double-sided ladders developed by the Pixelated Ladder with
¹⁴²⁷ Ultra-low Material Embedding (PLUME) collaboration. To finish, the prin-
¹⁴²⁸ ciple of Complementary Metal Oxide Semi-conductor (CMOS) sensors and
¹⁴²⁹ their use in physics are described.

¹⁴³⁰

Contents

¹⁴³¹ 4.1 The ILD vertex detector specifications	50
¹⁴³² 4.1.1 Physics requirements	50
¹⁴³³ 4.1.2 Layout of the vertex detector	52
¹⁴³⁴ 4.2 PLUME	54
¹⁴³⁵ 4.2.1 Design and goals	55
¹⁴³⁶	

1437	4.2.2 Prototypes	56
1438	4.2.3 Perspectives	57
1439	4.3 Integration of CMOS sensors	59
1440	4.3.1 Charges creation and signal collection	60
1441	4.3.2 Pros and cons of the technology	61
1442	4.3.3 Signal processing	62
1443	4.3.4 State of the art in high energy physics	66

1447 4.1 The ILD vertex detector specifications

1448 The VXD is the closest sub-detector to the interaction point (IP) in charge
 1449 of reconstructing the vertex by extrapolating particles back to their origin of
 1450 production. This detector should be optimised to track particles in a high-
 1451 density environment and to be able to extract the tracks from the different
 1452 particles, especially the b and c quarks in the case of the ILC. The recon-
 1453 struction of the displaced vertices should be efficient enough to perform a
 1454 good flavour tagging. Therefore, the detector has to measure particles with
 1455 a lifetime in the picosecond regime, representing a decay length between 150
 1456 and 500 μm . The minimum distance of the first VXD layer is determined
 1457 by the beam pipe radius, and the background induced by beamstrahlung, to
 1458 limit the pixel occupancy. This sub-detector has a central role in the tracks'
 1459 reconstruction. Depending on the option chosen, the VXD has to provide
 1460 five or six points of measurement with a very high precise spatial resolution.
 1461 For the studies requiring vertex charge identification, it should be able to
 1462 reconstruct low-momentum and very forward tracks.

1463 4.1.1 Physics requirements

1464 The ideal VXD should be made of sensors with a fine granularity in order
 1465 to increase the ability to distinguish two nearest particles. The mechanical
 1466 structure of the detector should provide a good stiffness and stability of the
 1467 whole system but has to be at the same time as light as possible to reduce the
 1468 interaction of the particles traversing it, before they reached another part of
 1469 the main detector. As well, in order to reduce the unwanted interactions, the
 1470 sensor technology used has to have a low power consumption to avoid any
 1471 special cooling system which can have a bad impact on the material budget.
 1472 The design of such detector, like the minimal distance of the first layer to

the IP and the spacing between different layers, is determined by both the beam background and the physics to study. The flavour tagging ability, the vertex charge measurement and tracking, and the displaced vertices reconstruction are the main physics parameters driving the design. The distance of closest approach of a particle to the colliding beam is called the impact parameter and the resolution achievable by the detector is described by the formula 4.1[7].

$$\sigma_{IP} = a \oplus \frac{b}{p \sin \theta^k}, \text{ with } k = \begin{cases} \frac{3}{2} & \text{in the } R - \Phi \text{ projection} \\ \frac{5}{2} & \text{in the } z \text{ projection} \end{cases} \quad (4.1)$$

Where θ is the track polar angle, a and b are explained in the following.

The first term a is the impact parameter resolution of the sensors used for the VXD, which is linked up to the radius of the inner R_{int} and outer R_{ext} layers and the single point resolution $\sigma_{s.p.}$, as described in equation 4.2.

$$a = \sigma_{s.p} \frac{R_{int} \oplus R_{ext}}{R_{ext} - R_{in}} \quad (4.2)$$

In the case of the ILD, the single point resolution should not be higher than $\sigma_{sp} \simeq 3\mu\text{m}$, leading to an impact parameter with a resolution of the order of $a \simeq 5\mu\text{m}$.

The second term presented in the equation 4.3, is related to the multiple scattering inducing an uncertainty on the impact parameter. It depends on the charge Z of the impinging particle, the material crossed by the particle $\frac{x}{X_0 \sin \theta}$ and the distance of the innermost layer to the IP. Depending on the momentum or the crossing angle of the incoming particles, the two parameters are more or less important. For low momentum particles or crossing particles with a shallow angle, the b parameter becomes important, while for higher momentum a dominates.

$$b = R_{int} \frac{13.6 \text{MeV}/c}{\beta c} Z \sqrt{\frac{x}{X_0}} \left[1 + 0.036 \ln \left(\frac{x}{X_0 \sin \theta} \right) \right] \quad (4.3)$$

For the ILC purpose, the ILD-VXD should reach an impact parameter resolution better than $5 \mu\text{m}$ and a b parameter better than $10 \mu\text{m GeV}/c$. This precision on these parameters were never obtained before in other experiments. As a comparison, the resolution parameters for the LHC are: $a = 12 \mu\text{m}$ and $b = 70 \mu\text{m GeV}/c$.

1500 **4.1.2 Layout of the vertex detector**

1501 The VXD will be made of 12 cm long ladders arranged cylindrically in con-
 1502 centric layers to form long-barrels surrounding the IP, contrary to the SiD
 1503 vertex detector with a design based on a 5 layers barrel, four endcap disks
 1504 and three additional forward pixel disks[10]. Two different geometries are un-
 1505 der consideration for the ILC-ILD, nevertheless, they are both based on long
 1506 ladders. The first option is based on five single-sided layers with a material
 1507 budget not exceeding 0.11 % of X_0 per layer. The five layers are in a radius
 1508 range varying from 15 mm for the first layer to 60 mm for the last one. The
 1509 second option is based on three double-sided layers. The material budget
 1510 should be less than 0.16 % of X_0 for one detecting face. The mechanical
 1511 structure, which holds the two layers, is 2 mm thick and will be in a radius
 1512 range varying from 15 to 60 mm.

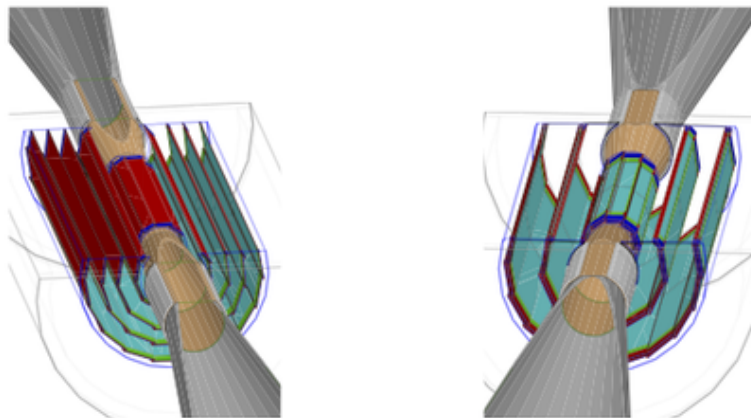


Figure 4.1 – Overview of the two vertex detector option for the ILC. On the left, it is made of five single sided layers, whereas the right one represents three double-sided layers.

1513 Both geometry designs are based on pixel sensors instead of strips detec-
 1514 tors. A non-exhaustive list of the possible technologies are presented below:

1515 **FPCCD**

1516 The Fine Pixels Charged Coupled-Device (FPCCD) [11] is based on the
 1517 Charged Coupled-Device (CCD) processes. The sensor is using small pixels
 1518 size (approximately $\sim 5\mu\text{m}$) to provide a sub-micron spatial resolution and
 1519 an excellent capability to separate two nearby tracks. Its thickness is 50

1520 μm and the epitaxial layer ($15 \mu\text{m}$ thick) is completely depleted to limit
 1521 the charge spreading around pixels and to reduce the number of hits per
 1522 pixel. However, the CCD architecture provides slow readout and the matrix
 1523 will be read between consecutive bunch trains, helping to reduce the power
 1524 consumption and avoiding beam induced RF noise. The FPCCD are planned
 1525 to be operated at -40°C .

1526 DEPFET

1527 The Depleted P- Channel Field Effect Transistor (DEPFET) [41] is an Active
 1528 Pixel Sensor (APS) in which field effect transistors are incorporated into each
 1529 pixel. The single point resolution is $\sim 3 \mu\text{m}$ for pixels with a size of $20 \mu\text{m}$.
 1530 The silicon itself is used as sensitive part but also as a mechanical structure,
 1531 minimising the support and services. The sensor is completely depleted of
 1532 free charged carries thanks to a voltage applied to the thickness. The rolling-
 1533 shutter approach is used for reading each row and the column readout is done
 1534 by two auxiliary Application-Specified Integrated Circuits (ASICs).

1535 The DEPFET technology is the one chosen to build the vertex detector
 1536 of the BELLE-II experiment[2].

1537 CMOS

1538 Different options for CMOS pixel sensors are studied, such as the 3D in-
 1539 tegrated CMOS, but due to the context of this thesis, the work will focus
 1540 on the CMOS sensors based on the Minimum Ionizing MOS Active pixel
 1541 sensor (MIMOSA) architecture developed by the IPHC of Strasbourg. This
 1542 technology is described in section 4.3.

1543 For all the technologies, the sensors' power consumption has to be min-
 1544 imised in a way to reduce the cooling system and in the same time the added
 1545 material budget in the sensitive detector volume. As it was shown on the
 1546 figure 2.2 of the chapter 2, the bunch train will last less than 1 ms for a
 1547 dead time of 200 ms. Two possibilities are envisaged to benefit from the
 1548 beam structure. The first one consists to store the hits information thanks
 1549 to a time stamp during the bunch crossing and to read out the data after
 1550 the last collision. This method might be used by the FPCCD technology
 1551 due to the slow integration time of the CCD. Another solution is to use
 1552 power-pulsing. Right after the last collision, the sensors are switched off or
 1553 the power consumption is reduced as mush as possible, and before the first
 1554 collision, the sensors is switch on again. This pulsing method is studied by
 1555 different collaborations.

1556 Another aspect not discussed yet is the radiation tolerance of the detector,
 1557 which is directly related to the beam background. The first layer is the most
 1558 affected by the background and it should have a high radiation tolerance.
 1559 The required radiation tolerance is about 1 kGy for the total ionising dose
 1560 and a fluence of $10^{11} n_{eq}/\text{cm}^2$ [9].

1561 The efficiency of the VXD has also to be excellent in order to maximise the
 1562 tracking performances. The efficiency is defined here as the ratio of detected
 1563 particles over all the particles crossing the detector. If one layer of the vertex
 1564 detector misses a hit, the track reconstruction will be less accurate

Cooling system¹⁵⁶⁵
 integration time,
 radiation tol-¹⁵⁶⁶
 erance, electro-
 magnetic inter-
 ference¹⁵⁶⁷

To summarise, the expected parameters expected for the ILC are:

- An excellent impact parameter resolution: $a \sim 5\mu\text{m}$ and $b \sim 10\mu\text{m}$
- A material budget not exceeding $0.1 \% X_0$ per layer for the single-sided option ($0.16 \% X_0$ for the double one)
- Radius of the first layer $\sim 15/16$ mm

1571 4.2 PLUME

1572 The Pixelated Ladder with Ultra-low Material Embedding (PLUME) project
 1573 aims to produce double-sided ladder prototypes with respect to the ILC
 1574 requirements[40]. Three labs in the Europe are involved: the IPHC-PICSEL
 1575 in Strasbourg, the University of Bristol and DESY in Hamburg. The collab-
 1576 oration is studying the feasibility to build such vertex detector using MAPS
 1577 thinned down to $50\mu\text{m}$ and is exploring the benefits of this design. Stras-
 1578 bourg is in charge to develop and mount the sensors on the modules, to take
 1579 care of the readout and the Data AcQuisition (DAQ), and to provide a cool-
 1580 ing system. The mechanical design, stability measurements and building the
 1581 ladders are done by the University of Bristol, while DESY has studied the
 1582 ladder mock-up, performed power-pulsing tests and is now characterising and
 1583 validating the modules in the lab. In 2016, DESY has provided the oppor-
 1584 tunity to test the ladder in real conditions thanks to the test beam facility
 and the possibility to use the DAQ software developed at DESY: EUDAQ.

REF: EUDAQ¹⁵⁸⁵

1586 **4.2.1 Design and goals**

1587 The figure 4.2 illustrates the design of a PLUME ladder. The ladder struc-
 1588 ture is defined by the sensors arrangement on the mechanical structure (po-
 1589 sitioned next to each other). In this design, the stiffener is a 2 mm thick
 1590 Silicon Carbide (SiC) foam which has a density varying between 8 % and 4
 1591 % (depending on the ladder version) and could be reduced to only 2 or 3
 1592 %. The choice of this foam is a good compromise between the stiffness and
 1593 the thickness compare to other materials. The figure 4.3 is representing the
 1594 structure of this foam. It is macroscopically uniform and has the advantage
 1595 to be easily machinable. Nevertheless, it has a low thermal conductivity (50
 1596 W/m/K) and can't be used to dissipate the heat. On each side, a low mass
 1597 flex-cable is glued, which is used to connect the sensors for powering and
 1598 managing them. It is made of copper traces coated in Kapton, but new pro-
 1599 tootypes using aluminum traces are developed and currently tested in order
 1600 to reduce the material budget. The ladder embeds twelve sensors, six on
 1601 each face, that are glued and connected to the flex cable. On one edge of the
 1602 flex-cable, a single Zero Insertion Force (ZIF) connector is used to link the
 1603 ladder to the external board servicing, via a jumper cable. For the moment,
 1604 the design is dedicated to the MIMOSA-26 sensors thinned down to $50\mu\text{m}$
 1605 but it can be adapted to any kind of MAPS sensors having the same thick-
 1606 ness. Although the MIMOSA-26 has a spatial resolution better than $3\mu\text{m}$
 1607 (see subsection 4.3.4), the integration time is not suited for the bunch train
 1608 structures of the ILC.

REF Joel paper

1609 The aims of the collaboration are to build ladders with a material budget
 1610 better than 0.35% of X_0 for a spatial resolution better than $3\mu\text{m}$, and thus
 1611 to evaluate the benefits of a double-sided measurement.

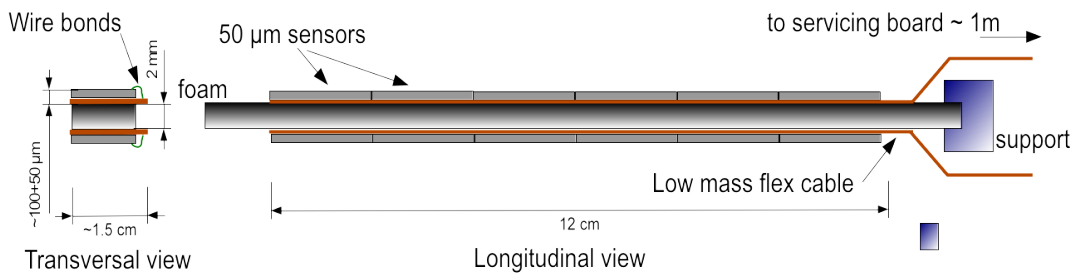


Figure 4.2 – Side view (transversal and longitudinal) of the PLUME me-
 chanical structure.

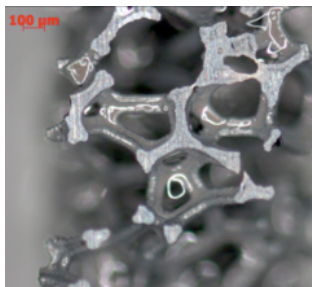


Figure 4.3 – Microscopical view of the silicon carbide foam structure.

1612 4.2.2 Prototypes

1613 Since 2009, the collaboration is studying the design, the production, the
 1614 impact of the mechanical structure on the ladder's performances, but also
 1615 how to power and control the sensors together. The first ladder prototype,
 1616 called version-0 (V-0) was developed and tested in 2009. The purpose of
 1617 this prototype was to settle the fabrication and the test beam procedures,
 1618 without trying to reach the desired material budget goal. Two MIMOSA-20
 1619 analog output sensors were mounted on each side of a stiffener, providing a
 1620 $1 \times 4 \text{ cm}^2$ sensitive area. The prototype was tested in 120 GeV pion beam
 1621 at the CERN-SPS and the results have demonstrated the benefits of the
 1622 double-sided measurement on the spatial resolution, which is improved by
 1623 about 25%[38].

1624 Then in 2010, a second prototype featuring a design closer to the wanted
 1625 goal, called version-1 (V-1), was developed. Each module of the ladder was
 1626 made of Kapton flex-cable with a thickness of 0.14 mm, using copper traces.
 1627 They are denoted Optiprint-Kapton-Flex-cable (OKF), where Optiprint is
 1628 the vendor of these flex-cable. It is the first version to embed six MIMOSA-
 1629 26 binary output sensors working simultaneously on each side of the stiffener.
 1630 The material budget is estimated to be 0.65 % of X_0 in the sensor's sensitive
 1631 area. The aim of this prototype was to validate the operation of multiple
 1632 sensors in a chain. Two ladders were tested in real conditions. The first
 1633 one was tested with 120 GeV pions at CERN-SPS in 2011, while the second
 1634 ladder was tested in April 2016 with up to 5 GeV positrons at DESY in
 1635 Hamburg. The DESY test beam results are presented in chapter ???, while
 1636 a specific study of the sensor's deformation observed at CERN is discussed
 1637 in chapter ???.

1638 At the beginning of 2016, the third prototype versions were mounted but
 1639 have not yet been completely tested. In fact, this new version is divided
 1640 into two sub-versions: one using copper traces and the other one aluminum

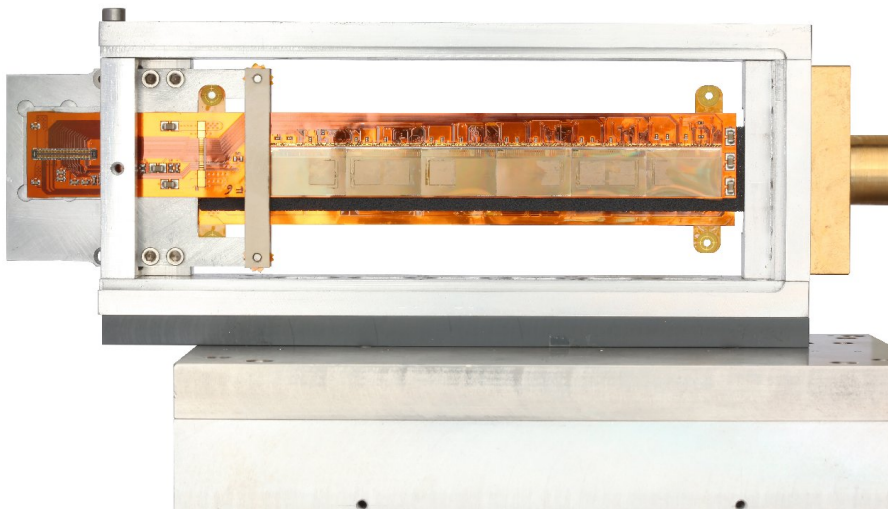


Figure 4.4 – Front view of the ladder version-1 made in 2010 in its holding box. On the left, there is the connector to the output board servicing, on the right a connection to blow air on the module. As this version was not made with a mirrored design, the flexible cables are not entirely overlapping and the SiC foam can be seen (in black here).

traces. Nevertheless, both sub-versions have a new design featuring reduced traces thickness to have a narrower flex-cable (18 mm width) adjusted to the sensors width in order to minimise the dead areas. The flex-design has slightly changed to have a mirrored geometry (figure 4.5) and a straight geometry in order to minimize the dead area too and have a better alignment solution. The stiffener is made of a lower density SiC foam reducing the global material budget.

The table 4.1 summarises the material budget reached by the different prototypes.

4.2.3 Perspectives

Although the collaboration has shown their expertise to build light mechanical structures, more tests and optimisations have to be done. MIMOSA-26 sensors are not designed to match the ILC specs. The integration time of this sensor is 115.2 μ s, whereas the bunch train last only 0.95 ms (bunch

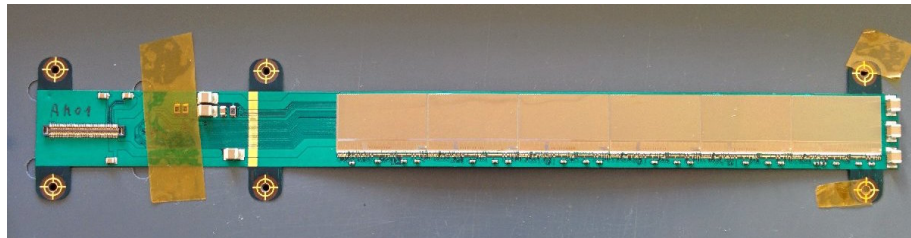


Figure 4.5 – Picture of the first mirrored module made with aluminum traces. The cable width is adjusted to the size of the sensor.

Layer	budget (% X ₀)		
	V-0	V-1	Goal
Sensor	0.053	0.053	0.053
Flex-cable	0.524	0.150	0.034
Passive components	0	0.033	0.033
Stiffener (foam)	0.764	0.175	0.087
Total	1.926	0.654	0.334

Table 4.1 – Estimation of the material budget for the different prototypes of the PLUME ladder.

1655 crossing spaced out by 337 ns), a new CPS with a faster integration time
 1656 has to be integrated. Another problem of the MIMOSA-26 sensors is that
 1657 they are not suited for a power pulsing. As a reminder, the principle of the
 1658 power pulsing is to reduce the consumption of the sensor during the 200 ms
 1659 dead time. Nevertheless, a power-pulsing study on a single Mi-26 sensor has
 1660 been done and the results have shown that the nominal supply voltage of the
 1661 MIMOSA-26 can be lowered from 3.3 V to 1.85 V without losing the sensor's
 1662 registers. The fake hit rate measured was close to the one obtained in normal
 1663 conditions after the sensor reaches a stable operation. Moreover, the power
 1664 consumption was reduced by a factor 6.34[31].

1665 A complete power-pulsing study of the whole ladder in the lab has to be
 1666 done in order to make sure that the sensors are still behaving correctly. If
 1667 the first results are comforting, the power-pulsing will be tested under real
 1668 conditions with a high magnetic field. The impact of the Lorentz forces due
 1669 to the coupling of the power-pulsing and the magnetic field is going to be
 1670 studied, especially is this structure will induce unwanted deformations or
 1671 vibrations.

1672 The collaboration is considering to embed the sensors directly inside the

1673 multi-layer micro-cable[8]. The chips are glued on the first polyimide sub-
1674 strate layer, then the metal layer is deposited on top of it and the metal
1675 traces are directly connected to the chips pads. Then an insulator is added
1676 to the module. The advantages of this technique are, firstly, the direct con-
1677 nection of metal traces to the pads that avoid wire-bonding and can reduce,
1678 at the same time, the width of the module. And secondly, this structure has
1679 the advantage to apply the mechanical stress on the polymer wrapping, thus
1680 reducing it on the sensor.

1681 A closer perspective for the collaboration is to integrate two ladders in
1682 the physics commissioning of the BEAST experiment at KEK. The version-2
1683 ladder will be used but a second option is foreseen. MISTRAL sensors will be
1684 mounted on the flex-cable instead of the MIMOSA-26. These sensors have a
1685 bigger sensitive area, a faster integration time ($\sim 20\mu\text{s}$) but a worth spatial
1686 resolution ($< 10\mu\text{m}$) due to the pixel size (pitch of $36 \times 62.5\mu\text{m}^2$).

1687 4.3 Integration of CMOS sensors

1688 The PICSEL group of the IPHC at Strasbourg is developing since 1999
1689 CMOS sensors called MIMOSA for *Minimum Ionizing MOS Active pixel sen-*
1690 *sor*. They are semi-conducting pixel sensors based on the APS, an alternative
1691 to the CCD developed at the beginning of the 1990's by the imaging industry
1692 and used nowadays for the smartphone's cameras. One particularity of the
1693 sensors developed by Strasbourg is that the different region of the CMOS,
1694 such the sensitive area or the electronic layer where the signal is processed,
1695 are made of the same material. This device is called then Monolithic Active
1696 Pixel Sensor (MAPS) and the different layers are:

- 1697 • A substrate providing a mechanical stability;
- 1698 • An epitaxial layer which is the sensitive volume of the sensor;
- 1699 • An electronic layer where are located the diodes collecting the charges
1700 and the microelectronic processing the signal.

1701 The motivation to use this technology or any other silicon sensor in par-
1702 ticle physics is due to the minimum energy needed to create an electron/hole
1703 pair by a traversing particle. In silicon, this minimum energy is only 3.6 eV,
1704 while for a gaseous detector, it is close to 30 eV.

1705 **4.3.1 Charges creation and signal collection**

1706 The CMOS sensor can detect crossing particles thanks to their structure, but
1707 also to the interaction of particles with matter. When a particle is traversing
1708 a layer of matter, it loses energy via interactions with electrons and nuclei.
1709 Due to the size of a MAPS, it loses only a small fraction of its energy, and
1710 the energy loss can be described by a Landau. A Minimum Ionizing Particle
1711 (MIP) creates 80 electrons per microns inside the silicon.

1712 At the beginning, the microelectronic industry has insulated the transis-
1713 tors from the substrate thanks to a high resistivity layer, called the epitaxial
1714 layer. The development of CMOS sensors was accelerated due to the prop-
1715 erties offered by these semiconductors.

1716 The CMOS sensors developed by the IPHC at Strasbourg are called mono-
1717 lithic MAPS sensors because the different layers of the sensor are made in
1718 one block of the same material, but with different doping. The structure of
1719 the sensor is a highly doped P+ substrate made of a moderate quality silicon.
1720 The crystal structure contains a lot of defects, hence the recombination rate
1721 of charge carriers is high. Above the bulk, a low-doped P- layer is grown.
1722 The silicon used has a good quality, thus the charge carriers have less chance
1723 to recombine. It is the sensitive part of the sensor and is called the epitaxial
1724 layer. On top of it, an N-well implant has the role of the charge collection.
1725 The interface between the N-wells and the epitaxial layer forms a P-N junc-
1726 tion called a collection diode. A depleted area is created by this junction,
1727 on which the charge carriers are attracted. Nevertheless, this P-N junction
1728 is only one part of the pixel. Next to the N-well implants are sitting highly
1729 doped P-well in charge to reflect the charge carriers to the implants. The
1730 difference of doping between the bulk and the epitaxial layer is also used to
1731 reflect the charge carriers to the collection diode.

1732 The typical doping concentration are 10^{15} at/cm³ for the epitaxial layer,
1733 10^{19} at/cm³ in the substrate and 10^{17} at/cm³ for the other layers. The doping
1734 concentration defines the size of the depleted region. For this doping con-
1735 centrations, only a small region around the P-N junction is depleted, while
1736 the epitaxial layer is mainly undepleted. As no external voltage is applied
1737 to the sensor to increase the depleted region, the charge carriers created by
1738 crossing particles are thermally diffused into the epitaxial layer to the diode.
1739 Nevertheless, the different doping levels produce a built-in voltage defined
1740 as:

$$V_b = \frac{kT}{q} \ln \left(\frac{N_{p+}}{N_{p-}} \right) \quad (4.4)$$

1741 The built-in voltage depends on the Boltzmann constant k , the temperature T , the elementary charge q and the different concentrations doping
 1742 $N_{p\pm}$ of the interface. Due to the different doping levels, the electrons are
 1743 restricted to diffuse inside the sensitive volume, to be then guided towards a
 1744 collection diode. One effect of the thermal diffusion is that the average path
 1745 of the electrons in the epitaxial layer is longer than the one they would have
 1746 in a fully-depleted sensor. Hence, the probability of recombination between
 1747 an electron and a hole is increasing. Also, the charges tend to spread more
 1748 around neighboring n-well. Therefore, the charge collection efficiency is lower
 1749 than the fully-depleted sensor.
 1750

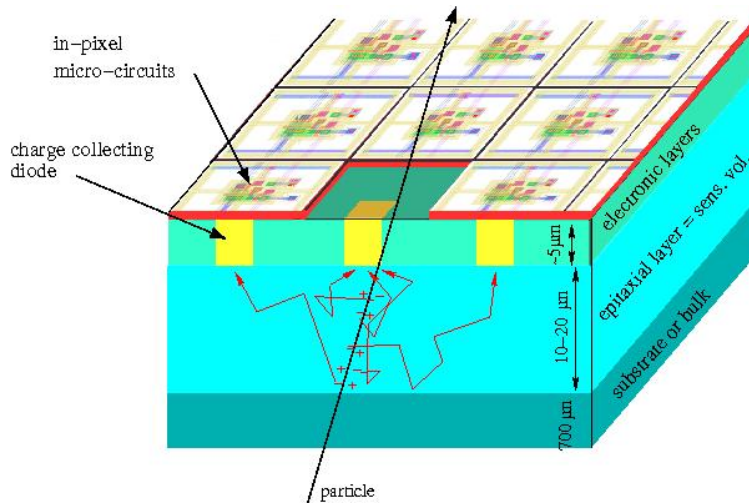


Figure 4.6 – Drawing of MAPS structure representing the different layers of the sensor and the path of charge carriers in the epitaxial layer.

1751 4.3.2 Pros and cons of the technology

1752 The CMOS sensors have several interesting properties. First of all, the fab-
 1753 rication cost is lower than other pixel technologies due to the industrial pro-
 1754 cesses used to build the sensors. Therefore, many prototypes and bigger
 1755 matrices can be built, while benefiting from the industrial experience. For
 1756 example, the imaging industry has developed smaller and smaller grid size
 1757 and a pitch size of ten microns can be achieved.

1758 Secondly, due to the size of the depleted area, the charge carriers tend to
 1759 spread more over neighboring pixels. On the one hand, the signal collected
 1760 per pixel is smaller, but on the other hand, the reconstruction of the hit

1761 position with a centre of gravity algorithm is improving the spatial resolution.
 1762 To give an idea, a binary output sensor with a pitch of $18.4 \mu\text{m}$ can achieve
 1763 a spatial resolution better than $3 \mu\text{m}$.

1764 Thirdly, the distinct doping of the different layers is responsible for the
 1765 reflection of the charge carriers to the collection diodes. However, only the
 1766 interface between two different doped regions is responsible for this reflection.
 1767 Thus, the substrate can be thinned down to few microns leading to a sensor
 1768 with a thickness of $50 \mu\text{m}$, while keeping the possibility to manipulate them.
 1769 In this way, the material budget can be reduced down to $0.053\% X_0$.

1770 Nevertheless, the thickness of the epitaxial layer (usually between 10 and
 1771 $15 \mu\text{m}$) and the small depleted region are responsible for a small charge col-
 1772 lection. As a matter of fact, a MIP is creating 80 electron/hole pairs per
 1773 microns, so the number of charges collecting by the diode is of the order of
 1774 a thousand electrons. Hence, the signal created is only a few millivolts and
 1775 low noise electronics have to be used for processing the signal.

1776 CMOS sensors are sensitive to ionizing and non-ionizing radiations that
 1777 degrade the sensor properties. The non-ionizing radiations are damaging the
 1778 crystal structure of the epitaxial layers, creating defaults in the lattice. The
 1779 recombination rate is increasing and reduces the signal collected. To avoid
 1780 this effect, two solutions are possible. The first one is to reduce the size of
 1781 the pixels in order to decrease the path of the particles from the epitaxial
 1782 layer to the collection diodes. Nevertheless, the cost to build sensors with a
 1783 smaller pitch is increasing. The second solution is to increase the resistivity
 1784 of the epitaxial layer to expand the depleted area.

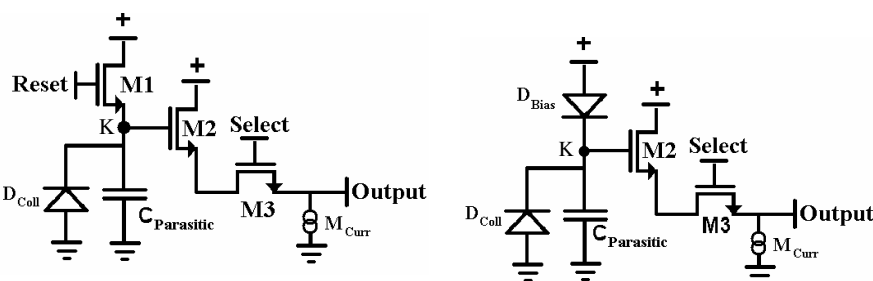
1785 The ionizing radiations are responsible for charges accumulation in the
 1786 electronic layer. The leakage current is increasing in the pixel and diode
 1787 collection. To reduce the leakage current, smaller diodes can be used to
 1788 reduce the impact of the leakage current but as it was explained before, the
 1789 cost of fabrication is increasing.

1790 4.3.3 Signal processing

1791 If no charge is collected by the pixel, the voltage at the equivalent capac-
 1792 itor of the diode is evolving because of the leakage current inherent in the
 1793 junction. The pixel reading can be done in two different ways, depending
 1794 on the method used to minimise the leakage current effect. Currently, two
 1795 pixel's architectures are used to compensate the diode's leakage current: the
 1796 *3 Transistors pixel design*, mainly used in imaging, and the *self-biased pixel*
 1797 *design*. The circuit diagram which is shown on the figure 4.7 represents the
 1798 two methods to design pixel.

The first one, presented on figure 4.7a, consists to reinitialise the collection diode's voltage to a reference voltage thanks to a *reset* transistor, denoted M1 on the diagram. This method works in two steps. Firstly, the M1 transistor is closed and the charge of the equivalent capacitor C_d associated to the junction P-N, represented by a diode on the diagram, is slowly decreasing because of the diode's leakage current. During this phase, the pixel is sensitive and is read. After a time interval equivalent to the integration time of the sensor, the transistor M1 is opened to recharge C_d to its initial voltage. During this time, the pixel is not sensitive. While M1 is used for the reset, M2 is used as a pre-amplifier of the signal created by the diode and M3 link up the voltage to the output of the circuit. Although this compensation method is fast, it generates a dead time for detection between two readings.

The figure 4.7b depicts the *self-biased pixel design* method[17]. It is using a P-N junction (symbolised here by a diode mounted on the other side) coupled to the N-well implant to absorb the leakage current. The inverted diode is continuously compensated the diode's leakage current, thus the dead time vanishes. While no particle is crossing the sensor, an equilibrium appears between the leakage and recharge current. A particle going through the sensor disrupts this equilibrium. The charges collected by the pixel lead to a discharge of the diode's capacitor C_d , followed by a recharge of this capacitor thanks to the second diode to reach again the equilibrium. Nevertheless, if the recharge procedure is too fast compare to the integration time, the physics signal is masked and the passage of the particle is never notified. Even if the time interval to recharge the capacitor C_d is set properly, an important charge collection per pixel could disturb the recharge phase and the pixel will reach a stable level again only a long time interval of the order of 10 ms.



(a) Three transistors (3T) pixel design.
(b) Self-biased pixel design.

Figure 4.7 – Two different architectures of pixel.

1826 Integration time and readout

1827 For a non-depleted epitaxial layer, the charge carriers are thermally diffused
1828 to the collection diodes. The time to collect these charges in a pixel is ~ 100
1829 ns, setting a maximal limit to read the signal. This integration time is not
1830 reachable due to other factors, like the pixel occupancy or the time needed
1831 to obtain the information of all the pixels. Also, a compromise to reach fast
1832 integration time has to be done. Faster is the sensor, more important is the
1833 power consumption of the electronic. Moreover, to reduce the integration
1834 time, a solution consists of increasing the size of the pixels. In consequence,
1835 the pointing resolution of the device is impacted. For the case of the ILC,
1836 the integration time is dictated by the pixel occupancy that should not be
1837 bigger than a percent, to stay in the using sensor's range and to be able to
1838 reconstruct the impact.

1839 The first sensors developed were using an analog output. With this ap-
1840 proach, the pixels were addressed sequentially and their output was multi-
1841 plexing in one bus line. The advantage of such method is that the discrimina-
1842 tion can be adjusted offline for each pixel, thus compensating the nonuniform
1843 response. Nevertheless, the integration time is depending on the operational
1844 frequency of the bus (usually 50 MHz) and the number of pixels contained
1845 in a matrix. For a sensor having millions of pixels, the integration time is
1846 then of the order of the millisecond. An analog output is then too slow for a
1847 ILC purpose.

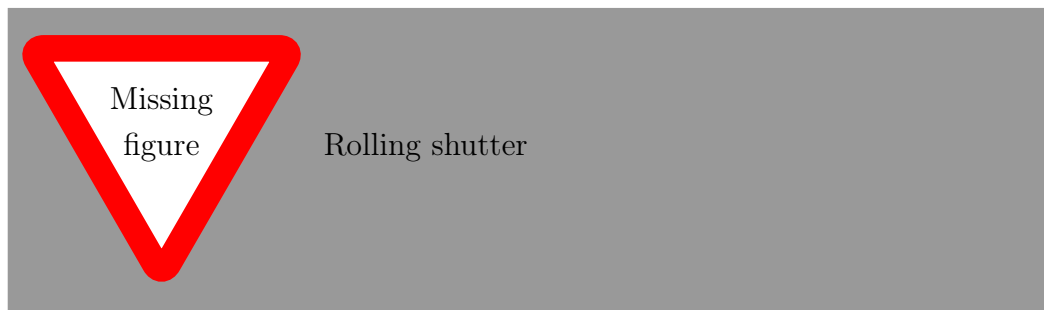


Figure 4.8 – Parallel column readout.

1848 To overcome this problem, an approach is to group the pixels in columns
1849 and to read them in parallel. The figure 4.8 depicts the principle of this
1850 method called *column parallel readout* or *rolling-shutter*. Instead of having
1851 one bus line for the whole matrix, each column has its own bus and a data
1852 sparsification logic is integrated on the periphery of the sensor. One row is

1853 read out between 100 ns and 200 ns, independently to the number of pixels
 1854 contained in it. In consequence, a matrix containing thousands of rows has
 1855 an integration time of $\mathcal{O}(100\mu\text{s})$. Moreover, to increase the integration time
 1856 an output memory is duplicated at the periphery of the sensor. Hence, when
 1857 one line is read, the precedent one is processed by the electronics at the end
 1858 of each bus line of each column. To minimise the data bandwidth, only the
 1859 pixels above certain thresholds are read thanks to discriminators coupling to
 1860 a zero suppression logic, called Suppression de zéro (SUZE). In this way, only
 1861 the address of the first pixel hit in a row and the number of the adjacent fired
 1862 ones are stored. This memory is duplicated to be able to process one row,
 1863 while the previous one is read out by the outside world. In order to increase
 1864 the readout speed, two techniques are conceivable[46]. The first one provides
 1865 elongated pixels in the vertical direction in order to reduce the number of
 1866 rows, thus degrading the spatial resolution in the same direction. The second
 1867 one consists of dividing the columns into two distinct parts, which have its
 1868 dedicated output.

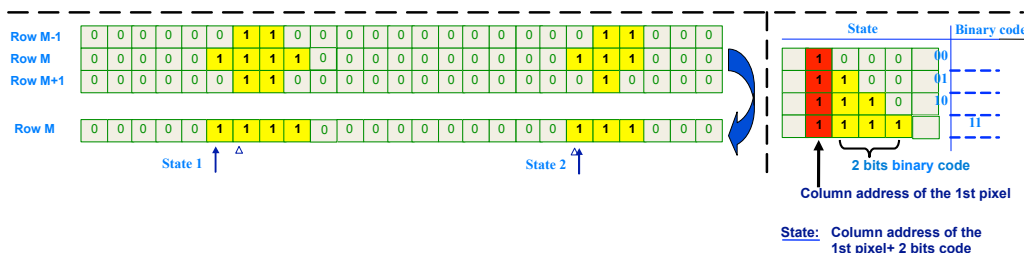


Figure 4.9 – Principle of the zero suppression logic.

Noise

1869 The CMOS sensors are sensitive to the noise. Many factors are causing it and
 1870 the different kind of noise is divided into two categories: the Fixed Pattern
 1871 Noise (FPN) and the Temporal Noise (TN). The non-uniformity responses
 1872 of the pixel in a sub-array is responsible for the FPN and is regarded as an
 1873 offset or pedestal, which is subtracted from the pixel response to reduce the
 1874 impact of this noise. The TN has different origins, as the shot noise, the
 1875 pink noise or the thermal noise. The different operational phases to read the
 1876 signal are contributing to the noise.

1877 One contribution to the TN appears in the *3T pixel design* only during
 1878 the reset phase. This noise arises when the transistor is open restoring the
 1879

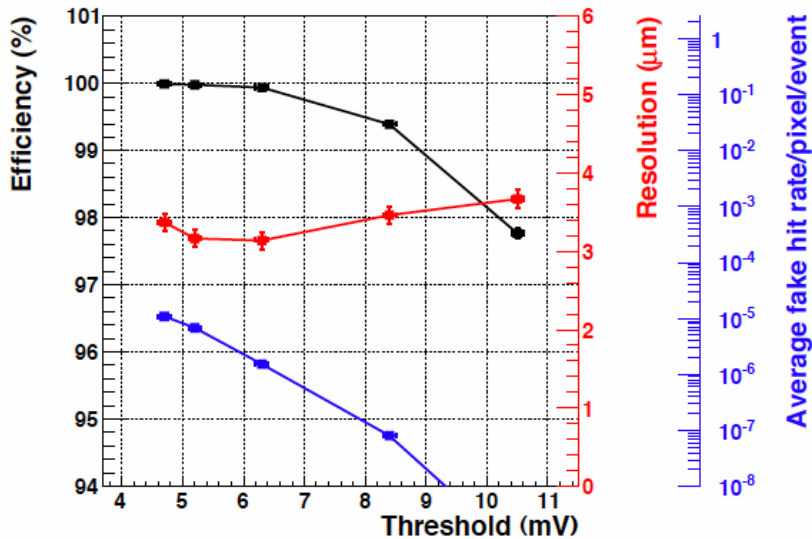


Figure 4.10 – Plots representing the efficiency, the fake hit rate per pixel and the spatial resolution as a function of the discriminator threshold.

charge of the capacitor associated with the collection diode. It is dependent on the temperature and the diode's capacitance.

The second one is the noise during integration and is caused by statistical fluctuations of the leakage current (shot noise). Faster is the integration time, slower is the shot noise contribution.

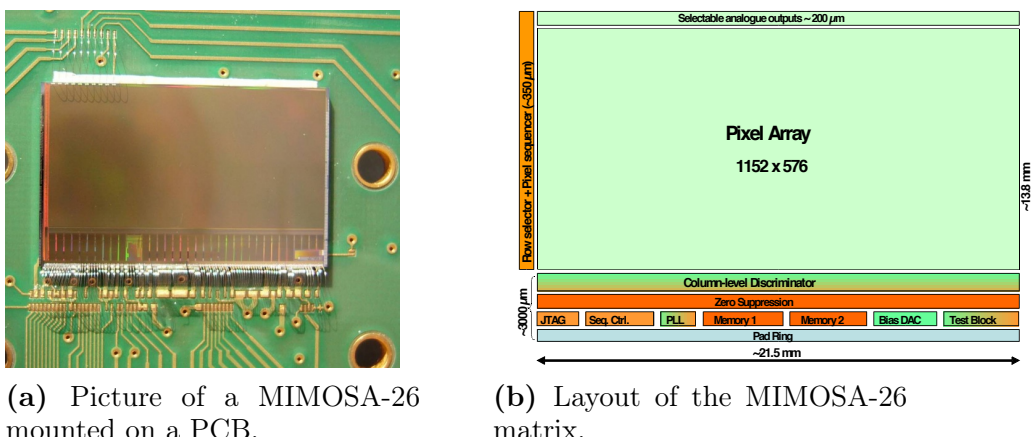
Finally, the third one arises from the readout, while the column switch and the source follower capacitors are working. This noise depends on the contribution of each capacitor.

To remove the FPN and the reset noise, a Correlated Double Sampling (CDS) is performed inside the pixel or at the bottom of the column. It consists to acquire two frames and to subtract the first one to the second one to search for possible signals. The chapter 5 describes the steps to characterise the FPN and TN and to select an appropriate Signal to Noise ratio (SNR) in order to minimise the noise contribution, and to find a range on which the sensor is working properly.

4.3.4 State of the art in high energy physics

The first full-scale digital sensor developed by the PICSEL group was the MI-MOSA-26. They were designed to equip the reference planes of the EUDET

beam telescope and are used since 2010 to build the PLUME prototypes. It is fabricated in the AMS $0.35\mu\text{m}$ technology, and has a matrix containing approximately 6.6×10^5 pixels, distributed in 1152 columns and 576 rows. The pixel pitch is $18.4\mu\text{m}$ and the sensitive area represents $21.2 \times 10.6\text{cm}^2$. The readout of the matrix is ensured by a rolling-shutter working at 80MHz frequency, hence the integration time is $115.2\mu\text{s}$. The signal produced by the charge collection inside the pixel is firstly amplified. Then, the CDS technique is used to subtract successive frames before to send the signal at the bottom of the pixel array, where the signal processing circuitry is placed. Analog to digital conversion is done, coupled to a second double sampling, in order to reduce the FPN. The output of the discriminators is then connected to a zero suppression logic, in which an output memory is duplicated to ensure a continuous readout. The signal is finally transmitted to the outside world. The architecture of the MIMOSA-26 is represented by a block-diagram on figure 4.11b. The power consumption is $1.1\mu\text{W}/\text{pixel}$ and the sensor is thinned down to $50\mu\text{m}$ in order to minimise the multiple scattering inside the volume. The performances obtained with a MIMOSA-26 are shown on the figure 4.10.



(a) Picture of a MIMOSA-26 mounted on a PCB.

(b) Layout of the MIMOSA-26 matrix.

Figure 4.11 – Block-diagram and a picture of the MIMOSA-26

The PICSEL group has then developed digital output sensors for the pixel vertex detector at the STAR experiment at Brookhaven National Laboratory[1]. The figure 4.12 is showing a half-section of the STAR vertex detector (subfigure 4.12a) and a MIMOSA-28 bounded on a PCB(subfigure 4.12b). They are based on the architecture of MIMOSA-26 with some modifications. The matrix contains 960 columns and 928 rows for a pitch of $20.7 \times 20.7\mu\text{m}^2$. The sensitive area is $19.7 \times 19.2 \text{ cm}^2$, for an integration time of less than $200\mu\text{s}$. The sensor can reach a particle detection rate of 10^6 particles/ cm^2/s .

¹⁹²³ Finally, their power consumption is lower or equal to 150 mW/cm^2 . The
¹⁹²⁴ spatial resolution obtained for ULTIMATE is less than $4 \mu\text{m}$.

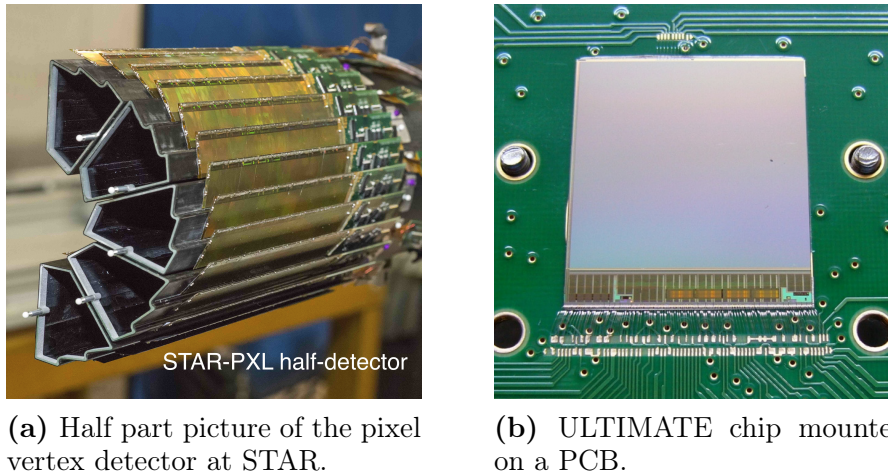


Figure 4.12 – Pictures of the STAR vertex detector and an ULTIMATE chip

¹⁹²⁵ This chapter has depicted the purpose of the vertex detector for the ILD.
¹⁹²⁶ Different technologies were introduced, to focus specifically on the CMOS
¹⁹²⁷ sensors and their use in high-energy physics. The PLUME collaboration
¹⁹²⁸ aims to integrate MAPS onto light double-sided ladders, in order to reach
¹⁹²⁹ the requirements of the ILC. The collaboration has reached different steps to
¹⁹³⁰ produce the first full-scale ladder, which have only a material budget of
¹⁹³¹ only $0.35\%X_0$ and a spatial resolution better than $4\mu\text{m}$. The principle of
¹⁹³² the CMOS technology was presented. The next chapter is focusing on the
¹⁹³³ electrical validation of this sensors mounted onto a PLUME ladder.

¹⁹³⁴ Chapter 5

¹⁹³⁵ Basic assessments

¹⁹³⁶ The chapter 4 has described the PLUME project with the different prototypes that were built. Since the version-1 of PLUME, the ladder has a more
¹⁹³⁷ complicated electrical scheme due to the six sensors on each module. The
¹⁹³⁸ flex-cable used has a lot of thin metal layers connected to the sensors. The
¹⁹³⁹ synchronisation, as well the powering and data transmission of the chips have
¹⁹⁴⁰ to be work without any problem. Before performing a test under real conditions
¹⁹⁴¹ at test beams CERN or at DESY, the device has to be validated and
¹⁹⁴² characterised in the lab. This chapter is introducing the different steps from
¹⁹⁴³ the assembly procedure performed at Strasbourg (for the module) and Bris-
¹⁹⁴⁴ tol (for a complete ladder), to the final tests to study the sensors response,
¹⁹⁴⁵ and include electrical functionality tests at Hamburg.

¹⁹⁴⁷ Contents

¹⁹⁴⁸ 5.1	PLUME assembly procedures	70
¹⁹⁴⁹ 5.1.1	Module and ladder assembly	70
¹⁹⁵⁰ 5.1.2	Visual inspections	72
¹⁹⁵¹ 5.2	Electrical validation	73
¹⁹⁵² 5.2.1	Auxiliary board	73
¹⁹⁵³ 5.2.2	Smoke test	75
¹⁹⁵⁴ 5.2.3	JTAG communication	78
¹⁹⁵⁵ 5.3	Noise measurements	79
¹⁹⁵⁶ 5.3.1	Characterisation bench	79
¹⁹⁵⁷ 5.3.2	Threshold scan	81
¹⁹⁵⁸ 5.3.3	Noise measurements	84
¹⁹⁵⁹		

1960	5.4 Conclusions	86
1961		
1963		

1964 5.1 PLUME assembly procedures

1965 The ladders are built in two steps. Firstly, two independent modules are
 1966 assembled at Strasbourg, then tested at DESY, afterward, they are shipped
 1967 to Bristol where the modules are glued together on a SiC foam to form a
 1968 PLUME ladder. The assembly procedures are introduced below, as well as
 1969 the visual inspection between the mounting steps.

1970 5.1.1 Module and ladder assembly

1971 Module assembly

1972 The module assembly is performed at the IPHC by the microelectronics
 1973 group and is done in three steps. First of all, the passive components are
 1974 soldered onto a flex-cable. Then, an epoxy layer with a thickness of 300 μm
 1975 is applied under the connector side. Due to the force applied by pulling and
 1976 pushing the jumper cable on the ZIF connector, the epoxy layer has the role
 1977 to reinforce this area and to avoid the flex-cable to be damaged. The module
 1978 is then placed on a metal jig to ensure its flatness using a vacuum suction.
 1979 The next step consists of gluing the six sensors onto the flex. The positioning
 1980 of the chips was used to be done manually, but a programmable robot which
 1981 has a maximum mismatch alignment reaching approximately 20 μm is now
 1982 used for this procedure. As the sensors are thin and fragile pieces, their
 1983 are manipulated with a vacuum sucker. Few drops of glue are dispensed on
 1984 the flex and then, the sensors are gently pressed one by one on top of it to
 1985 be glued. Afterward, the glue is cured in an oven and the chips cannot be
 1986 removed anymore. If a sensor is not working properly, it can not be replaced
 1987 by a new one because the force needed to remove it might break the fragile
 1988 flex-cable. On the worse case scenario, a new sensor can be glued on top of
 1989 it, but this solution cannot be envisaged for a real ladder as it increases the
 1990 material budget locally.

1991 In order to avoid this situation, the sensors are probe-tested at the IK
 1992 in Frankfurt, to select only the good ones before the module assembly. The
 1993 final step consists of soldering the 540 wire-bonds (a single MIMOSA-26
 1994 requires 90 wire-bonds) using a semi-automatic machine. The wire-bonds
 1995 can be protected by applying a glob-top epoxy. It has the advantage to offer

1996 a protection against moisture or contaminants, an electrically insulation and
 1997 prohibits their movement during other manipulations (see 5.1.2 for the utility
 1998 of the glob-top epoxy). Nevertheless, it increases the material budget locally
 1999 and if an electrical problem occurs, the wire-bonds can't be disconnected.
 2000 When the module is assembled, it is finally transferred onto a plastic sole,
 2001 which has alignment pins. This sole helps to manipulate the modules, but
 2002 also reduces the stress on the flex-cable, by holding it as flat as possible.
 2003 During shipping, a plastic cover is screwed on top of the sole to protect
 2004 completely the module.

2005 Ladder assembly

2006 The ladder assembly is performed by the Bristol team. It consists of two
 2007 modules together on a spacer (SiC) and a bate (an aluminum plate). The
 2008 operation is done entirely by hands. Each module is placed on a separate jig
 2009 containing grooves and alignment pins to ensure the positioning, as presented
 2010 on figure 5.1a. The sensitive side of the module is facing the jig to have an
 2011 access to the rear of the flex-cable for the gluing procedure. Then, the foam
 2012 is placed on one module below the sensors, while the bate is glued below the
 2013 connector with an overlap on the foam (see figure 5.1b) The second module
 2014 receives some glue on the backside before the jigs are assembled together.
 2015 The glue is then cured for one day. The amount of glue needed for the
 2016 assembly was studied carefully. Indeed, the surface of the foam is irregular,
 2017 so if not enough glue is used, the foam will not be glued on the module. On
 2018 the other hand, using too much glue might stick the jigs together. When the
 2019 ladder is finally ready, it is placed into an aluminum box used for shipping
 2020 but also testing.

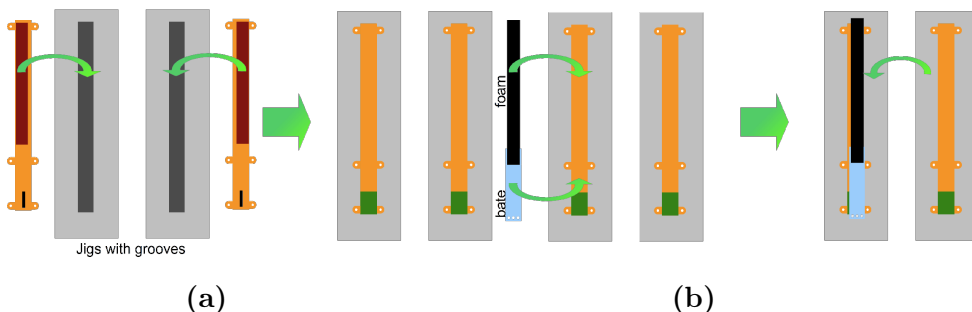


Figure 5.1 – Drawing of the ladder assembly. The modules are first placed on the jigs, sensors facing the grooves 5.1a, then the foam and the bate are glued between the two modules 5.1b.



Figure 5.2 – Visualisation of the alignment. The distance between the two edges is $\sim 51 \mu\text{m}$.

2021 5.1.2 Visual inspections

2022 As explain in subsection 5.1.1, the sensors positioning was performed firstly
 2023 manually and later was switched to an automatic procedure. To tune prop-
 2024 erly the robot which is in charge of gluing the sensors on the flex-cable, the
 2025 microelectronic group needs a position feedback. The modules are then in-
 2026 spected under a microscope to measure the gap between two sensors, and
 2027 their position relatively to each other. The distance between the last pixel
 2028 of a sensor to the neighboring one should be less than $500 \mu\text{m}$, taking into
 2029 account the $20 \mu\text{m}$ robot's mismatch. The figure 5.2 is a picture taken with a
 2030 microscope showing the relative position of two sensors on the bottom of the
 2031 matrix for an aluminum straight module. The gap between the two edges is
 2032 $\sim 51 \mu\text{m}$.

2033 The visual inspection is also needed to check if the wire-bonds are cor-
 2034 rectly connected to the right sensor's pad, to verify that the gluing of the
 2035 sensors on the flex-cable did not break the matrix due to some dust and also
 2036 to control that the shipping of the module between the labs (for example
 2037 between Strasbourg and DESY) did not damage it. The modules are fragile
 2038 objects that have to be manipulated with care. Any wrong manipulation can
 2039 damage severely the vital functionality. For example, the figure 5.3 shows
 2040 a picture taken with a microscope of wire-bonds crashed due to a falling
 2041 cable on it. The sensitive part and the electronics were not damaged, but
 2042 some wires were touching leading to a shortcut. Fortunately, the microelec-
 2043 tronic group at Strasbourg was able to unbend the wires and repair the most

2044 damaged one. This module is fully operational and working correctly.

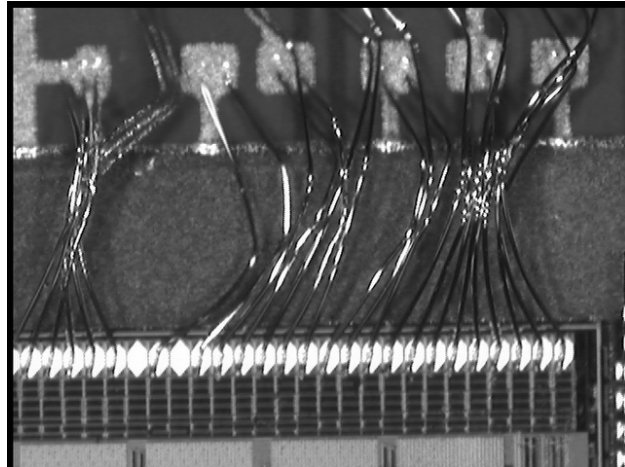


Figure 5.3 – Picture taken with a microscope showing wire-bonds crashed due to a falling cable. Some of the wire-bonds are in contact leading to a shortcut and a non-functional module.

2045 5.2 Electrical validation

2046 The electrical validation of a PLUME module or ladder is performed in two
2047 steps. The first one consists of checking that all the system controlling and
2048 powering the module is working. Then, the module is connected and its
2049 consumption, as well as the communication, are checked.

2050 5.2.1 Auxiliary board

2051 A module or a PLUME ladder is connected to the outside world by plugging
2052 a jumper cable on a ZIF connector at one edge of the module. This jumper
2053 cable is linked to an auxiliary board which powers the sensors of the module,
2054 but also pilots them and to transfer the data to the data acquisition system.
2055 This auxiliary card is connected to a power supply board which provides the
2056 nominal voltages needed by the sensors. The power supply board delivers
2057 the digital and analog voltages (V_{DD_D} and V_{DD_A} are set to 3.3 V using two
2058 independent potentiometers), the buffers voltage V_{CC} fixed to 3.3 V, as well
2059 for the temperature measurement diodes, a ± 5 V for trigger and a power

pulsing signal. For the lab tests to validate the module, the power pulsing is deactivated by connecting this pin to the +5 V pin of the trigger. The clamping voltage V_{clp} used for the polarisation of the pixel has to be in the range [2, 2.2] V. On the first version of the auxiliary board, it was provided by an external power supply, but the new version delivers the 2.1 V needed by using an I2C chips or a potentiometer (the user can select which methods to use thanks to a jumper). The auxiliary board is also connected to a computer in charge of the sensors' slow control. Two RJ45 are providing the Joint Test Action Group (JTAG) registers, as well as the start and reset signal. For a complete ladder, the two modules have to be synchronised and the clock can be injected by a clock distribution board. One RJ45 connector is dedicated to the JTAG slow control and the signals delivered are:

- **Test Data In (TDI)**: received the serial data input feed to the test data registers or instruction register
- **Test Mode Select (TMS)**: controls operation of test logic (for example, by selecting the register)
- **Test Clock (TCK)**: uses to load test mode data from TMS pin and test data on TDI pin at the rising edge, while at the falling edge, it is used to output the test data on the TDO pin.
- **Test Data Out (TDO)**: the output data feed the input data of the next sensor and the last sensor sends the information back to the computer

The second RJ45 connector is providing signal coming from the DAQ:

- **Clock**: has a rate of 80 MHz and is provided by the clock distribution board to synchronise two modules together
- **Start**: signal provided by the DAQ software to start and synchronise multiple sensors (the JTAG start works only for one sensor).
- **Reset**: reset the registers to default value.

The principle of the connection between the auxiliary board and the different components to operate one module is depicted on the figure 5.4.

Before connecting a PLUME module to the auxiliary board, the voltages have to be set and the JTAG communication has to be checked on the auxiliary card. Two external power supplies are delivering 8 V D.C. to the

power supply board and are giving an information on the consumption of the whole system. The empty auxiliary board has a current consumption about 350 mA. Then, the V_{CC} , V_{DD_d} and V_{DD_a} should be at 3.3 V, but only the two last voltages can be adjusted thanks to two potentiometers on the power supply board. The V_{clp} is set to 2.1 V and should not be outside the range [2, 2.2] V. The JTAG communication is verified thanks to a probe linked to an oscilloscope. The observed signals should be:

TDI:

TDO:

TMS: by default is fixed to 1 and change to 0 at every register selection

TCK: this clock is slower (30 kHz) than the 80 MHz needed by the sensors and is only dedicated for the slow control

Reset: by default is fixed to 1 and should change to 0 every time the reset is called by the JTAG software

Start:

Clock: Independently of the method used, the 80 MHz clock has to be correctly distributed along the auxiliary card

5.2.2 Smoke test

After the validation of the auxiliary board (and the power supplies switched off), the module can be linked to it via a jumper cable. The voltages applied to the device have to be adjusted again due to the dissipation inside the flex-cable and the jumper cable. The V_{DD_D} , V_{DD_A} and V_{clp} can be measured on different pads of the ladder: three pads are closed to the connector, while the three others are at the edge of the flex-cable, as seen on the figure 5.5

Two versions of the jumper cable were produced, one very flexible with a high resistivity and the second one stiff with a low resistivity. The most flexible cable was not used because of an important voltage drop between the auxiliary board and the module, but also because of a wrong fabrication. Indeed, after setting the voltages to the nominal value and plug in the module, a short-circuit happened. The auxiliary board tests were correct and were proofed one more time without the module. Then, a thermal camera was used to find if a sensor was responsible for the short-circuit. One sensor was

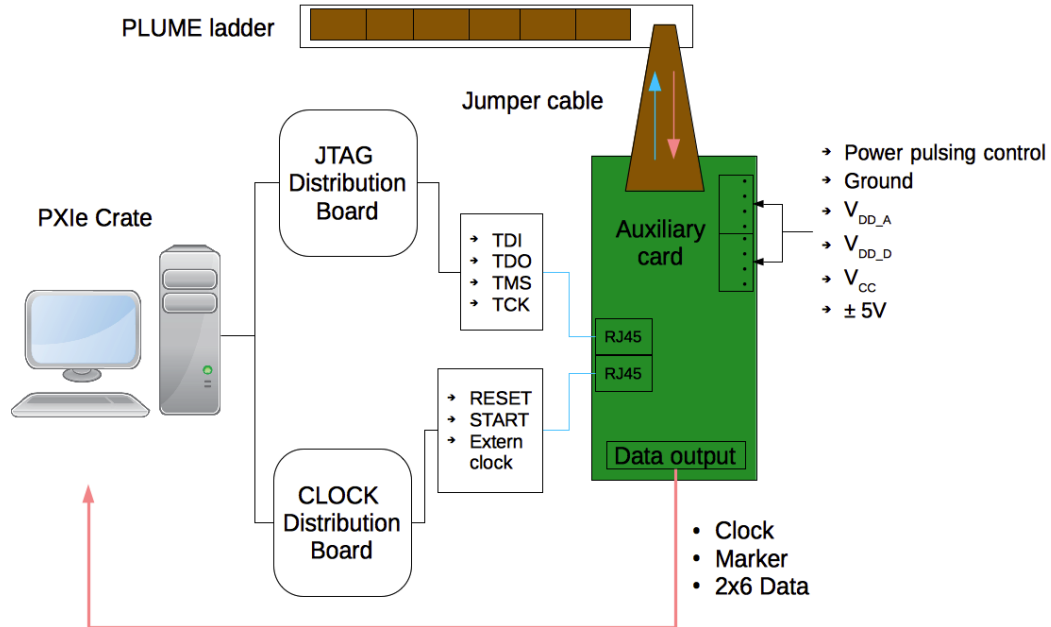


Figure 5.4 – Sketch of the PLUME connection.

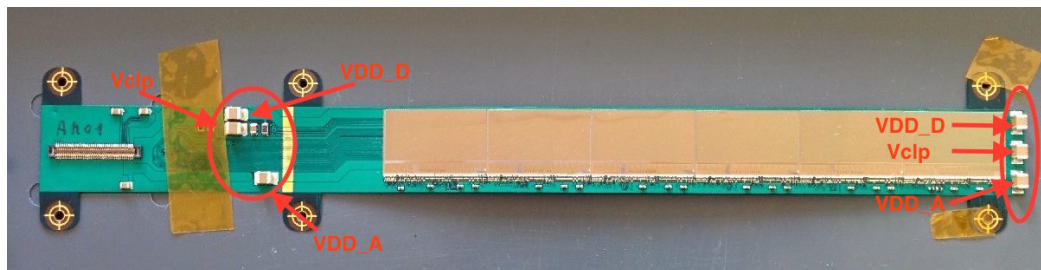


Figure 5.5 – Picture of a aluminum mirrored module with the points of measurement for V_{DD_D} , V_{DD_A} and V_{clp} .

hotter than the others, nevertheless, the wire-bonds were correctly assigned.
 The problem was coming from a short-circuit between the V_{DD_D} and the
 V_{clp} . By passing this two lines on the jumper cable and by connecting them
 directly to the module, the short was gone. Instead of this flexible jumper
 cable, a stiffer one was used. Nonetheless, any movement of the auxiliary
 board causes a too important stress on the connector and on the flex-cable.

2131 To avoid any damage, a support was built to hold the auxiliary board and
2132 the module on the same frame, thus reducing the risk to break anything.

2133 The module consumption is checked at every JTAG steps to make sure
2134 that no short-circuit occurs. Right after powering-on the system, the six
2135 sensors are starting in a random state and the consumption at this stage can
2136 not point out any electrical problem. After the reset of the registers, the
2137 total consumption should be around 33 mA. Then, the registers are loaded
2138 and the consumption should be around 750 mA. They are read-back by the
2139 JTAG software, which indicates if errors occur. If during the reading step
2140 no error was discovered, the sensors can be operated and their consumption
2141 should be around 1300 mA.

2142 An inspection of the output with an oscilloscope is performed to check
2143 the slow control and to estimate the response of the sensor. For the normal
2144 mode data format with SUZE enable, the output data of the last frame is
2145 sparsified and transmitted during the acquisition of the current one. The
2146 information provided by the MIMOSA-26 is contained in four output lines.
2147 The first output line corresponds to the *clock* which is always running even if
2148 the data transmission is finished. Its rate depends on the clock rate register.
2149 For the normal output mode, it is 80 MHz. The second output line is the
2150 *marker*, which is available in all mode. It is set during four clock's rising edge
2151 cycle and might be used to detect the beginning of the data transmission.
2152 Then, the two last output lines are dedicated to the data. They contain
2153 multiple information. First of all, the beginning and the ending of the data
2154 transmission is determined by the *header* and *trailer*. They can be used to
2155 detect a loss of synchronisation. They corresponds to 2×16 bits (*header0*-
2156 *header1* and *trailer0-trailer1*) and are totally configurable through the JTAG
2157 software. The *header* is followed by the *frame counter* which corresponds to
2158 the number of frames since the chip was reset. The information is separated
2159 into two words (*FrameCounter0* corresponding to the least significant bit
2160 and *FrameCounter1* corresponding to the most significant bit). Then, the
2161 *data length* gives the number of 16 bits words of the useful data. The useful
2162 data is split into *states/line*, which contains the address of the line which has
2163 a hit and an overflow flag if the number of states is bigger than the memory
2164 limitation. It is followed by the *state* giving the number of consecutive hits
2165 and the address of the first column. Finally, the *trailer* is ending the data
2166 transmission followed by 32 bits of zero. The figure 5.6 is a picture of an
2167 oscilloscope output of a MIMOSA-26 data output. From the top to the
2168 bottom, it shows the 80 MHz *clock*, the four clock's cycle *marker*, the *data0*
2169 and *data1* with the *header* and the *frame counter*. More information about
2170 the MIMOSA-26 can be found in the MIMOSA-26 user manual[28].

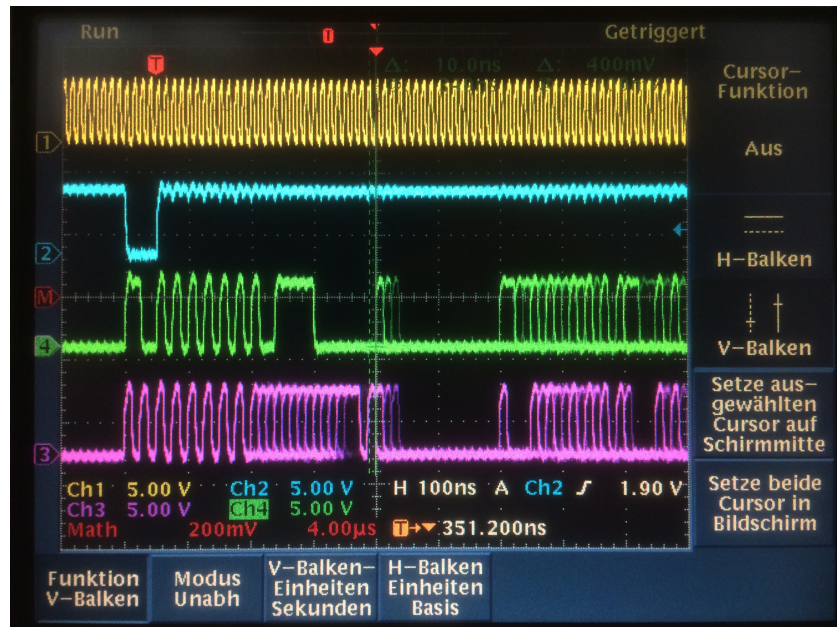


Figure 5.6 – MIMOSA-26 output from oscilloscope. The top yellow line corresponds to the clock, the blue line below to the marker (which last 4 clock cycles), and the green and purple line are the data output containing the hit information

2171 5.2.3 JTAG communication

2172 After adjusting the voltages and looking for any short-circuits, the next step
 2173 is to control the JTAG communication for every sensor. As in the PLUME
 2174 module, all the sensors are synchronised, only the *clock* and *marker* from
 2175 one sensor is read back. On the oscilloscope, the trigger is set on the *marker*.
 2176 The sensors are configured in the normal mode data format (80 MHz with
 2177 zero suppression output) and the output is checked in three steps. First of
 2178 all, the sensor is reset, the registers are loaded and read back and then the
 2179 start signal is sent. Through the JTAG software, the *header* and *trailer* are
 2180 modified several times and are checked thanks to the oscilloscope. Then,
 2181 the discriminators' response is visualised, specifically to find pixels always
 2182 sending data even if the discriminators are closed. The number of defective
 2183 pixels and their position is then estimated. After that, an estimation of
 2184 the threshold discriminator values to get few hits are determined and the
 2185 response is then checked. Nevertheless, using light to estimate the response
 2186 of the sensor can impact the pixels' baseline and modify the normal behavior

2187 of the matrix. For example, instead of sending more information, the pixels
2188 are less responsive. Thus, using a radiation source is a better solution.

2189 5.3 Noise measurements

2190 In chapter 4, the principle of the CMOS sensors is described and the noise
2191 of this technology is discussed. As a reminder, the two noise contributions
2192 are the Temporal Noise (TN) and the Fixed Pattern Noise (FPN). The FPN
2193 is determined as an offset to subtract from the pixel response to reduce its
2194 non-uniformity response, while the TN is coming from the contribution of
2195 different noises during the reset, the integration and the readout of the pixel.
2196 These noises have to be measured in the lab in order to find the optimum
2197 configuration to detect physics signal and reduce the noise impact on the
2198 measurement.

2199 5.3.1 Characterisation bench

2200 The noise is estimated with a bench of characterisation composed of a Na-
2201 tional Instrument PXIe crate equipped with a 6562 digital card, two power
2202 supplies, a power distribution board, an auxiliary and a JTAG card, as well
2203 as the module to test. The procedure described here is applied to a single
2204 MIMOSA-26, or a PLUME module, as well as an MIMOSA-28 sensor. Nev-
2205 ertheless, the data acquisition software used during the characterisation is
2206 slightly different to match the clock speed, depending on the sensor tech-
2207 nology. The four data outputs are connected from the pins on the auxil-
2208 iary board to the digital card thanks to a National Instrument spider cable.
2209 Firstly, a test pattern, which loads automatically a JTAG file for this test, is
2210 done to read the *header* and *trailer* during several frames with a determined
2211 data length. It has been observed that the *clock* output cable has to be 80 cm
2212 longer than the three other cables to ensure the synchronisation on the rising
2213 edge. If this is not done or if one of the cables has a wrong polarity, the
2214 software is not able to read the *header* and *trailer* and the characterisation
2215 can't be done.

2216 Then, the sensors are configured in the discriminator output mode. The
2217 zero suppression mode is bypassed, pixels and discriminators are in normal
2218 mode (the whole matrix read in $115 \mu\text{s}$), but the readout frequency is lower
2219 (10 MHz) via two LVDS output pads. The control of the discriminators is
2220 divided into four sub-matrices, each containing 288 columns. Thus, for one
2221 sub-matrix a threshold value in DAC units in the JTAG software is driving

2222 all the discriminators, depending on a baseline value. For one line, usually
 2223 one located in the middle of the matrix, its baseline response is studied to
 2224 find the "middle-points" by looking for the threshold of each sub-matrix, in
 2225 which the discriminators are reaching a half activation. When this "middle-
 2226 points" are determined, the homogeneity of the matrix is checked, as shown
 2227 on the figure 5.7. Due to the structure of the sensor, the homogeneity is
 2228 not perfect and some dispersions in the discriminator response are observed
 2229 between the beginning and the end of a sub-matrix. Moreover, to reduce
 2230 this dispersion, the reference baseline, and the clamping voltage have to be
 2231 adjusted.

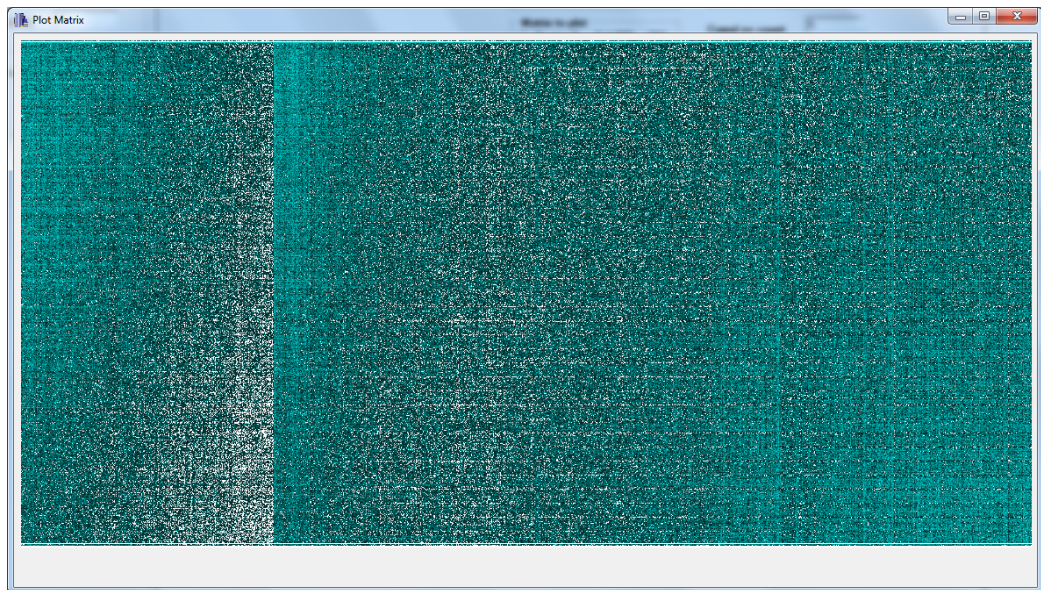


Figure 5.7 – Matrix response for the discriminators half activated.

2232 Afterward, the thresholds are set to the lowest and highest value to look
 2233 for defect pixels in the matrix. On the one hand, few pixels can be always
 2234 activated even if the discriminators were closed. The figure 5.8 depicts the
 2235 matrix output for all the discriminators closed. Therefore, a line is always
 2236 activated, as well as few pixels in a column and they are increasing the fake
 2237 hit rate of the matrix. A solution exists to disconnect some discriminators
 2238 in order to reduce the noise of defect columns thanks to the JTAG program,
 2239 nevertheless, no solution during the sensor programming exists to remove
 2240 the defect lines. On the other hand, few pixels can be always deactivated
 2241 even if the discriminators are completely opened, thus, they are not able to
 2242 detect any physics signal. This behavior is represented on the figure 5.9 and

2243 no solution exists to make them working properly.

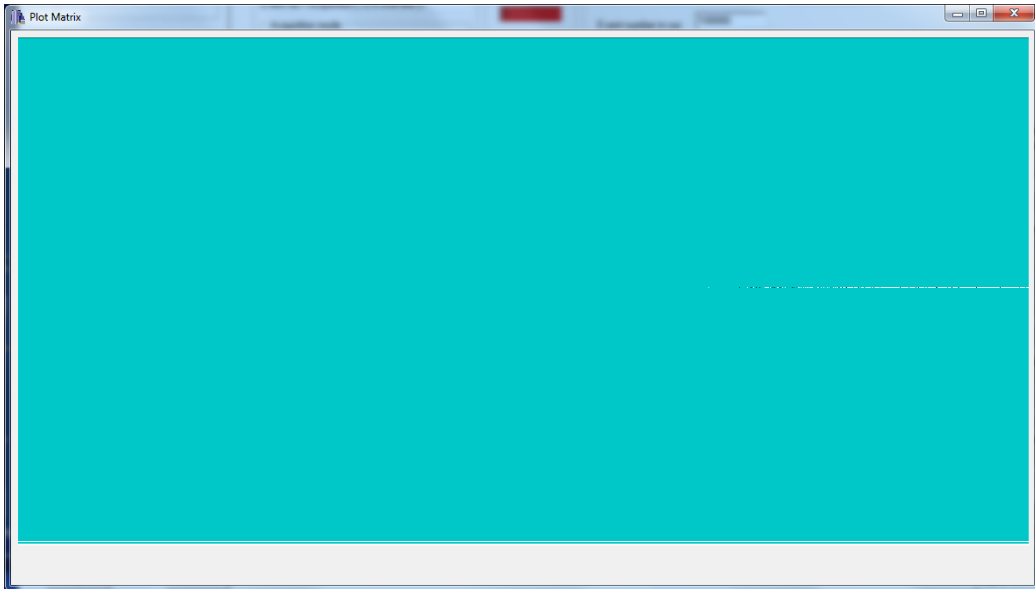


Figure 5.8 – Matrix response in discriminator mode, where all the discriminators are opened. On the right of the matrix, one line is not working correctly and some pixels are never activated

2244 5.3.2 Threshold scan

2245 The noise performance of the sensor is determined through a threshold scan
2246 around the "middle-point" found before. This consists to record the nor-
2247 malise response of the discriminators or the discriminators and the pixels for
2248 different threshold values. For the first possibility, an external voltage is in-
2249 jected into the discriminators, while the matrix output is disconnected. Only
2250 the noise contribution coming from the discriminator is thus determined. In
2251 this work, the noise performance results presented were done without injected
2252 an external voltage, but rather with the sensitive system connected to the
2253 discriminators. Usually, 29 runs containing between 50 to 1000 are stored.
2254 The files created are used to firstly, build a configuration file containing the
2255 DAC values of each sub-matrix for the different thresholds applied. The
2256 threshold is here defined has the voltage applied to the discriminators. Af-
2257 terward, this file is analysed and converted to create an output file containing
2258 a hit average picture of each sub-matrix for each step. Then, a macro based
2259 on C++ and ROOT framework is reading the hit average picture to plot the

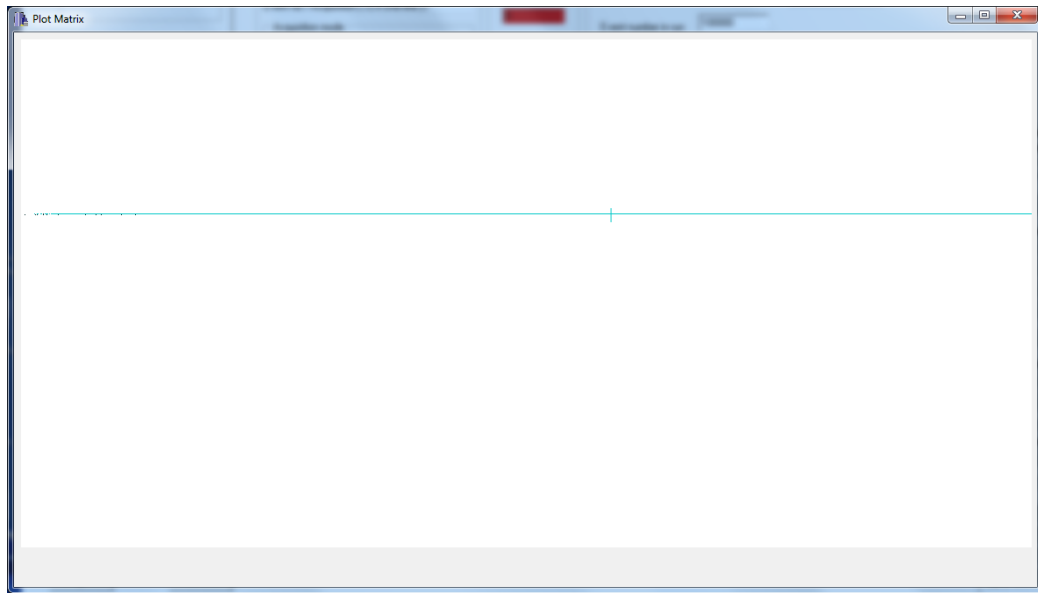


Figure 5.9 – Matrix response in discriminator mode, where all the discriminators are closed. One line of pixels is always activated, as well as few pixels in the same column. This will increase the fake hit rate of the sensor.

2260 transfer function, also called "S" curve, as represented on the figure 5.10. It
 2261 shows the normalised response of the 288 discriminators and the pixels con-
 2262 tained in this sub-matrix as a function of the threshold applied in millivolts.
 2263 The temporal noise of each pixel is calculated from the derivative of the "S"
 2264 curve and is represented here in the left plot of the figure 5.11. The mean
 2265 value of the distribution obtained the mid-point threshold of a pixel. The
 2266 dispersion of the mid-point threshold corresponds to the fixed pattern noise,
 2267 represented on the right plot of the figure 5.11.

2268 The plot on the left in figure ?? represents the temporal noise, while the
 2269 right one represents the fixed pattern noise. The systematic offset of the
 2270 discriminator is extracted from this measurements (the mean value of the
 2271 temporal noise, the mean value and the sigma value of the fixed pattern
 2272 noise). To calculate the discriminator thresholds of each sub-matrix for a
 2273 given SNR, the total noise is determined as:

$$\text{Total noise} = \sqrt{\langle TN \rangle^2 + \langle FPN \rangle^2} \quad (5.1)$$

2274 For a given S/N cut σ , the thresholds are determined by:

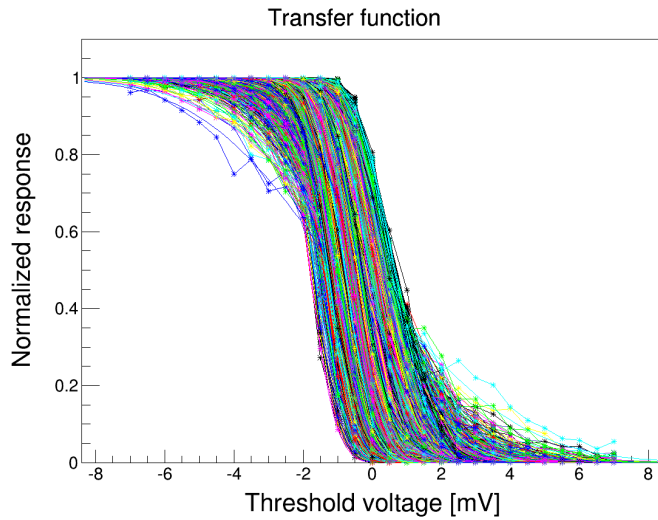


Figure 5.10 – Pixels response of a threshold scan around the middle-point of discriminators for a sub-matrix.

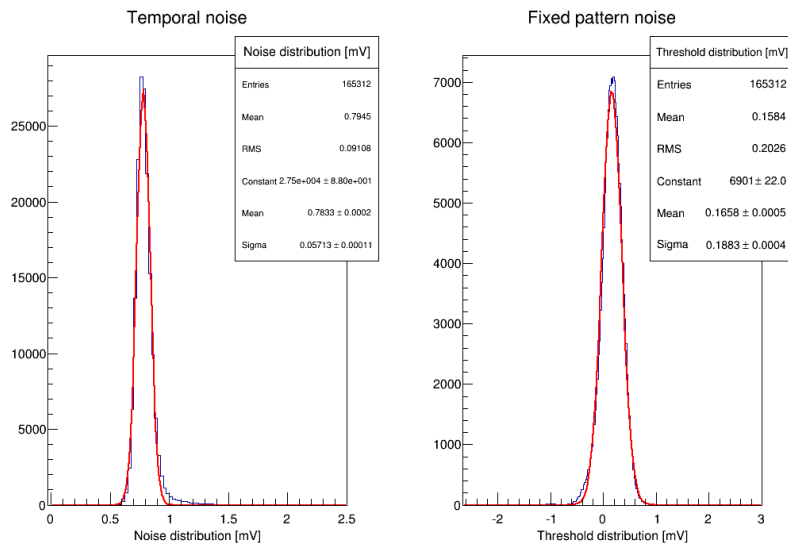


Figure 5.11 – Noise performances of a sub-matrix for the discriminators and the pixel array output. The temporal noise is plotted on the left plot, whereas the fixed pattern noise is represented on the right plot.

$$\text{Threshold (mV)} = \text{Total Noise} \times \sigma + \text{offset} \quad (5.2)$$

2275 This is converted into the DAC values by taking into account the DAC
 2276 offset and the DAC slope, which is assumed to be 0.25 mV:

$$\text{Threshold (DAC)} = \frac{\text{Threshold (mV)} - \text{DAC}_{\text{offset}}}{\text{DAC}_{\text{slope}}} \quad (5.3)$$

2277 5.3.3 Noise measurements

2278 Once the thresholds are defined for the different cuts, the fake hit rate of the
 2279 matrix, as well as the detection homogeneity is determined. A quick step
 2280 consists of using the DAQ software and acquiring ten-thousands events in
 2281 the dark to determine the noise qualitatively. The fake hit rate per event per
 2282 pixel is then considered as:

$$\text{F.H.R} = \frac{\text{Number of hits}}{\text{Number of events} \times \text{Number of pixels}} \quad (5.4)$$

2283 The figure 5.12 is representing the accumulation in the dark of ten thou-
 2284 sand events for a threshold five times bigger than the noise. The measured
 2285 fake hit rate was below 10^{-4} hits/pixel/events.

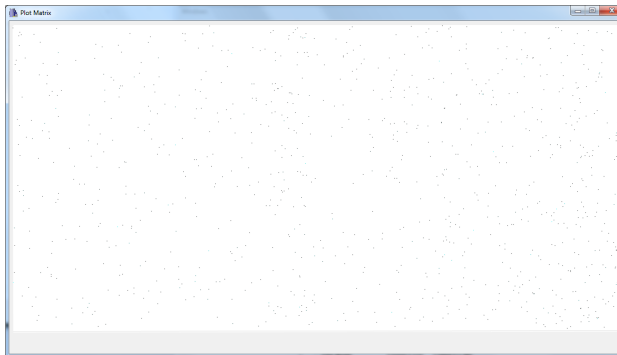


Figure 5.12 – Accumulation of 10k events at a thresholds of 5 times the noise acquired in the dark.

2286 Then, an iron 55 source is used to control the homogeneity of the thresh-
 2287 olds determined before. The figure 5.13 represents the accumulation of ten

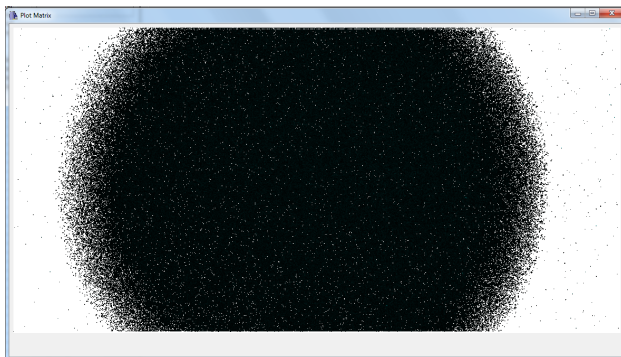


Figure 5.13 – Accumulation of 10k events at a thresholds of 5 times the noise with ^{55}Fe radiation source.

2288 thousand events for a threshold five time bigger than the noise with an iron
2289 source on top of the sensor.

2290 Finally, in order to validate the sensor, the acquisition system used during
2291 the test beam is used to calculate quantitatively the fake hit rate. The
2292 auxiliary board is connected to a Flex RIO board instead of the digital card.
2293 The test beam DAQ software developed by the IPHC is using a LabVIEW
2294 interface for the run control. It provides several useful information, such as
2295 the number of events acquired, the *header*, the *trailer* and the *frame counter*
2296 of the sensor. This helps the user to know if the acquisition is running
2297 properly. If the *frame counter* is different for each sensor, this points out
2298 a loss of synchronisation during the acquisition. Also, a different *header* or
2299 *trailer* such as the ones set in the JTAG software might point out a wrong
2300 connection. A second software is used to store the data into three files:
2301 a parameter file containing the run number, the event number, an index
2302 file and a binary file containing the raw data. Two acquisition modes are
2303 available. The first one, used in test beam, acquires data only when a trigger
2304 is sent. The second one, stores all frames regardless the trigger status. This
2305 acquisition is the one used in the lab, as only the noise of the sensor is
2306 measured.

2307 Several runs containing each one million events are acquired for different
2308 thresholds. The data stored are analysed with a software developed by the
2309 IPHC and is called TAPI Analysis Framework (TAF)[30]. It is based on
2310 C++ and the ROOT framework. The software reads the information of the
2311 hit pixels, reconstructs the clusters of hit pixels and in the case of a test
beam is able to reconstruct tracks from the hit information.

2313 A method is used to determine the fake hit rate with respect to the num-

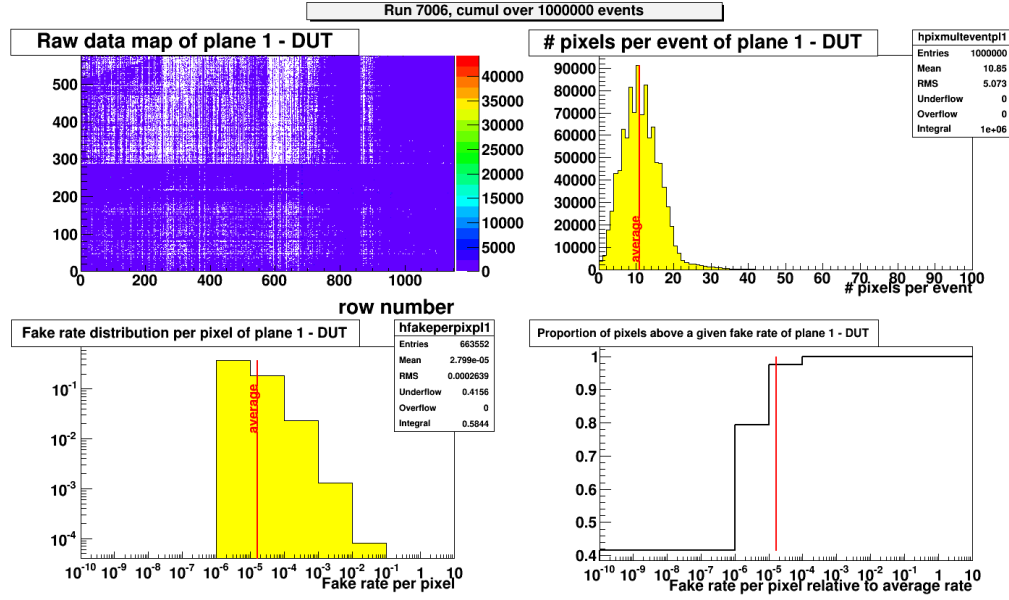


Figure 5.14 – Results of the fake hit rate measurement for a threshold three times bigger than the noise. The top left plot represents a raw picture of the million events accumulated over the whole matrix. The top right one is the distribution of the number of pixels hit per event. The bottom left plot is the fake hit rate per pixel distribution, while the bottom right one is the fake hit rate relative to the average rate distribution.

ber of pixels hit per event. From the distribution shown on the figure 5.14, which represents the number of pixels fired per event, the average fake hit rate is calculated as the mean of this distribution divided by the total number of pixels contained in the matrix. The error on the measurement is then the root mean squared of the distribution divided by the number of entries and the number of pixels inside the matrix. This calculation is done for different thresholds and the figure 5.15 represents the average fake hit rate per pixel per event as a function of the threshold for one sensor of an aluminum module. The results are matching the expected behavior for a standalone MIMOSA-26 sensor as shown in figure 4.10.

5.4 Conclusions

The assembly procedures and the tests performed in the laboratory were introduced along this chapter. Only the results for one sensor were presented.

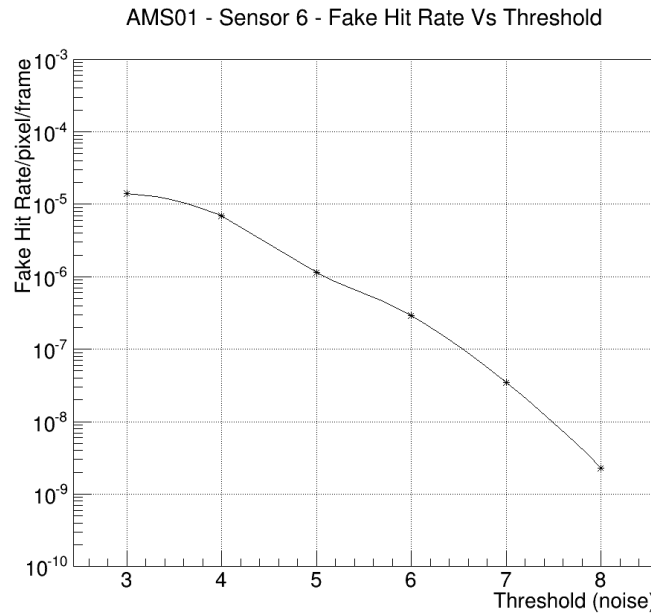


Figure 5.15 – Distribution of the fake hit rate per pixel.

Nonetheless, all the modules have a same behavior as the one expected for one single MIMOSA-26. So far, for the new PLUME versions which have a narrower flex-cable and which should embed only 0.35 % of the radiation length, different prototypes were built. The first ladder using copper module was assembled in January 2016. New ladders are currently being built and the collaboration is expecting to test them in the DESY test beam facility in November. Nevertheless, the aluminum ladder seems to be more challenging to build. Indeed, the three first mirrored versions produced have a connector problem, that could have been damaged by plugging and unplugging the jumper cable. This problem did not occur with the copper mirrored versions and this might come from a more fragile flex-cable. Ideally, each module should have its own jumper cable and this should not be disconnected. Nevertheless, for shipping them, there is no other solution. The collaboration is thinking of a tool which will reduce the stress applied to the connector.

The next chapter deals with the tests performed in real condition at the CERN-SPS facility with the PLUME-V1 prototype in 2011.

2343

Chapter 6

2344 **Deformation studies of a ladder
under the test beam**

2345

2346 The first full-scale prototype which embeds twelve sensors glued on a cop-
2347 per flex-cable and a 8 % density SiC foam was tested in November 2011 at
2348 CERN-SPS facility with a pions beam of 120 GeV. The motivations to per-
2349 form such a test in real conditions are first, to make sure that the ladder
2350 is working properly. Secondly, to verify the response homogeneity of each
2351 sensor. Finally, it has to prove the benefits of a double sided measurement.
2352 This chapter does not aim to present fully the test beam campaign and all
2353 the results but to focus on a specific study of the ladder's deformation ob-
2354 served during the alignment procedure. More results about this test beam
2355 are presented in Loic Cousin's thesis[36]. This chapter will present the test
2356 beam facility, as well as the experimental set-up. The alignment procedure is
2357 explained and some results for the ladder positioned in a normal incidence,
2358 as well as the ladder tilted in one direction, are discussed. The second part
2359 of the chapter will focus on the deviation observed during the alignment and
2360 will discuss a method to overcome these deformations. Finally, the benefits
2361 of double-sided measurements will be introduced.

2362

Contents

<small>2363</small> 6.1 Test beam of the full complete PLUME ladder	90
<small>2364</small> at CERN	90
<small>2365</small> 6.1.1 Test beam facility and beam test set-up	90
<small>2366</small> 6.1.2 Cartesian coordinate systems	90
<small>2367</small> 6.1.3 Measurements	91
<small>2368</small> 6.2 Spatial resolution studies	93
<small>2369</small>	

2370	6.2.1 Normal incidence track	93
2371	6.2.2 Ladder tilted in one direction	97
2372	6.3 Benefits of double-sided measurement	105
2373	6.3.1 Spatial resolution with mini-vectors	106
2374	6.3.2 Angular resolution	107
2375	6.4 Conclusions	109

2379 **6.1 Test beam of the full complete PLUME lad- 2380 der at CERN**

2381 **6.1.1 Test beam facility and beam test set-up**

2382 The test beam was performed at CERN-SPS in the North hall on the H6
 2383 beam line. Negative pions with an energy of 120 GeV were used. The spill
 2384 structure was 9.6 s with a dead time of 45.6 s. The bench set-up is composed
 2385 of a telescope equipped with four standard MIMOSA-26 sensors, thinned
 2386 down to 120 μm and used as reference planes. It is made of two arms and
 2387 the distance between two sensors of the same arm is 5 mm. The reference
 2388 planes are stabilised to a temperature of 15 degrees Celsius and a 8 sigma
 2389 S/N threshold cut was applied. The PLUME ladder is positioned between
 2390 the two telescope arms for the tests. For the rest of the chapter, the ladder
 2391 is called the Device Under Test (DUT). The bench has also 7×7 scintillators
 2392 used for triggering the data. Most of the runs were taken with a trigger
 2393 frequency between 2 and 8 kHz, except for two days where the frequency
 2394 was oscillating between 1 and 1.3 kHz. The acquisition system is limited to
 2395 eight inputs and four of them are used by the telescope. Thus, only four
 2396 sensors of the DUT were connected to the acquisition, two on each side. The
 2397 temperature of the DUT was stabilised thanks to an air flow cooling system,
 2398 provided by a fan.

2399 **6.1.2 Cartesian coordinate systems**

2400 Although the sensors have their own ID to distinguish them during the anal-
 2401 ysis, the position of each plane has to be known exactly. Two Cartesian
 2402 coordinate systems are then defined. The first one is the global one and is
 2403 determined by the position of each sensor of the telescope. The notation

6.1. TEST BEAM OF THE FULL COMPLETE PLUME LADDER AT CERN91

used for this coordinate system is (x, y, z) . The x -axis corresponds to the horizontal direction, the y -axis is the vertical one and the z -axis is along the beam direction. The origin $(0, 0, 0)$ of the system is usually defined by the position of the first plane hit. The second coordinate system is the local one and is determined by a single sensor. To differentiate this reference system to the other one, the (u, v, w) notation is used. The u -axis corresponds to the pixel rows, the v -axis is along the pixel columns and the w -axis is perpendicular to the matrix. The origin of the local system is the center of the pixel matrix. The figure 6.1 summarises the definition of the two coordinate systems.

Draw a better figure

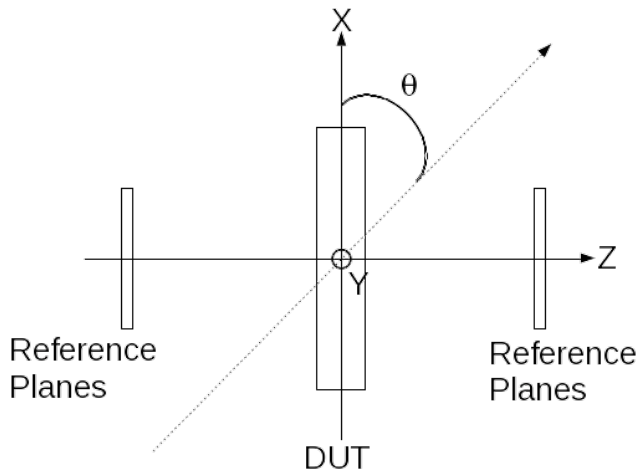
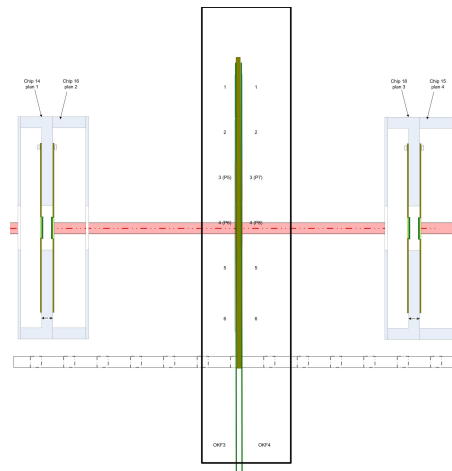


Figure 6.1 – Drawing of the laboratory coordinates.

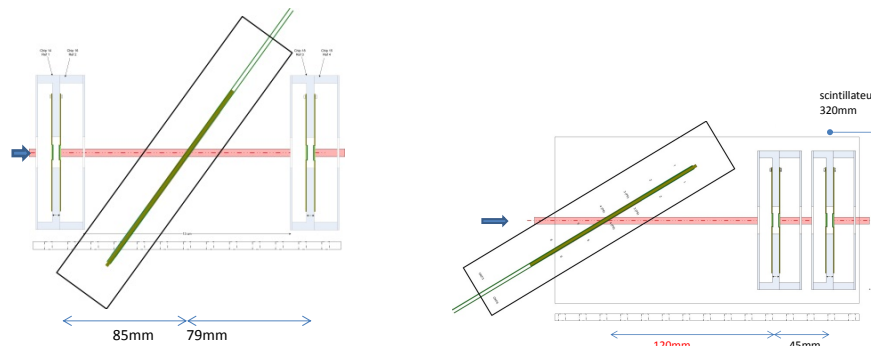
6.1.3 Measurements

The prototype validation was done under several conditions. Firstly, three different geometric configurations were used. On the first one presented on the figure 6.2a, the DUT is parallel to the telescope planes and the beam is hitting the device in a normal incidence. The ladder is placed in between the two arms. The middle of the foam is at equal distance from both inner telescope planes. For the second configuration, as shown on the figure 6.2b, the distance between the telescope planes are the same, but the DUT is tilted between 28 and 40 degrees along the y -axis. Runs with a larger angle (60 degrees) were done. Due to the PLUME box's size, the cabling for the

acquisition, the air cooling system and the design of the telescope stage, limiting the spacing between the two arms, the DUT was placed behind the two arms, as presented on the figure 6.2c. For both configurations, different parameters were modified. The thresholds were set to 5 and 6 mV, different sensors were aimed and the air flow speed was set to 3 m.s^{-1} and 6 m.s^{-1} .



(a) Configuration for normal incidence with respect to the beam direction.



(b) Configuration for an angle between 28 and 40 degrees.

(c) Configuration for an angle of 60 degrees.

Figure 6.2 – Top view sketches of the test beam configuration for different ladder positions: 6.2a is for normal incidence, 6.2b and 6.2c are for tilted ladder.

The analysis and the results shown in the following sections were performed with TAF, the analysis software developed by the IPHC and presented in chapter 5.

2432 6.2 Spatial resolution studies

2433 One of the measurements performed during the analysis is to determine the
2434 pointing resolution of the ladder. As the sensors used are well-known, the
2435 performance of the ladder should be similar to the one expected. Any devi-
2436 tions on the pointing resolution or the efficiency might point out an unex-
2437 pected impact of the mechanical structure or the flex-cable design over the
2438 whole system. The alignment steps to obtain the pointing resolution of
2439 the ladders are explained below for different run configurations.

2440 6.2.1 Normal incidence track

2441 For each event, the acquisition is recording the position of the pixels hit, the
2442 frame number, as well as the sensor ID. The binary file created contains no
2443 information about the relative position of each sensor. To perform an analy-
2444 sis, the telescope planes have to be aligned each other. The hits information
2445 of every plane is combined in order to create tracks. A track corresponds to
2446 the path of a particle through the system. Thanks to this information, the
2447 tracks are then compared to the hits position on the DUT to give some infor-
2448 mation, such as the detection efficiency (the ratio of tracks matched to the
2449 hits on the DUT) or the spatial resolution (minimum distance to distinguish
2450 two incoming tracks).

2451 The alignment procedure is done in two steps: firstly the telescope planes
2452 are aligned to minimise the mismatch of particles' tracks and to improve
2453 the tracking resolution. Afterward, the DUT is aligned with respect to the
2454 information provided by the reference planes and then, the analysis itself is
2455 performed. Although the position of each sensor is measured during the test
2456 beam with a precision of the millimeter, for the analysis, a precision of the
2457 micron level has to be achieved. Three degrees of freedom were taken into
2458 account for the alignment here: two translations for the x and y -axes and
2459 one rotation around the z -axis. The z position is determined by the position
2460 measured during the test beam campaign and is not considered as a free
2461 parameter due to the beam used.

2462 Alignment procedure and telescope alignment

2463 Firstly, the data acquired during the test beam are processed to extract the
2464 signal and the hit information. For each frame, the position of the pixel(s)
2465 having a signal above the discriminator threshold is stored and assigned
2466 to an ID corresponding to a sensor. The analysis software is in charge to

2467 assign correctly the hit to the sensors and then to group the pixel fired into
 2468 clusters. As the sensors used during the test beam have a binary output, no
 2469 information on the seed pixel is available. Thus, the hit position is obtained
 2470 from a centre-of-gravity calculation.

2471 Secondly, with the analysis software, one plane is considered as the origin
 2472 of the telescope coordinate system and is used as a reference for the align-
 2473 ment. Usually, the first sensor hit by the beam is the main reference. The
 2474 alignment means to correct the offset for the view angles and the hit position
 2475 of the telescope planes and the DUT. These offsets are found thanks to scat-
 2476 tering plots where the residuals are represented as a function of predicted hit
 2477 position. An alignment is considered as a good one when the residuals are
 2478 not correlated to the predicted hit position. If it is not centered around zero,
 2479 an offset has to be applied in this direction, whereas a slope indicates that a
 2480 tilt has to be applied. First off, the hit positions of the first plane are extrap-
 2481 olated to the next planes in order to perform the alignment. These tracks
 2482 extrapolated are straight lines perpendicular to the hits position. Thus, the
 2483 hit position of the last telescope plane is adjusted to match the hit position
 2484 of the first plane. The alignment is an iterative procedure which consists to
 2485 minimise the residual. It corresponds to the distance between the extrapo-
 2486 lated track to the closest hit on the sensor. Afterward, the track candidates
 2487 are built by matching a hit on the first plane to a hit on the last one. The
 2488 second and third telescope planes are aligned with respect to the information
 2489 provided by the extrapolated tracks. For example, the figure 6.3a and 6.3b
 2490 show the residual distributions of the second and third planes in the u and
 2491 v direction with respect to the tracks built by the first and the last planes.

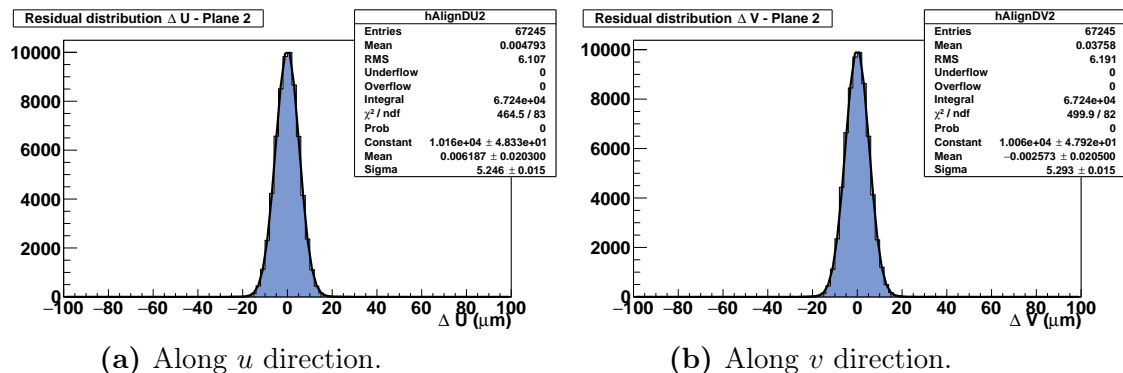
(a) Along u direction.(b) Along v direction.

Figure 6.3 – Residual distributions in the u and v directions for the middle telescope planes.

2492 As already explained, the alignment is an iterative procedure. At the

beginning, a region of interest of $1000 \times 1000 \mu\text{m}$ around the extrapolated is used to find a matching hit. Step by step, this region of interest is restricted to achieve a region of six times the pitch of the sensor.

After aligning the telescope, a candidate track is dismissed if it is made of less than four hits or if the χ^2 fit is greater than a fixed value determined by the user. Two assumptions are used during the alignment. The telescope planes are parallel each other. Thus the alignment consists of a translation along x and y and a rotation around the z -axis. As the test beam was performed without a magnetic field and pions of 120 GeV were used, the Coulomb multiple scattering is neglected. So, the tracks are perpendicular to the detectors and the alignment is not sensitive to the z position. A precision of the millimeter level for the position does not have a huge impact on the alignment.

Alignment of the DUT

When the telescope alignment is done, the reference tracks reconstructed by the reference planes are used to align the DUT. Its z position is fixed, nonetheless, two degrees of freedom are added to the three degrees defined above: the rotations along the x and y -axes. To assist the user in the alignment steps, several scatter plots are produced (see figure 6.4). For examples, the figures 6.4a and 6.4b help to indicate a tilt in the z -direction, whereas figures 6.4c and 6.4d help to find shift and/or tilt in the respective u and v -directions. The figures 6.4e and 6.4f show the residuals distribution in both direction for one sensor of the DUT. The width of these distributions, called spatial residual σ_{Res} , is approximately $4.1 \mu\text{m}$ and is a combination of the telescope resolution σ_{tel} , the multiple scattering $\sigma_{M.S}$ and the pointing resolution or spatial resolution of the sensor σ_{DUT} , as described in equation 6.1.

$$\sigma_{Res}^2 = \sigma_{tel}^2 + \sigma_{DUT}^2 + \sigma_{M.S}^2 \quad (6.1)$$

With 120 GeV pions, the effects of the Coulomb multiple scattering are neglected, thus the pointing resolution of the sensor is:

$$\sigma_{DUT} = \sqrt{\sigma_{Res}^2 - \sigma_{tel}^2} \quad (6.2)$$

For the configuration of the telescope used, the spatial resolution of the whole system measured is $\sigma_{tel} \simeq 1.8 \mu\text{m}$, thus the sensor studied here has a pointing resolution $\sigma_{DUT} \simeq 3.7 \mu\text{m}$ for a threshold of 6 mV. This result is

corroborating the pointing resolution of a single MIMOSA-26, as shown on figure 4.10 in chapter 4.

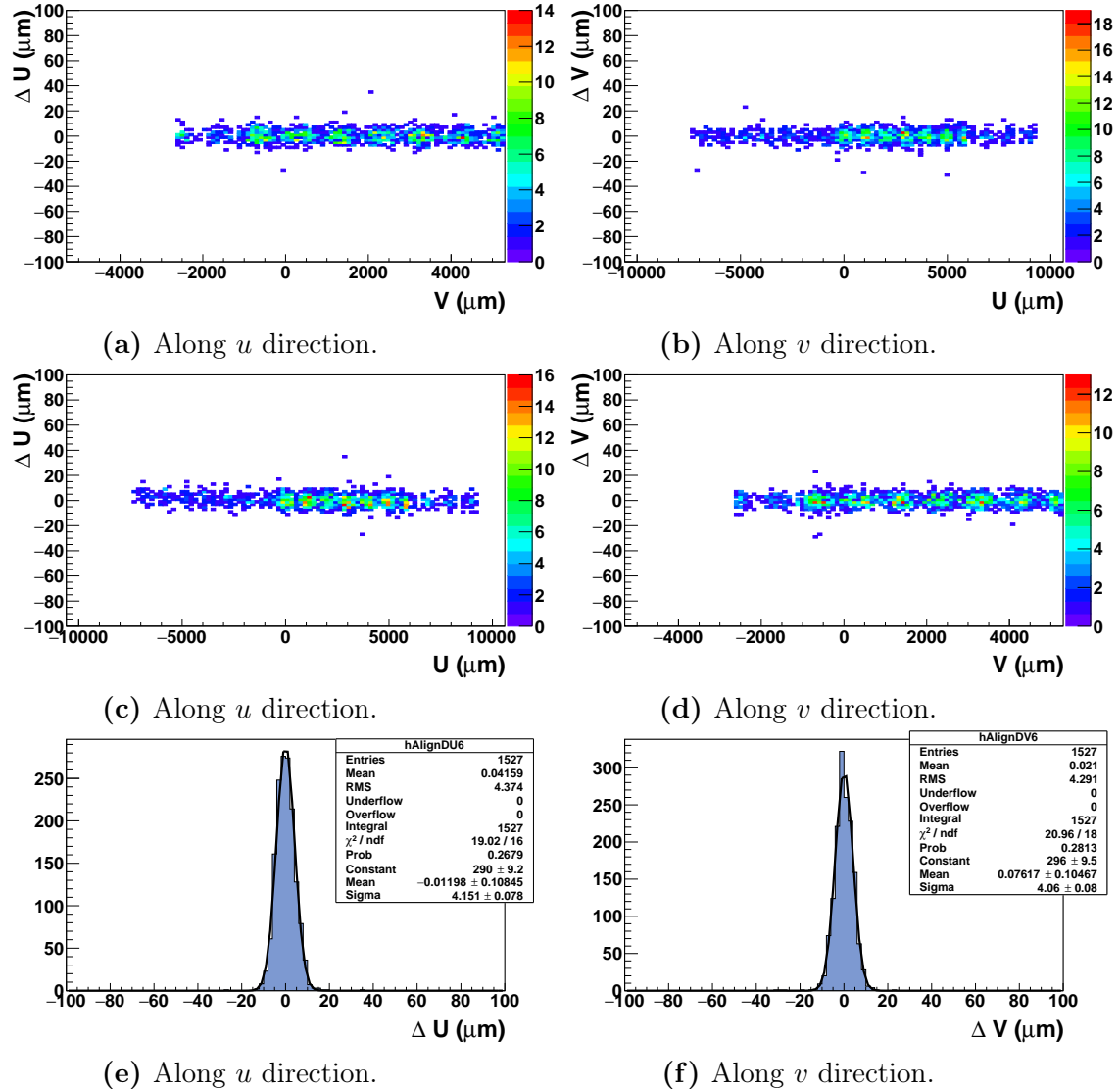


Figure 6.4 – Results of the DUT alignment: 6.4a is the residual ΔU as a function of the hit position on the v -direction, 6.4b is the residual ΔV as a function of the hit position on the u -direction, 6.4c is the residual ΔU as a function of the hit position on the same direction, 6.4d is the same plot for the other direction, 6.4e and 6.4f are the residuals distributions in the two directions.

2526 **6.2.2 Ladder tilted in one direction**

2527 The performances of the DUT are also studied for tilted tracks by rotating
2528 the ladder with respect to the beam axis along the v -direction. Three differ-
2529 ent angles were tested (28° , 36° and 60°), as well as different threshold cuts
2530 and air flow speed. The results presented below are for a run with a 36° tilt,
2531 a threshold sets to 5 mV and an air flow speed of 3 m.s^{-1} . The same align-
2532 ment procedure as presented in the subsection above is used, nevertheless,
2533 the alignment of the plane along the u -direction is more complicated than
2534 the other direction. Indeed, the scatter plot in the v -direction for the front
2535 plane which is shown on figure 6.5d represents a good alignment and the
2536 spatial residual (see figure 6.5f) is comparable to the one find for normal in-
2537 cidence tracks. But, the scatter plot $\Delta u = f(u_{hit})$ as presented on figure 6.5c
2538 shows a banana shape that can not be flatten with a traditional alignment
2539 procedure. Moreover, the spatial residual measured on figure 6.5e is larger
2540 ($6.8 \mu\text{m}$ instead of $\sim 4 \mu\text{m}$ in the v -direction) and the distribution has a
2541 large tail on the positive values. Concerning the back plane, the deformation
2542 is also visible on figure 6.6c but have a different form. The spatial residual
2543 measured for this plane is more than two times larger than the other side
2544 ($14.1 \mu\text{m}$) as it is depicted on figure 6.6e.

2545 **Origin of the deviations**

2546 The deviations observed are mainly caused by the characteristics of the lad-
2547 der. Indeed, ultra-thin sensors with a thickness of approximately $50 \mu\text{m}$ are
2548 used. Naturally, without any mechanical structure, the sensors tend to be
2549 very flexible and not self-supporting. Nevertheless, the gluing procedure to
2550 the flex-cable and the SiC foam induces permanent deformations of the sur-
2551 face that can not be flattened. Also, the foam has an open-cell structure
2552 with small bumps and the glue spots might be more or less important on
2553 some positions. The Bristol group has performed a mechanical survey on a
2554 mechanical prototype, which has non-functioning MIMOSA-20 sensors. The
2555 chips were thinned and attached to the standard flex-circuits. The measure-
2556 ments done with an optical survey equipment have revealed a peak-to-peak
2557 flatness of the order of the $100 \mu\text{m}$ on both sides. The figure 6.7 shows the
2558 result of this survey. The overall shape is due to the intrinsic shape of the
2559 foam.

2560 Another parameter has to be taken into account to explain the devia-
2561 tion observed. During the analysis, this non-flatness structure is not taken
2562 into account. The sensors are modelled as completely flat planes and the

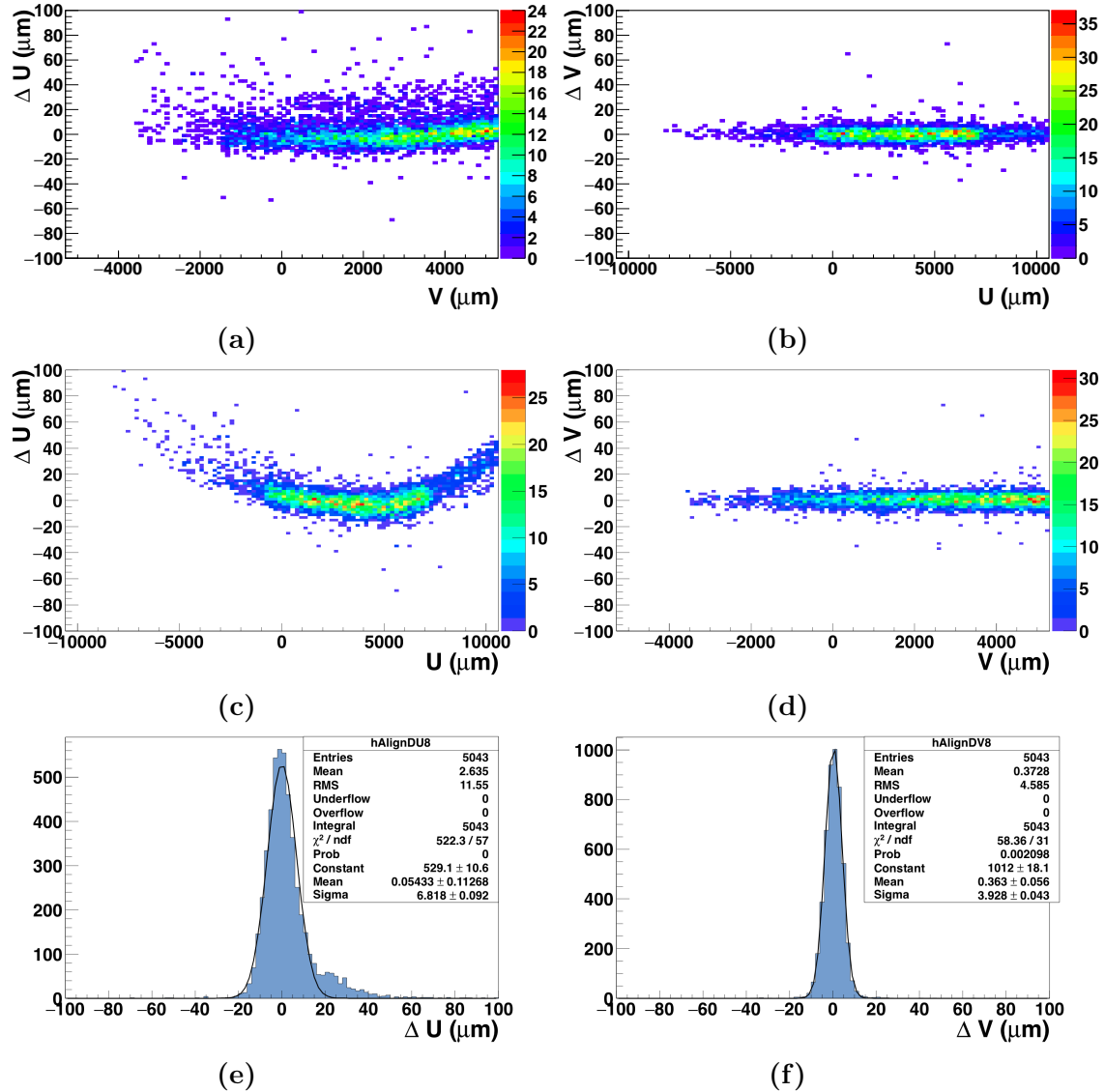


Figure 6.5 – Distribution of the residuals obtained for the front sensor with a tilt of 36° : 6.5a $\Delta u = f(v_{hit})$, 6.5b $\Delta v = f(u_{hit})$, 6.5c $\Delta u = f(u_{hit})$, 6.5d $\Delta v = f(v_{hit})$, 6.5e distribution of the residual Δu and 6.5f distribution of the residual Δv .

2563 z -position is fixed. However, the sensor's position in three dimensions is ac-
 2564 tually different due to the deformations. When the particles are not striking
 2565 the sensor in normal incidence, the hit predicted with respect to the flat

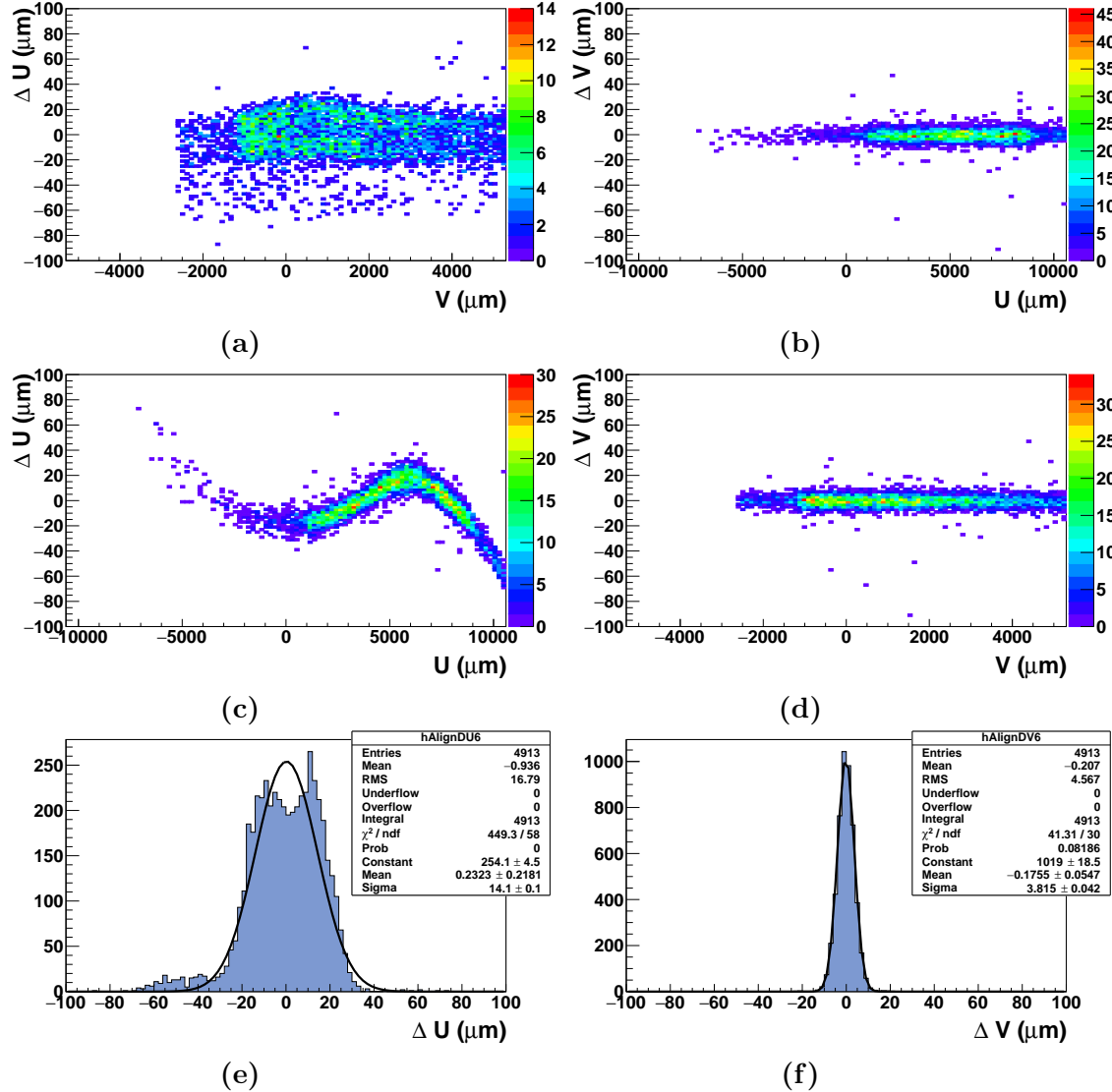


Figure 6.6 – Distribution of the residuals obtained for the back sensor with a tilt of 36°: 6.6a $\Delta u = f(v_{\text{hit}})$, 6.6b $\Delta v = f(u_{\text{hit}})$, 6.6c $\Delta u = f(u_{\text{hit}})$, 6.6d $\Delta v = f(v_{\text{hit}})$, 6.6e distribution of the residual Δu and 6.6f distribution of the residual Δv .

2566 plane does not have the same position anymore. Thus, the residual between
 2567 the position of the extrapolated track and the predicted hit is increasing.
 2568 The figure 6.8 depicts the difference between the hit expected U_h on the flat

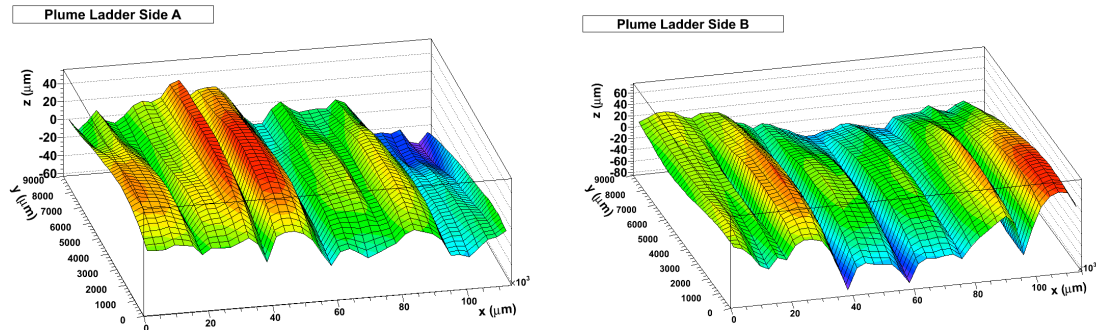


Figure 6.7 – Results of the mechanical survey of each side of the PLUME mechanical prototype.

2569 plane and the extrapolation of the actual hit U'_h extrapolated. For a normal
 2570 incidence, these two hits are at the same position, but larger is the angle,
 2571 larger is the difference between the expected hit and the extrapolated one.
 2572 The deformation height δw can be expressed as a function of the angle θ and
 2573 the residual δu of the track:

$$\delta w = \frac{\delta u}{\tan(\theta)} \quad (6.3)$$

2574 Thus, the visible deformation of the surface is sensitive to the angle of
 2575 the incoming track. In the case presented above, the angle of the incoming
 2576 track is only in one direction and so, the deformations are visible only in the
 2577 u -direction and the other one is not affected, even if the deformations are in
 2578 two dimensions.

2579 **Algorithm to estimate the deformations**

2580 The sensor deformations were already studied in Strasbourg by Maria Robert
 2581 Daniel. The sensor was mapped for the alignment in order to remove the
 2582 contribution of the deviation on the residual[42]. As this method is done man-
 2583 ually and is time-consuming, an automatic method has to be implemented.
 2584 A similar effect was observed in the CMS tracker during the alignment pro-
 2585 cedure with cosmic rays and a method was developed to compensate the
 2586 deformations[1]. They have used modified two-dimensions Legendre poly-
 2587 nomials to parametrise the sensors' deformations and therefore, they were

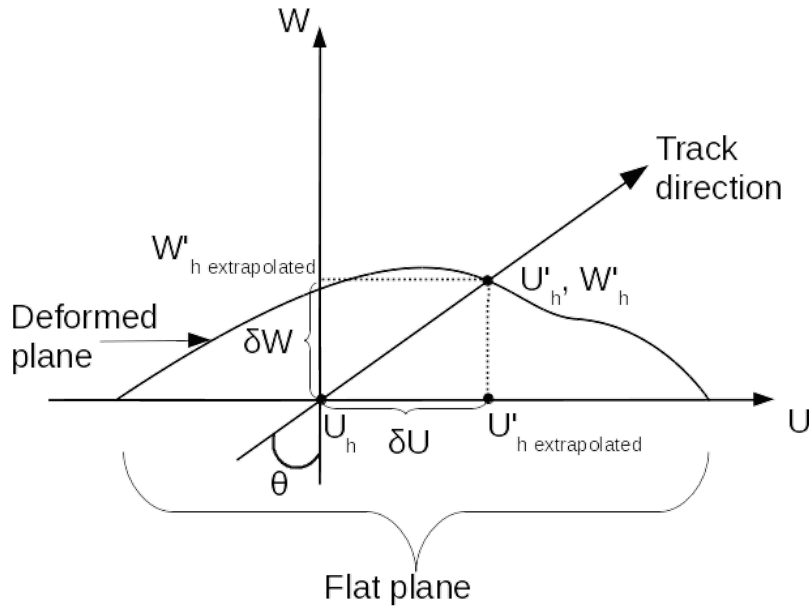


Figure 6.8 – Side view of the sensor’s deformation.

able to minimise the effect of the deviations during the alignment procedure of the tracker. The method implemented in TAF was inspired by the work which was done by the CMS collaboration. Nonetheless, contrary to the CMS tracker, the tilt was produced only in one direction. Hence, the two-dimensions Legendre polynomials can not be used to parametrise the sensor’s deformations, but the problem is still the same. Tracks with a large angle of incidence are more sensitive to the exact position of the plane in three dimensions, so the coordinates of the hits have to be exactly known. The deviations observed on the figure 6.5c provide an information on the behaviour of the deformation, that is extrapolated to the position of the plane on the w -direction. Thus, the hit position is calculated again with respect to the sensor’s surface shape extrapolated. This shape is guessed from the track-hit residuals as a function of the hit position in the same direction. A Legendre function is used to fit the curve and the coefficient given by the fit steps are used to calculate the deformation of the plane. The equation 6.4 represents the extrapolated shape of the plane in the w -direction calculated with respect to the expected hit position u_r , which is normalised to the sensor width.

$$w(u_r) = \sum_{k=0}^n \omega_k P_k(u_r) \quad (6.4)$$

2605 The ω_k are the coefficients that quantify the sensor curvature and $P_k(u_r)$
 2606 are the Legendre polynomials defined by the equation 6.5:

$$P_k(u_r) = \frac{1}{2^k!} \frac{d^k}{du_r^k} ((u_r^2 - 1)^k) \quad (6.5)$$

2607 Then, the exact hit position is calculated by correcting the hit position
 2608 extrapolated by $(-\omega(u_r) \cdot \tan \theta)$, according to the equation 6.3 and the resid-
 2609 ual Δu is determined by taking into account the tracks' angle during the
 2610 analysis.

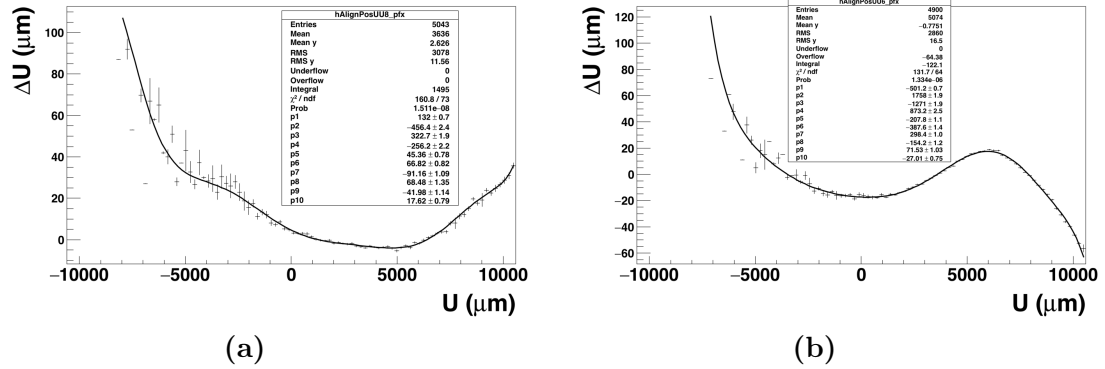


Figure 6.9 – Profile of the scatter plot showing the track-hit residual in the u -direction as a function of the hit position on the plane for the same direction: 6.9a is the profile of the front plane and 6.9b is the profile of the back plane. Both profiles were fitted with a sum of Legendre polynomials up to the eleventh order.

2611 Correction of the deformation

2612 Contrary to the CMS case, the Legendre polynomials used here are calculated
 2613 in one dimension as the tilt is only in one direction. The scatter plot displayed
 2614 in subsection 6.2.2 was profiled and fitted with a Legendre function. The sum
 2615 of Legendre polynomials up to different orders was tried to find the function
 2616 fitting the best the profile. The coefficients obtained after fitting are used
 2617 to parametrise the surface's shape and the position of the hit. The table 6.1
 2618 summarises the different χ^2 / NDF obtained for the different orders, as well
 2619 as the residual measured in the u -direction after correction.

2620 A second-order Legendre function does not fit well the profile of $\Delta U =$
 2621 $f(u_{hit})$ and does not provide a good improvement on the compensation of

Order	Front plane		Back plane	
	χ^2/NDF	σ_U^{front}	χ^2/NDF	σ_U^{back}
3	21683.9/84	6.508	35575.2/72	13.28
4	1449.91/83	6.176	25129.8/71	12.38
5	1449.79/82	5.998	1718.81/70	6.918
6	653.738/81	5.924	1480.55/69	6.817
7	304.206/80	5.922	634.696/68	6.406
8	288.376/79	5.937	269.296/67	6.228
9	225.376/78	5.9	250.565/66	6.239
10	225.353/77	5.914	152.236/65	6.159
11	158.053/76	5.913	131.727/64	6.176

Table 6.1 – Fit results of the scatter plot $\Delta U = f(U)$ for Legendre polynomials order and the residual obtained on each side of the PLUME ladder.

deformation. The best improvement was achieved on both sides from the 8th order Legendre polynomials to higher values. Although the χ^2/NDF is better for higher order, the width of the residual distribution is of the same order ($\sigma_{front} \simeq 5.9 \mu\text{m}$ and $\sigma_{back} \simeq 6.2 \mu\text{m}$). The figure 6.9a depicts the fit results for the front plane and the figure 6.9b is for the back plane. For both figures, the deviation is not well fitted for the negative values. The dispersion of the residuals is wider.

For example, using a 11th order Legendre polynomials has improved the spatial residual for both planes. Instead of $\sigma_u \simeq 6.8 \mu\text{m}$ for the front plane, the spatial residual is $\sigma_u \simeq 5.9 \mu\text{m}$, namely an improvement of 13.2 % of the measured spatial residual and achieving a pointing resolution of 5.6 μm for a tilt at 36°. Concerning the back plane, the spatial residual measured was 14.1 μm and after the correction it achieves 6.2 μm , namely an improvement of 56.0 % on the measured spatial residual. The point resolution of the plane is then 5.9 μm . As it can be seen on figure 6.10c, the deviations are reduced. Nevertheless, the edges of the plot are less corrected. This is due to the fact that the length of the sensor used to parametrise the Legendre function is a bit different to the real size of the sensor due to the deformation. On the back plane, a bump is still visible in the middle of the scatter plot (see figure 6.11c). This may be due to a missing information on the deformation of the sensor in the other direction.

This method was applied for different angles and the results are summarised in the table 6.2. The correction based on Legendre polynomials shows good results for the 28 degrees angle with a pointing resolution of 4.6 μm . Although for larger angles the precision is not expecting to reach the

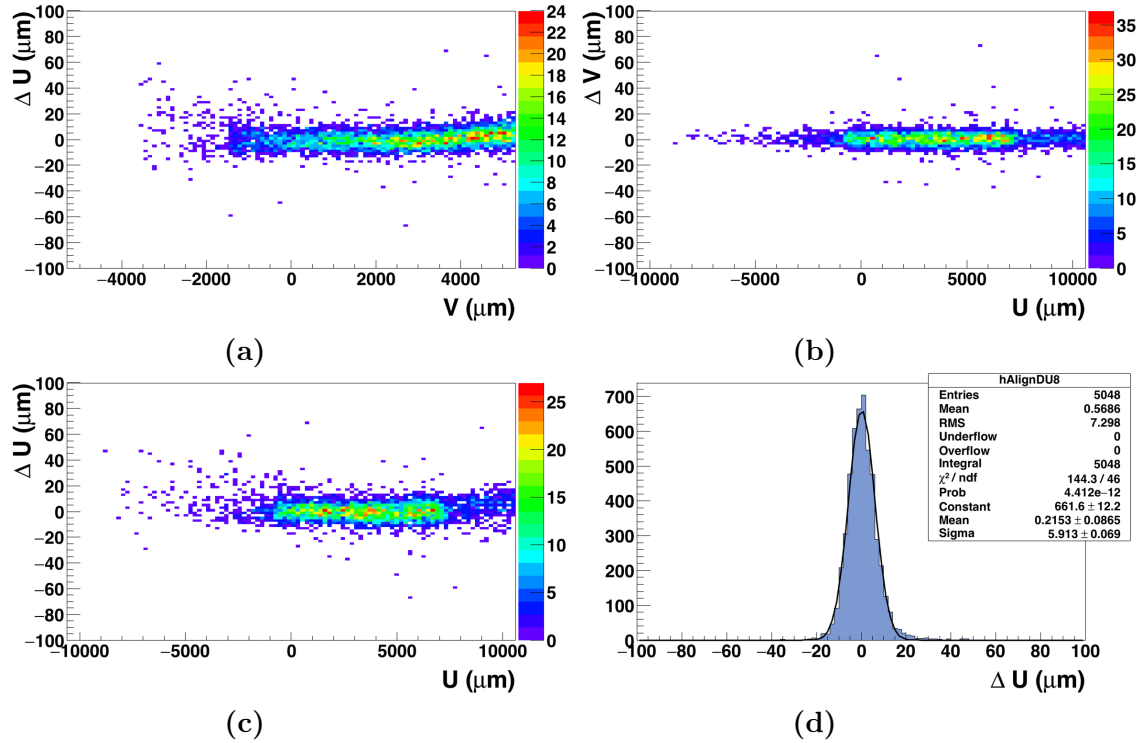


Figure 6.10 – Results of the alignment after applying the Legendre polynomials correction and taking into account the angle of the incoming particles for the front sensor: ?? $\Delta u = f(u_{hit})$ and [6.10d](#) distribution of the residuals.

normal value, the results obtained are less positive. For the large angle (60 degrees), the position of the DUT on the outside of the telescope arms does not provide a good telescope resolution ($\sigma_{tel} = 18.8 \mu\text{m}$). The pointing resolution achieved for the front and back planes are respectively $10.8 \mu\text{m}$ and $17.7 \mu\text{m}$. The sensitivity of the reconstruction to large tracks angle, as well as a unadapted telescope configuration impact severely the spatial resolution of the sensors.

A hypothesis on the deformation of the origin might come from heating or the cooling system that induces vibration. Although few runs were performed with a different air flow speed, the impact of the cooling system and the heat was not planned for this test beam. Thus, the results are not relevant enough to conclude for any vibration or the heat that tends to deform more the surface.

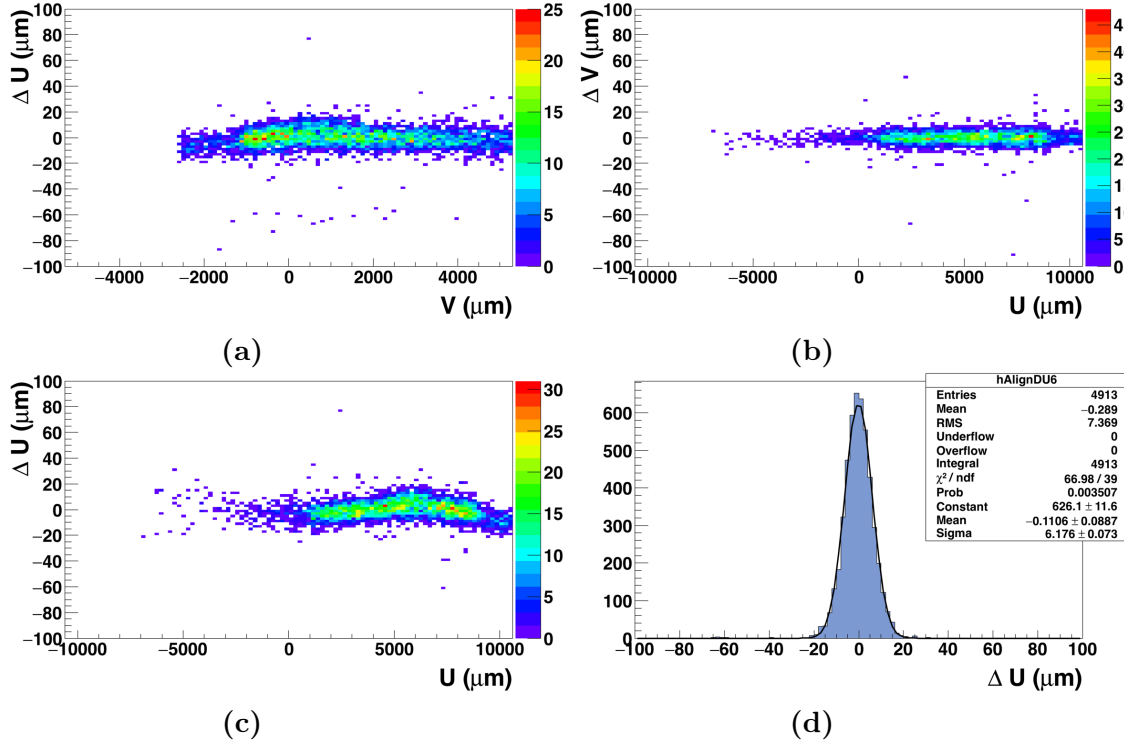


Figure 6.11 – Results of the alignment after applying the Legendre polynomials correction and taking into account the angle of the incoming particles for the back sensor: ?? $\Delta u = f(u_{hit})$ and [6.11d](#) distribution of the residuals.

Side	Tilted angle	σ_U^{Def} (μm)	σ_U^{Cor} (μm)	Improvement
Front	28	9.0 ± 0.1	4.9 ± 0.1	46.6 %
Back	28	5.7 ± 0.1	4.7 ± 0.1	17.5 %
Front	36	14.1 ± 0.1	6.1 ± 0.1	56.0 %
Back	36	6.8 ± 0.1	5.9 ± 0.1	13.2 %
Front	60	41.2 ± 0.15	25.8 ± 0.2	37.4 %
Back	60	23.3 ± 0.13	21.7 ± 0.1	6.8 %

Table 6.2 – Alignment results for different angles before and after using the correction based on Legendre polynomials.

2660 6.3 Benefits of double-sided measurement

2661 As two modules are sharing the same mechanical structure, the information
 2662 provided by each side can be combined together. A mini-vector is created

2663 by connecting two hits on each side of the ladder for the same event. This
 2664 combination gives access to a new information compared to a single sensor:
 2665 the angular resolution.

2666 **6.3.1 Spatial resolution with mini-vectors**

2667 To study the benefits of the mini-vector, a virtual intermediate plane is de-
 2668 fined at the center of the ladder. The two hits of each side of the DUT are
 2669 connected to form a mini-vector and the intersection of this vector to the
 2670 intermediate plane is determined. The intersection of the extrapolated track
 2671 to the intermediate plane is also performed and the distance between the
 2672 position of the track and the position of the mini is then measured.

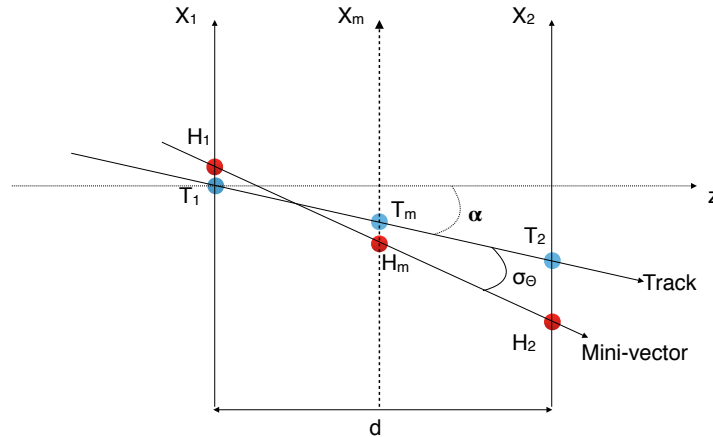


Figure 6.12 – Principle of the mini-vector. The two hits (in red) on the planes x_1 and x_2 are connected and the intersection on virtual intermediate plane x_m is then determined. The blue points represents the track extrapolated through the DUT.

2673 A theoretical estimation of the spatial resolution for the mini-vector can
 2674 be done thanks to the formula above:

$$\sigma_m^2 = \frac{\sigma_{front}^2 + \sigma_{back}^2}{(d_{front} - d_{back})^2} \cdot d_m^2 + \sigma_{tel}^2 \quad (6.6)$$

2675 Where σ_m is the resolution on the intermediate plane, σ_{front} and σ_{back} are
 2676 the resolution of the two sides of the DUT, σ_{tel} the resolution of the telescope
 2677 and $(d_{front} - d_{back})$ the distance between the front and back planes and d_m^2

2678 the position of the intermediate plane. For the plume ladder, the SiC as a
 2679 thickness of 2 mm and the intermediate plane is located in the middle, the
 2680 equation 6.6 can be rewritten:

$$\sigma_m^2 = \frac{\sigma_{front}^2 + \sigma_{back}^2}{4} + \sigma_{tel}^2 \quad (6.7)$$

2681 Thus, if the resolution on both side of the telescope are similar with
 2682 $\sigma_{front} = \sigma_{back} = \sigma$, the resolution of the mini-vector σ_{res} is then:

$$\sigma_{res} = \frac{\sigma}{\sqrt{2}} \quad (6.8)$$

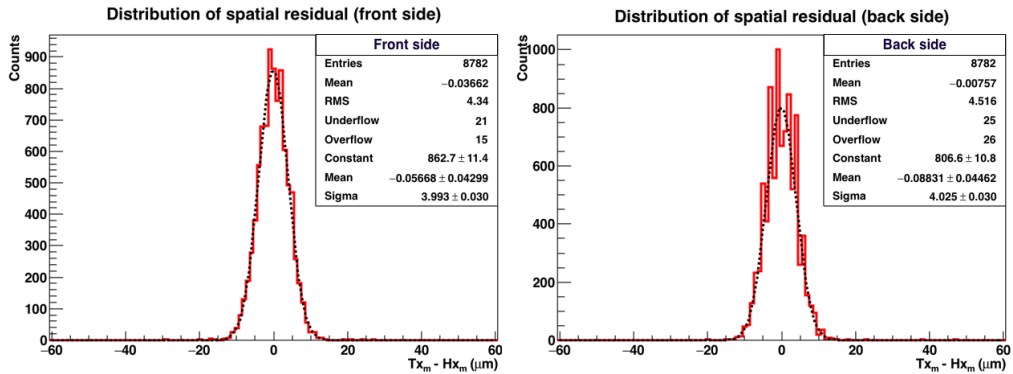


Figure 6.13 – Residual distribution for both side of the ladder in the u -direction

2683 For a run in normal incidence, the spatial resolution measured on each
 2684 side is $\sigma_{front} \simeq \sigma_{back} \simeq 4 \mu\text{m}$, according to the figure 6.13. The resolution
 2685 of the mini-vector should be then $\sigma_{res} \simeq 2.8 \mu\text{m}$. The measurement of the
 2686 residual for the mini-vector displayed on the figure 6.14 gives a residual of 3.2
 2687 μm . Taking into account the resolution of the telescope, the spatial resolution
 2688 achieved by the mini-vector is $\sigma_{res} \simeq 2.9 \mu\text{m}$.

2689 6.3.2 Angular resolution

2690 The mini-vectors give an access to new information not provided by a single
 2691 sensor, the angular resolution. The direction of the track can be compared
 2692 to the direction of the mini-vector. The estimation of the angular resolution
 2693 is given by:

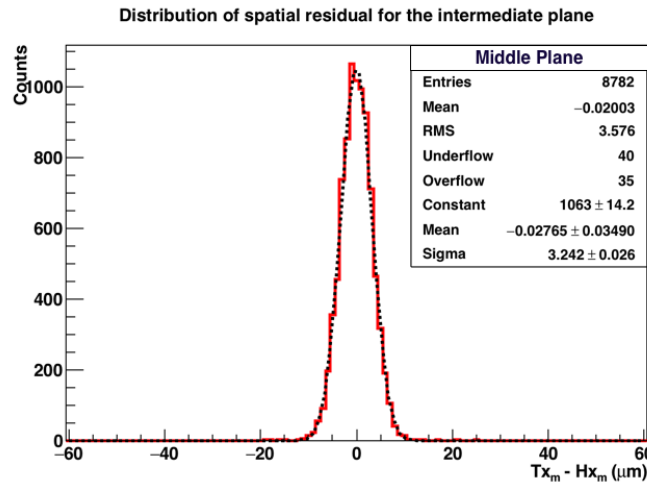


Figure 6.14 – Residual distribution of the mini-vector measured on the intermediate plane.

$$\sigma_{theta} = \frac{\sqrt{\sigma_{front}^2 + \sigma_{back}^2}}{d} \quad (6.9)$$

With σ_{front} and σ_{back} the spatial resolution on each side of the DUT in microns and d the distance between the two sides in microns. The spatial resolution here is $\sigma \simeq 3.6 \mu\text{m}$ and the distance between the two planes 2000 microns. The angular resolution estimated is then $\sigma_\theta = 0.146^\circ$.

The figure 6.15 depicts the distribution of the angle between the tracks direction and the mini-vectors direction. As it can be seen, several peaks are present and the distribution can't be extrapolated by a Gaussian fit. The sensors have a binary output and the hit position is determined by the centre-of-gravity of the clusters. If the cluster is only one pixel, the centre-of-gravity will be in the middle of the pixel, but if the clusters contain more pixels, this centre-of-gravity will be displaced. Moreover, they are some deviations in the distance between the hit projected to one side to the real hit position on this side. The figure 6.16 represents the minimum distance between one cluster on one side to the cluster on the other side.

Hence, for one pixel clusters, the displacement between the two pixels is the pitch $p = 18.4 \mu\text{m}$ and the angle between the two minimal hit position is then $\theta \sim 0.52^\circ$. A selection of the events where only clusters of 1 pixel are considered is shown on the figure 6.17a. The two peaks have a spacing

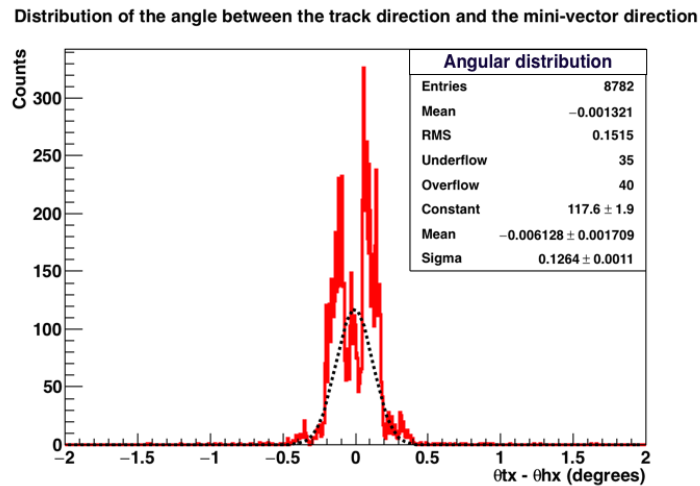


Figure 6.15 – Distribution of the angle between the tracks direction and the mini-vectors direction.

2712 close to 0.5° . For clusters of 1×2 or 2×2 pixels, the distance between the
 2713 two hit positions reconstructed via centre-of-gravity is half the pitch. Hence,
 2714 the peaks are two times closer with a spacing of nearly 0.25° , as seen on
 2715 the figures 6.17b and 6.17c. Nevertheless, for larger cluster sizes the angular
 2716 distribution has only one peak around 0° .

2717 6.4 Conclusions

2718 Along this chapter, the test beam campaign done in November 2011 at CERN
 2719 was discussed. The results were focused on the alignment procedure, as well
 2720 as the performances of the ladder in normal and tilted positions. The runs in
 2721 tilted position were challenging to align due to some deviations between the
 2722 track-hit residual and the actual hit position on the plane. This has the effect
 2723 of increasing the spatial residual measured. A higher pointing resolution
 2724 is expected for bending tracks but in a smaller proportion. An algorithm
 2725 using Legendre polynomials to describe the sensor's shape was discussed.
 2726 The results obtained for small angles are close to the value expected for a
 2727 single MIMOSA-26 sensor in normal incidence. Nevertheless, the pointing
 2728 resolution depends strongly on the incidence angle. For 36° and higher, the
 2729 correction is less efficient to achieve the normal performances. It might also
 2730 be possible that the heating is increasing the deformation and that the cooling
 2731 system could induce some vibrations which induce some deformation too.

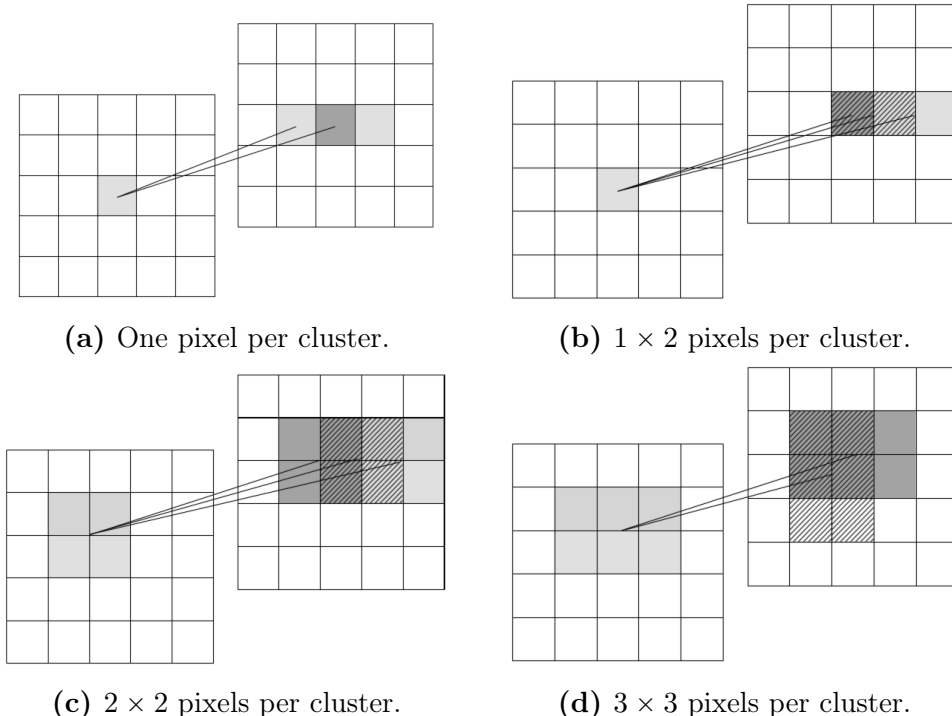


Figure 6.16 – Minimum distance between the cluster projected on one side to the position of the cluster of this side.

2732 Nevertheless, the results obtained here for different air flow speed can not
 2733 lead to a conclusion on a possible impact of the cooling system.

2734 The second part of this chapter was talking about the benefits of double-
 2735 sided measurements. For normal incidence, the pointing resolution of the
 2736 mini-vector, which is the combination of the pointing resolution on each
 2737 side, is better than the spatial resolution of a single sensor. Moreover, the
 2738 mini-vectors give access to another information: the angular resolution. Due
 2739 to the binary output and the centre-of-gravity hit position reconstruction,
 2740 multiple peaks are visible and a simple Gaussian fit can not be used. The
 2741 same work has to be done with ladder titled with respect to the beam to
 2742 study the impact of the deformation on the mini-vectors.

2743 The first results obtained are encouraging the mechanical structure. Nev-
 2744 ertheless, the material budget of the ladder is estimated theoretically. The
 2745 next chapter will introduce a test beam performed at DESY in 2016 and
 2746 will specifically talk about the measurement of the radiation length for a
 2747 PLUME-V1 prototype.

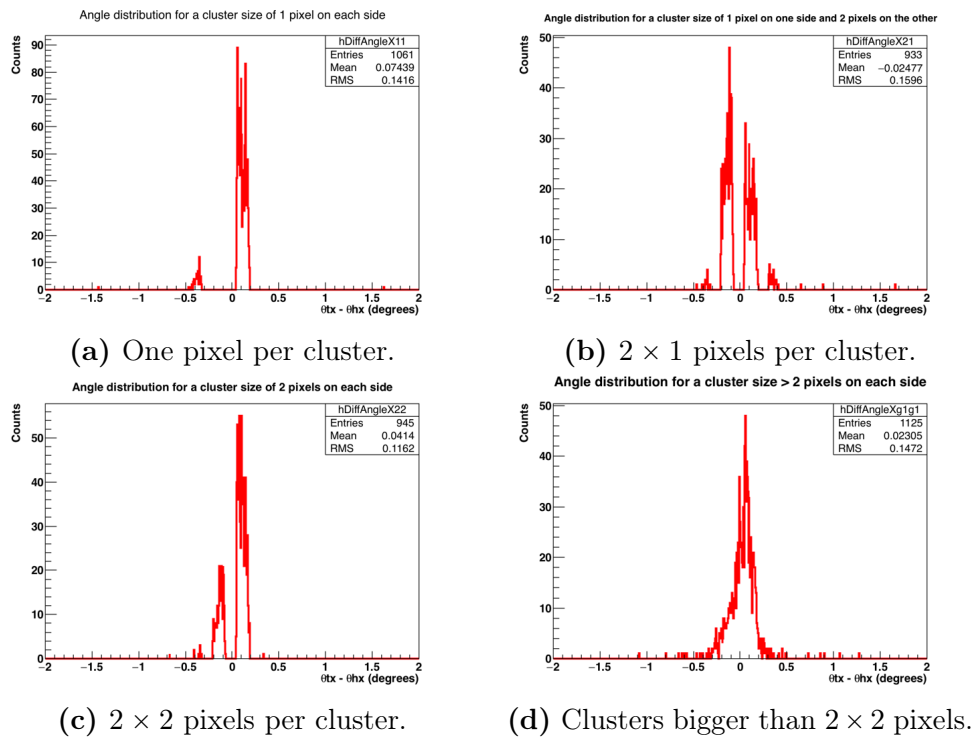


Figure 6.17 – Minimum distance between the cluster projected on one side to the position of the cluster of this side.

2748 **Chapter 7**

2749 **Determination of the material
2750 budget**

2751 The discovery of new physics and the characterisation of the already known
2752 particles are possible only with performant detectors. As it was presented
2753 on chapter 4, the fabrication of a vertex detector is constrained by two pa-
2754 rameters: the pointing resolution and the material budget. The first fully
2755 functional prototype of PLUME was tested in November 2011 at CERN with
2756 120 GeV pions. The results have shown that the pointing resolution of the
2757 ladder corresponds to the expected value for the ILD and moreover, the use
2758 of a double-sided structure improves this pointing resolution. Nevertheless,
2759 the material budget (X_0) of such device is estimated only by calculation and
2760 the SPS beam is not suited to a material budget measurement. Therefore,
2761 a test beam campaign of the PLUME-V1 prototype was done in April 2016
2762 at DESY test beam 21 with positrons up to 5 GeV. Firstly, the test beam
2763 preparation is discussed. Then, the motivation, the test beam facility, as well
2764 as the tools used for the analysis are presented. Finally, the results on the
2765 radiation length measurements are discussed.

2766 **Contents**

<small>2767</small> 7.1 Preparation of the test beam	114
<small>2768</small> 7.1.1 Measurements and telescope configuration	114
<small>2769</small> 7.1.2 Acquisition system	117
<small>2770</small> 7.1.3 experimental set-up	119
<small>2771</small> 7.1.4 Software analysis chain	120
<small>2772</small> 7.2 Measuring the radiation length	121

2774	7.2.1	Introduction	121
2775	7.2.2	Motivation	122
2776	7.2.3	The DESY II test beam facility	122
2777	7.3	Analysis	123

2781 7.1 Preparation of the test beam

2782 In April 2016, a test beam campaign with electrons and positrons up to 5 GeV
 2783 was performed at the DESY-II test beam facility. The first fully functional
 2784 PLUME ladder (PLUME-V1) was tested again to study the performances
 2785 of this device with low-momentum particles. The different measurements
 2786 scheduled are presented here, as well as the preparation of the test beam,
 2787 from the PLUME integration to the data acquisition.

2788 7.1.1 Measurements and telescope configuration

2789 During the two weeks of test beam, several measurements were performed to
 2790 test as much as possible the ladder. The measurements scheduled are:

- 2791 • Spatial resolution
- 2792 • Mini-vectors
- 2793 • Deformation study:
 - 2794 – Tilt up to 60° with a 10° step
 - 2795 – Air flow speed between 3 and 5 m.s⁻¹
- 2796 • radiation length along the sensors and on the mechanical flex

2797 Although all the planned schedule was performed, the test beam was at the
 2798 end of my Ph. D., therefore, I was not able to perform all of the measurements.
 2799 The section ?? presents the study I have performed on the radiation length
 2800 measurement.

2801 The pointing resolution of the telescope depends on the spacing between
 2802 the different planes. The best resolution is achieved by placing the inner
 2803 planes of the telescope as close as possible to the DUT and the outer planes
 2804 as far as possible from the DUT. Because of the deformation study, which

needs to rotate the ladder, the inner planes can not be close to the DUT without modifying the geometry at each steps. Hence, to keep a consistent alignment and to reduce the time spending on the off-line alignment, it was decided to fixed the inner planes as close as possible to be able to rotate the ladder without modifying the geometry. Moreover the ladder is not centered in its box, so to keep an equal distance between the two sides of the ladder and the two inner planes, the minimal distance between the telescope planes are calculated by taking into account an offset.

For the first time, the collaboration has decided to use the EUDET telescope and EUDAQ for the acquisition, instead of the Strasbourg telescope and the IPHC acquisition. Several configuration are available for the set-up used. The first ones consist to use the six planes of the EUDET telescope and to have two separate acquisition, one for PLUME and the second one dedicated for the telescope and then, to merge the data together. As the EUDET telescope are equipped with the same sensors as PLUME, the acquisition can be simplified by having only four telescope planes and connecting directly two sensors of the DUT. A simulation toolkit developed by Simon Spannagel and based on General Broken Lines (GBL) is used to compare the pointing resolution at the DUT position for different telescope geometries. Here, the six and four telescope planes set-up are compared for different energies and spacing between the sensors. This simulation takes into account the material budget of the telescope, the DUT and the multiple scattering of electrons in the air. One telescope plane as a material budget of ..., whereas PLUME is 0.65 % plus two kapton foils used to insulate the ladder from the light. For both configuration, the telescope is divided into two arms, two or three planes on each side of the DUT. The maximal distance between each plane of one frame is $d_{\max} = 150$ mm for the six sensors configuration, whereas for the second one it is $d_{\max}=300$ mm.

Energy (GeV)	σ_{res} (μm)	
	4 planes	6 planes
2	4.85	4.78
3	3.79	3.83
4	3.35	3.40
5	3.12	3.15
6	2.98	2.99

Table 7.1 – Estimation of the resolution measured σ_{res} at the DUT position for a telescope with four planes and six planes.

The table 7.1 summarises the measured resolution at the DUT position for different energies and the use of four or six telescope planes does not

2835 have an impact on the telescope pointing resolution. The figure 7.1 displays
 2836 the pointing resolution as a function of the different spacing between two
 2837 telescope planes of the same frame, for an energy set to 4.7 GeV.

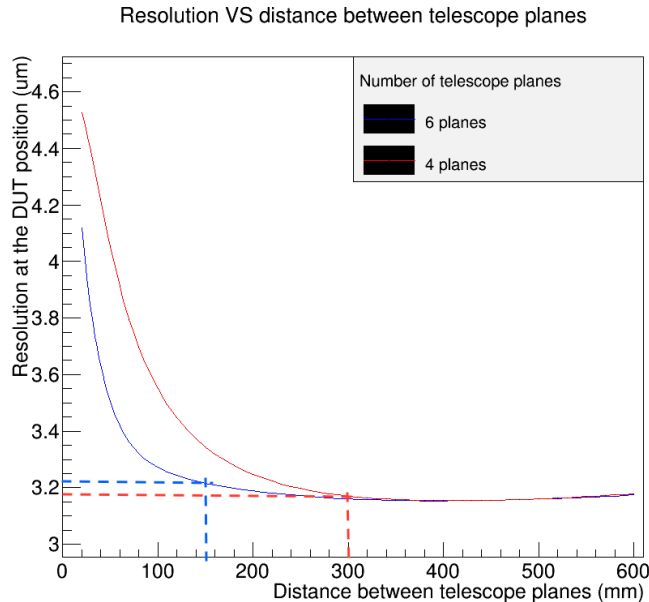


Figure 7.1 – Estimation of the resolution measured at the DUT position as a function of the distance between two telescope planes of the same arm. The blue lines is the results for six planes, whereas the red line is for four planes. The dashed lines are the maximal distance between two planes due to the rail limitation of the telescope frame.

2838 As the number of telescope planes does not impact the pointing resolution,
 2839 it has been decided to use only four telescope planes to simplify the
 2840 acquisition system. The sensors of the telescope and PLUME are both MI-
 2841 MOSA-26 thinned down to 50 μm . Instead of building a DAQ compatible
 2842 with EUDAQ, two EUDET telescope planes are removed from the set-up
 2843 and replaced by two PLUME sensors (one on each side). However, the syn-
 2844 chronisation and the stability of the acquisition have to be tested before the
 2845 test beam campaign.

7.1.2 Acquisition system**EUDAQ**

EUDAQ is a modular cross-platform data taking framework developed for the EUDET-type beam telescopes[29]. It is designed to be flexible and to have an easy integration of other devices. The software is based on *producers*, that are link between the different subdetector systems, such as the beam telescope, the DUT user DAQ and the Trigger Logic Unit (TLU). The events are built by the *Data Collector*. All subdetectors events are correlated to form one single global event for data belonging to one trigger.

To simplify the acquisition system, only one DAQ is used, but the robustness of the acquisition has to be tested. Hence, multiple tests are performed in the lab to make sure that EUDAQ is working with PLUME and then, single MIMOSA-26 sensors are added to the set-up.

Hardware

After ensuring that there is no data lose and the acquisition is stable for hours, the integration of PLUME on the test beam facility as been investigating. To perform the deformation studies, the DUT has to be on a rotation stage. With respect to the DUT coordinate system, the rotation is along the *u*-direction. Two options to perform the rotation are possible. The first one consists to have the same orientation between the PLUME sensors and the telescope planes. Hence, the ladder is in the horizontal position and the rotation needs a complicated frame... For the second options, ladder is positioned on the vertical direction. There is a 90° rotation between the telescope sensors and the PLUME ones. The frame consists of an aluminum plate insulated on which the DUT sits. Clamps are used to reduce the force applied by the cable on the flex to avoid to damage the DUT during the test beam. A plate with screws hold the ladder strongly to the frame. The frame is then mounted onto a rotation stage, which is mounted on a translation stage. The figure 7.2 shows a schematic model of the frame designed and built at DESY.

A cooling system is adapted to maintain a constant temperature. On one endcap, a pipe is fixed and connected to a fan. Some studies in Strasbourg were done to determine the air flow speed as a function of the voltage applied. Hence, an air flow speed of 3 m.s⁻¹ is achieved with 5 V and an air flow speed of 6 m.s⁻¹ for 10 V.

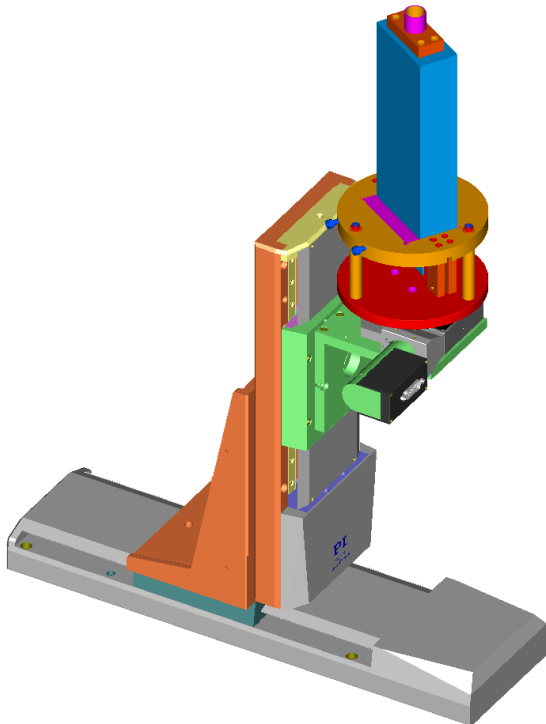


Figure 7.2 – TCAD model of the mechanical structure designed for the test beam in April. The ladder is hold on a circular frame fixed to a PI rotation stage, mounted onto a XY-table.

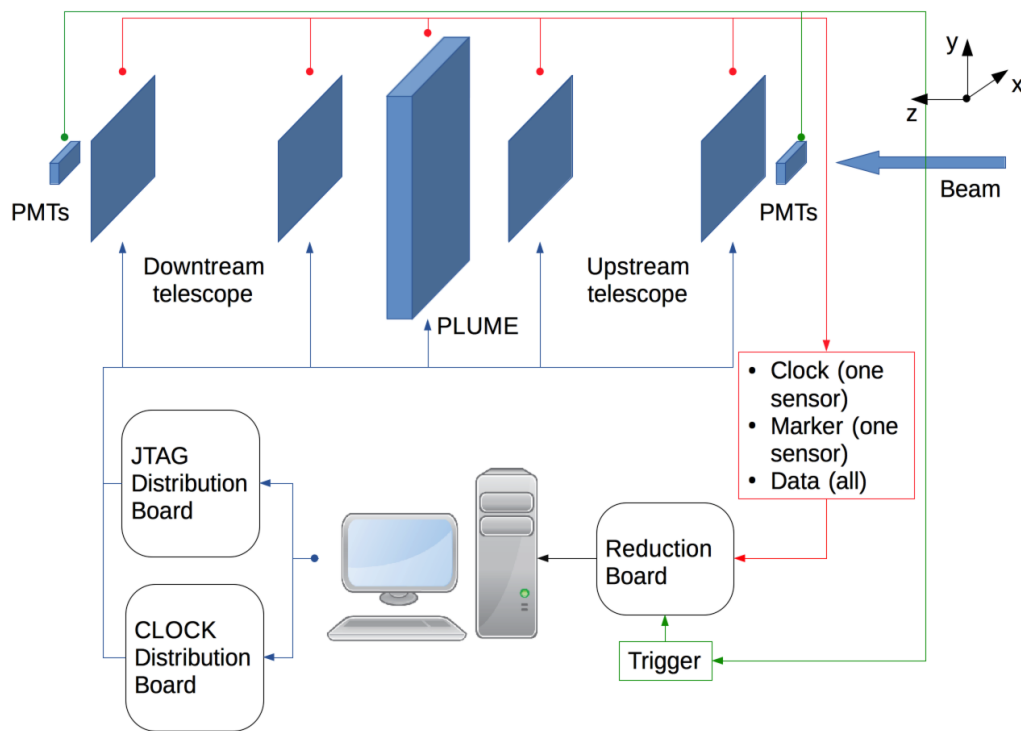


Figure 7.3 – Schematic of the test beam set-up. The PMTs are used for triggering. The clock and marker are read from only one sensor, here it comes from one PLUME sensor.

During the test beam campaign, the *clock* and *marker* are read from one sensor of the PLUME module. The *clock* is extended with a 80 cm long cable to ensure that one frame starts on the rising edge. The second input of the acquisition is a second PLUME sensor, followed by the four telescope planes. Photomultiplier Tube (PMT)s are placed in coincidence on each side of the telescope to avoid to trigger on fake events where the electrons does not pass through the entire set-up.

7.1.3 experimental set-up

To cool the ladder, a air cooling system is used. It consists of a fan connected to the back endcap of the PLUME box, via a pipe. A measurement performed by Strasbourg gives the corresponding air flow speed to the selected voltage input.

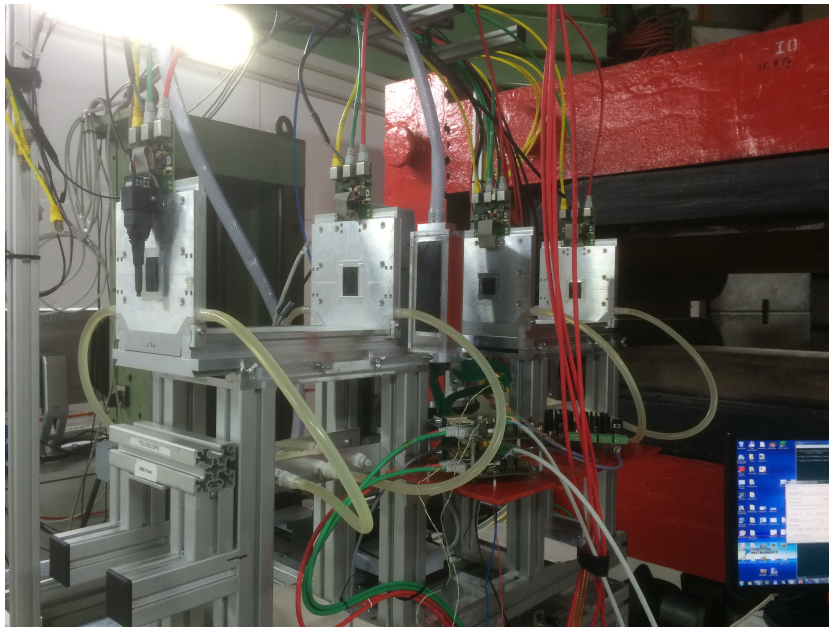


Figure 7.4 – Test beam set-up.....

2893 7.1.4 Software analysis chain

REF TO EU-
TEL

2894 The analysis framework used is called EUTelescope. It is based on the MAR-
2895 LIN framework from the ILCSOFT. It handles LCIO data format. Each step
2896 of the analysis is driven by dedicated processors.

2897 The first step consists to convert the raw data files into LCIO data format.
2898 This file contains the pixel number which fired in a given event, along with
2899 the sensor number. Then, the noisy pixel are removed before to use a cluster
2900 algorithm to form sets of cluster from the individual activated pixels. From
2901 the cluster information, the hit position is determined by a centre-of-gravity

2902 The specific acquisition which is done with EUDAQ has complicated the
2903 analysis. EUTelescope is coded to expect six telescope planes and a or several
2904 DUT but at different z -positions. One way to overcome this problem is
2905 to perform a biased analysis. Instead of performing the alignment of the
2906 telescope and followed by the DUT alignment, the procedure can be done in
2907 one way. Nevertheless, for an unknown reason GBL and Millepede-II are not
2908 working.

2909 A prototype software based on GBL and Millepede-II and written by
2910 Claus Kleinwort has permitted to perform the alignment, as well as the other

measurements. The software reads a lcio file containing the hit position of every plane.

Due to the specific acquisition which was done with EUDAQ, the analysis was a bit complicated. EUtelescope was coded to expect six telescope planes plus a single DUT. One way to overcome this problem was to perform a biased analysis. Instead of performing the alignment of the telescopes and then the DUT for an analysis, this step has to be done in one way. Nevertheless, the alignment procedure was not working.

To perform the alignment, I have used a python script written by Claus Kleinwort, which reads the hit position of every sensor and use GBL and MP-II to perform the alignment.

7.2 Measuring the radiation length

7.2.1 Introduction

Charged particles travelling through matter lose energy via inelastic collision with atomic electrons, but they also suffered from repeated elastic coulomb scattering from nuclei. Thus, they are deflected by many small angles from their initial trajectory because of the multiple coulomb scattering.

Highland formula describes the projected angle of the incoming particle depending on its momentum p , its velocity βc , its charge number z and its true path length in radiation length unit $\frac{x}{X_0}$.

$$\theta_0 = \frac{13.6 \text{ MeV}}{\beta cp} z \sqrt{\frac{x}{X_0}} \left(1 + 0.038 \ln \frac{x}{X_0} \right) \quad (7.1)$$

A modified version of the equation describes the electron scattering better than the Highland formula, with $\beta c = 1$ [23]:

$$\theta_0 = \frac{13.6 \text{ MeV}}{p} \left(\frac{x}{X_0} \right)^{0.555}, \quad (7.2)$$

The spread angle θ_0 depends on the momentum p of this particle and the relative radiation length $\frac{x}{X_0}$. Hence, higher is the momentum, lower is the spread angle. As well, the relative radiation length has an impact on the kink angle.

2937 7.2.2 Motivation

2938 The material budget of a detector is an important aspect during its design.
 2939 The ILC sets new goals for the material budget of the vertex detector, but
 2940 also for other parts of the detector. As a reminder, the tracking system
 2941 should detect precisely the particles path without degrading their energy,
 2942 while the calorimeters have to measure accurately the energy deposited by
 2943 the particles. To reconstruct accurately the events during a physics analysis,
 2944 the energy loss inside the different component of the detectors before the
 2945 calorimeters has to be known, in order to correct the measured energy.

2946 The radiation length X_0 is the amount of matter traversed by the electron
 2947 and its unit is g cm^2 . It is defined as the mean distance over which a charged
 2948 particle loss $1/e$ of its energy by bremsstrahlung.

$$\frac{1}{X_0} = \sum_j \frac{\omega_j}{X_j} \quad (7.3)$$

2949 7.2.3 The DESY II test beam facility

2950 The test beam facility at the Deutsches Elektronen-Synchrotron (DESY) is
 2951 made of three areas. Firstly, the electron beam is produced in the LINAC-II
 2952 and accelerated to 450 MeV before to be injected in the DESY-II synchrotron
 2953 ring. The DESY-II is used as a storage ring for the PETRA-III. The beam is
 2954 accelerated and the particles are stored until enough particles are available
 2955 to be sent on to PETRA, where they are used for photon science.

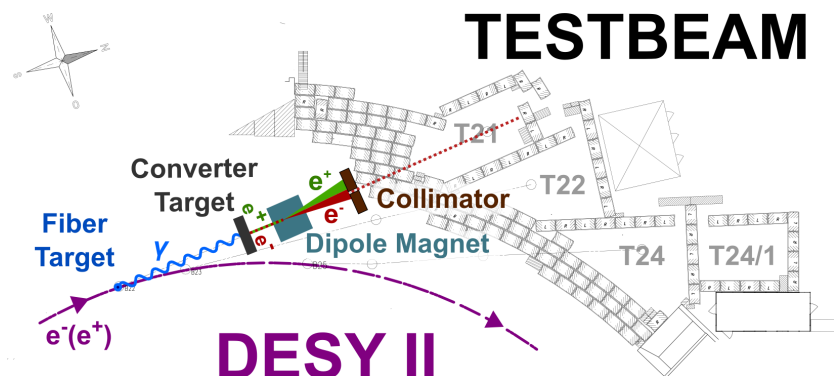


Figure 7.5 – Schematic layout of the DESY-II test beam facility[16].

To generate the beam delivered in the Hall 26, a graphite fiber target is placed inside the beam pipe. While the electrons are hitting the target, they lose energy and emit bremsstrahlung photons. The photons travel through the air and hit a target, on which the photons are converted to pairs of electrons and positrons. Different targets with different thicknesses are available and this will impact the particles rate. One is made of copper, whereas the other one is made of aluminum. Then, a dipole magnet bends the particles and spread them according to their energy. Afterward, a tungsten collimator cuts away the unwanted particles, those having a too high or too low momentum, before the test beam area. A second collimator is located in the test beam area and it determines the size of the beam spot. The figure 7.5 summarises the different step to generate a beam of electrons or positrons in test beam 21, while the energies and the rates available are displayed in figure 7.6

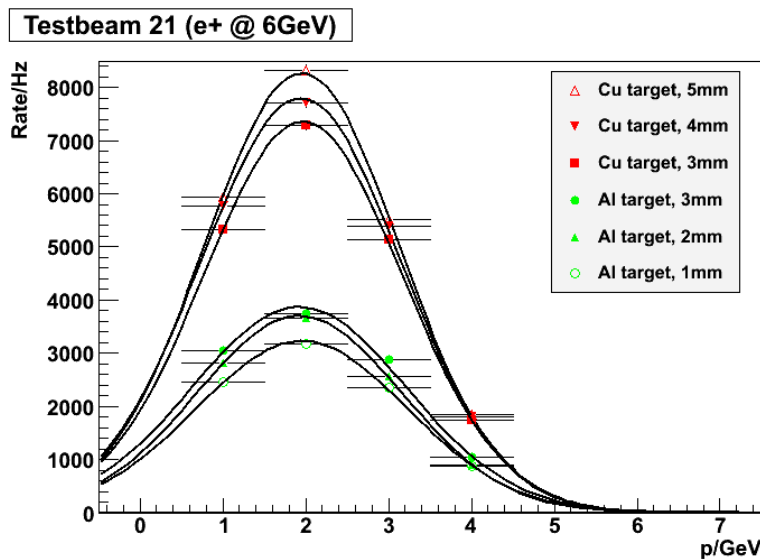


Figure 7.6 – Rate for different momentum and with different converter targets[16].

2970 7.3 Analysis

²⁹⁷¹ Acronyms

- ²⁹⁷² **AHCAL** Analogue HCAL. [36](#)
- ²⁹⁷³ **APS** Active Pixel Sensor. [53](#)
- ²⁹⁷⁴ **ASIC** Application-Specified Integrated Circuit. [53](#)
- ²⁹⁷⁵ **BDS** Beam Delivery System. [25](#)
- ²⁹⁷⁶ **CCD** Charged Coupled-Device. [52](#)
- ²⁹⁷⁷ **CDS** Correlated Double Sampling. [66](#)
- ²⁹⁷⁸ **CLIC** Compact LInear Collider. [24](#)
- ²⁹⁷⁹ **CMOS** Complementary Metal Oxide Semi-conductor. [49](#)
- ²⁹⁸⁰ **DAQ** Data AcQuisition. [54](#)
- ²⁹⁸¹ **DC** Direct-current. [25](#)
- ²⁹⁸² **DEPFET** Depleted P- Channel Field Effect Transistor. [53](#)
- ²⁹⁸³ **DESY** Deutsches Elektronen-Synchrotron. [122](#)
- ²⁹⁸⁴ **DUT** Device Under Test. [90](#)
- ²⁹⁸⁵ **ECAL** Electromagnetic CALorimeter. [33](#)
- ²⁹⁸⁶ **EM** electromagnetic interaction. [1](#)
- ²⁹⁸⁷ **ETD** End-cap Tracking Detector. [33](#)
- ²⁹⁸⁸ **FPCCD** Fine Pixels Charged Coupled-Device. [52](#)

- ₂₉₈₉ **FPN** Fixed Pattern Noise. [65](#)
- ₂₉₉₀ **FTD** Forward Tracking Detector. [33](#)
- ₂₉₉₁ **GBL** General Broken Lines. [115](#)
- ₂₉₉₂ **GEAR** GEometry Api for Reconstruction. [46](#)
- ₂₉₉₃ **GRPC** Glass Resistive Plate Chamber. [36](#)
- ₂₉₉₄ **HCAL** HAdronic CALanalogue HCALorimeter. [35](#)
- ₂₉₉₅ **ILC** International Linear Collider. [24](#)
- ₂₉₉₆ **ILD** International Large Detector. [21](#)
- ₂₉₉₇ **IP** interaction point. [28](#)
- ₂₉₉₈ **IR** interaction region. [25](#)
- ₂₉₉₉ **ISR** Initial State Radiation. [46](#)
- ₃₀₀₀ **JTAG** Joint Test Action Group. [74](#)
- ₃₀₀₁ **LCIO** Linear Collider I/O. [46](#)
- ₃₀₀₂ **LHC** Large Hadron Collider. [19](#)
- ₃₀₀₃ **LHCAL** Low angle Hadron CALorimeter. [36](#)
- ₃₀₀₄ **MAPS** Monolithic Active Pixel Sensor. [35](#)
- ₃₀₀₅ **Marlin** Modular Analysis and Reconstruction for the LINear collider. [46](#)
- ₃₀₀₆ **MIMOSA** Minimum Ionizing MOS Active pixel sensor. [53](#)
- ₃₀₀₇ **MIP** Minimum Ionizing Particle. [60](#)
- ₃₀₀₈ **OKF** Optiprint-Kapton-Flex-cable. [56](#)
- ₃₀₀₉ **PFA** Particle Flow Algorithm. [30](#)
- ₃₀₁₀ **PLUME** Pixelated Ladder with Ultra-low Material Embedding. [49](#)

- 3011 **PMT** Photomultiplier Tube. [119](#)
- 3012 **QCD** Quantum Chromodynamics. [8](#)
- 3013 **QED** Quantum Electrodynamic. [5](#)
- 3014 **QFT** Quantum Field Theory. [5](#)
- 3015 **RTML** Ring To the Main Linac. [26](#)
- 3016 **SDHCAL** Semi-Digital HCAL. [36](#)
- 3017 **SET** Silicon External Tracking. [33](#)
- 3018 **SiC** Silicon Carbide. [55](#)
- 3019 **SiD** Silicon Detector. [30](#)
- 3020 **SIT** Silicon Internal Tracker. [33](#)
- 3021 **SM** Standard Model. [2](#)
- 3022 **SNR** Signal to Noise ratio. [66](#)
- 3023 **SRF** Superconducting Radio-Frequency. [24](#)
- 3024 **SUZE** Suppression de zéro. [65](#)
- 3025 **TAF** TAPI Analysis Framework. [85](#)
- 3026 **TLU** Trigger Logic Unit. [117](#)
- 3027 **TN** Temporal Noise. [65](#)
- 3028 **TPC** Time-Projection-Chamber. [30](#)
- 3029 **VXD** Vertex Detector. [31](#)
- 3030 **ZIF** Zero Insertion Force. [55](#)

3031

Bibliography

- 3032 [1] Alignment of the CMS tracker with LHC and cosmic ray data. pages
3033 1748–221, 1088.
- 3034 [2] DEPFET Pixels as a Vertex Detector for the Belle II Experiment. 2013.
- 3035 [3] Georges Aad et al. Observation of a new particle in the search for the
3036 Standard Model Higgs boson with the ATLAS detector at the LHC.
3037 *Phys. Lett.*, B716:1–29, 2012.
- 3038 [4] R. Appleby, L. Keller, T. Markiewicz, A. Seryi, R. Sugahara, and
3039 D. Walz. The International Linear Collider Technica. 3, 2006.
- 3040 [5] D. M. Asner, T. Barklow, C. Calancha, K. Fujii, N. Graf, H. E.
3041 Haber, A. Ishikawa, S. Kanemura, S. Kawada, M. Kurata, A. Miyamoto,
3042 H. Neal, H. Ono, C. Potter, J. Strube, T. Suehara, T. Tanabe, J. Tian,
3043 K. Tsumura, S. Watanuki, G. Weiglein, K. Yagyu, and H. Yokoya. ILC
3044 Higgs White Paper. page 152, oct 2013.
- 3045 [6] H Baer, T Barklow, K Fujii, Y Gao, and a Hoang. [1306.6352] The Interna-
3046 tional Linear Collider Technical Design Report - Volume 2: Physics.
3047 ... *preprint arXiv:13066352*, 2, jun 2013.
- 3048 [7] M. Battaglia. Vertex tracking at a future linear collider. *Nucl. Instru-*
3049 *ments Methods Phys. Res. Sect. A Accel. Spectrometers, Detect. Assoc.*
3050 *Equip.*, 650(1):55–58, sep 2011.
- 3051 [8] Jerome Baudot, Olena Bashinska, Nathalie Chon-Sen, Wojciech Dulin-
3052 ski, Franziska Hegner, Marie Gelin-Galibel, Rhorry Gauld, Mathieu
3053 Goffe, Joel Goldstein, Ingrid Gregor, Christine Hu-Guo, Ulrich Koetz,
3054 Andrei Nomerotski, and Marc Winter. Development of Single- and
3055 Double-sided Ladders for the ILD Vertex Detectors. mar 2012.

- 3056 [9] T. Behnke, J. E. Brau, B. Foster, J. Fuster, M. Harrison, J. P. Paterson,
 3057 M. Peskin, M. Stanitzki, N. Walker, and H. Yamamoto. ILC Technical
 3058 Design Report Volume 1: Executive Summary. *ILC Tech. Des. Rep.*
 3059 *Vol. 1 Exec. Summ.*, 1:1–60, 2013.
- 3060 [10] Ties Behnke. The international linear collider. *Fortschritte der Phys.*,
 3061 58(7-9):622–627, 2010.
- 3062 [11] Constantino Calancha Paredes, A Dubey, H Ikeda, A Ishikawa, S Ito,
 3063 E Kato, A Miyamoto, T Mori, H Sato, T Suehara, Y Sugimoto, and
 3064 H Yamamoto. Progress in the development of the vertex detector with
 3065 fine pixel CCD at the ILC.
- 3066 [12] Serguei Chatrchyan et al. Observation of a new boson at a mass of 125
 3067 GeV with the CMS experiment at the LHC. *Phys. Lett.*, B716:30–61,
 3068 2012.
- 3069 [13] Donut Collaboration, K Kodama, N Ushida, C Andreopoulos, N Saoulidou,
 3070 G Tzanakos, P Yager, B Baller, W Freeman, B Lundberg, J Morrn,
 3071 R Rameika, J C Yun, J S Song, C S Yoon, S H Chung, P Berghaus,
 3072 M Kubanstev, N W Reay, R Sidwell, N Stanton, S Yoshida, S Aoki,
 3073 T Hara, and J T Rhee. Observation of Tau Neutrino Interactions. 2000.
- 3074 [14] A. Denner, S. Heinemeyer, I. Puljak, D. Rebuzzi, and M. Spira. Standard
 3075 Model Higgs-Boson Branching Ratios with Uncertainties. *Eur. Phys. J.*,
 3076 C71:1753, 2011.
- 3077 [15] Deutsches Elektronen-synchrotron Desy and Hamburg Germany. A re-
 3078 view of e+ e- Linear Colliders. 22:529–539, 1988.
- 3079 [16] Test beam at desy. [http://particle-physics.desy.de/test_beams_](http://particle-physics.desy.de/test_beams_at_desy/index_ger.html)
 3080 [at_desy/index_ger.html](http://particle-physics.desy.de/test_beams_at_desy/index_ger.html).
- 3081 [17] M Deveaux, S Amar-Youcef, A Besson, G Claus, C Colledani,
 3082 M Dorokhov, C Dritsa, W Dulinski, I Fröhlich, M Goffe, D Grand-
 3083 jean, S Heini, A Himmi, C Hu, K Jaaskelainen, C Müntz, A Shabetai,
 3084 J Stroth, M Szelezniak, I Valin, and M Winter. Radiation Tolerance of
 3085 CMOS Monolithic Active Pixel Sensors with Self-Biased Pixels. 2009.
- 3086 [18] F. Englert and R. Brout. Broken Symmetry and the Mass of Gauge
 3087 Vector Mesons. *Physical Review Letters*, 13:321–323, August 1964.
- 3088 [19] ~a R Erwin, R H March, W D Walker, M Goldhaber, T D Lee, C N
 3089 Yang, G Danby, J-M Gaillard, K Goulian, L M Lederman, N Mistry,

- 3090 M Schwartz, and Z Steinbergert. OBSERVATION OF HIGH-ENERGY
3091 NEUTRINO REACTIONS AND THE EXISTENCE OF TWO KINDS
3092 OF NEUTRINOS. *Phys. Rev. Phys. Rev. Phys. Rev. Lett.*, 9(6):101–
3093 1640, 1961.
- 3094 [20] E. Fermi. An attempt of a theory of beta radiation. 1. *Z. Phys.*, 88:161–
3095 177, 1934.
- 3096 [21] R. P. Feynman and M. Gell-Mann. Theory of the fermi interaction.
3097 *Phys. Rev.*, 109:193–198, Jan 1958.
- 3098 [22] Y. Fukuda, T. Hayakawa, E. Ichihara, K. Inoue, K. Ishihara, H. Ishino,
3099 Y. Itow, T. Kajita, J. Kameda, S. Kasuga, K. Kobayashi, Y. Kobayashi,
3100 Y. Koshio, M. Miura, M. Nakahata, S. Nakayama, A. Okada, K. Oku-
3101 mura, N. Sakurai, M. Shiozawa, Y. Suzuki, Y. Takeuchi, Y. Totsuka,
3102 S. Yamada, M. Earl, A. Habig, E. Kearns, M. D. Messier, K. Scholberg,
3103 J. L. Stone, L. R. Sulak, C. W. Walter, M. Goldhaber, T. Barszcza-
3104 k, D. Casper, W. Gajewski, P. G. Halverson, J. Hsu, W. R. Kropp,
3105 L. R. Price, F. Reines, M. Smy, H. W. Sobel, M. R. Vagins, K. S.
3106 Ganezer, W. E. Keig, R. W. Ellsworth, S. Tasaka, J. W. Flanagan,
3107 A. Kibayashi, J. G. Learned, S. Matsuno, V. J. Stenger, D. Takemori,
3108 T. Ishii, J. Kanzaki, T. Kobayashi, S. Mine, K. Nakamura, K. Nishikawa,
3109 Y. Oyama, A. Sakai, M. Sakuda, O. Sasaki, S. Echigo, M. Kohama,
3110 A. T. Suzuki, T. J. Haines, E. Blaufuss, B. K. Kim, R. Sanford, R. Svo-
3111 boda, M. L. Chen, Z. Conner, J. A. Goodman, G. W. Sullivan, J. Hill,
3112 C. K. Jung, K. Martens, C. Mauger, C. McGrew, E. Sharkey, B. Viren,
3113 C. Yanagisawa, W. Doki, K. Miyano, H. Okazawa, C. Saji, M. Taka-
3114 hata, Y. Nagashima, M. Takita, T. Yamaguchi, M. Yoshida, S. B.
3115 Kim, M. Etoh, K. Fujita, A. Hasegawa, T. Hasegawa, S. Hatakeyama,
3116 T. Iwamoto, M. Koga, T. Maruyama, H. Ogawa, J. Shirai, A. Suzuki,
3117 F. Tsushima, M. Koshiba, M. Nemoto, K. Nishijima, T. Futagami,
3118 Y. Hayato, Y. Kanaya, K. Kaneyuki, Y. Watanabe, D. Kielczewska,
3119 R. A. Doyle, J. S. George, A. L. Stachyra, L. L. Wai, R. J. Wilkes, and
3120 K. K. Young. Evidence for oscillation of atmospheric neutrinos. *Phys.*
3121 *Rev. Lett.*, 81:1562–1567, Aug 1998.
- 3122 [23] Geant4 multiple scattering. [http://geant4.cern.ch/
3123 G4UsersDocuments/UsersGuides/PhysicsReferenceManual/html/
3124 node34.html](http://geant4.cern.ch/G4UsersDocuments/UsersGuides/PhysicsReferenceManual/html/node34.html).
- 3125 [24] Steven Green, John Marshall, Mark Thomson, and Boruo Xu. Cam-
3126 bridge linear collider group - home page. [http://www.hep.phy.cam.
3127 ac.uk/linearcollider/calorimetry/](http://www.hep.phy.cam.ac.uk/linearcollider/calorimetry/).

- 3128 [25] Peter W. Higgs. Broken symmetries and the masses of gauge bosons.
 3129 *Phys. Rev. Lett.*, 13:508–509, Oct 1964.
- 3130 [26] ICFA. Final International Technology Recommendation Panel Report.
 3131 (September), 2004.
- 3132 [27] Ilcsoft homepage. <http://ilcsoft.desy.de>. Accessed: 2010-09-30.
- 3133 [28] IPHC. *MIMOSA26 User Manual*.
- 3134 [29] H Jansen, S Spannagel, J Behr, A Bulgheroni, G Claus, E Corrin, D G
 3135 Cussans, J Dreyling-Eschweiler, D Eckstein, T Eichhorn, M Goffe, I M
 3136 Gregor, D Haas, C Muhl, H Perrey, R Peschke, P Roloff, I Rubinskiy,
 3137 and M Winter. Performance of the EUDET-type beam telescopes.
- 3138 [30] Jérôme Baudot. TAF short manual. 2015.
- 3139 [31] Oleg Kuprash. Power pulsing of the CMOS sensor Mimosa 26. *Nucl.*
 3140 *Instruments Methods Phys. Res. Sect. A Accel. Spectrometers, Detect.*
 3141 *Assoc. Equip.*, 732:519–522, 2013.
- 3142 [32] Lcio homepage. <http://lcio.desy.de>.
- 3143 [33] T. D. Lee and C. N. Yang. Question of Parity Conservation in Weak
 3144 Interactions. *Physical Review*, 104:254–258, October 1956.
- 3145 [34] Yiming Li, Chris Damerell, Rui Gao, Rhorry Gauld, Jaya John John,
 3146 Peter Murray, Andrei Nomerotski, Konstantin Stefanov, Steve Thomas,
 3147 Helena Wilding, and Zhige Zhang. ISIS2: Pixel Sensor with Local
 3148 Charge Storage for ILC Vertex Detector. page 11, jun 2010.
- 3149 [35] Ronald Lipton. Muon Collider: Plans, Progress and Challenges. page 6,
 3150 apr 2012.
- 3151 [36] Cousin Loïc. Trajectométrie dans le cadre du projet européen aida,
 3152 2015.
- 3153 [37] O. Markin. Backgrounds at future linear colliders. feb 2014.
- 3154 [38] A Nomerotski, L Bachynska, J Baudot, N Chon-Sen, G Claus, R De
 3155 Masi, M Deveaux, W Dulinski, R Gauld, M Goffe, J Goldstein, I.-M
 3156 Gregor, Ch Hu-Guo, M Imhoff, U Koetz, W Lau, C Muntz, C Santos,
 3157 C Schrader, M Specht, J Stroth, M Winter, and S Yang. PLUME
 3158 collaboration: Ultra-light ladders for linear collider vertex detector.

- 3159 [39] K. A. Olive et al. Review of Particle Physics. *Chin. Phys.*, C38:090001,
3160 2014.
- 3161 [40] PLUME project. <http://www.iphc.cnrs.fr/PLUME.html>.
- 3162 [41] RH Richter, L Andricek, P Fischer, K Heinzinger, P Lechner, G Lutz,
3163 I Peric, M Reiche, G Schaller, M Schnecke, F Schopper, H Soltau,
3164 L Str uder, J Treis, M Trimpl, J Ulrici, and N Wermes. Design and tech-
3165 nology of DEPFET pixel sensors for linear collider applications. *Nucl.*
3166 *Instruments Methods Phys. Res. A*, 511:250–256, 2003.
- 3167 [42] Maria Robert. Study of the time-dependent cp asymmetry in d^0 decays
3168 in the belle ii experiment, 2015.
- 3169 [43] Adrian Signer. ABC of SUSY. *Journal of Physics G: Nuclear and*
3170 *Particle Physics*, 36(7):073002, jul 2009.
- 3171 [44] The standard model of particle physics. [http://www.brighthub.com/
3172 science/space/articles/84750.aspx](http://www.brighthub.com/science/space/articles/84750.aspx).
- 3173 [45] Junping Tian and Keisuke Fujii. Measurement of Higgs couplings and
3174 self-coupling at the ILC. *Eur. Phys. Soc. Conf. High Energy Phys.*
- 3175 [46] Marc Winter. Development of Swift, High Resolution, Pixel Sensor
3176 Systems for a High Precision Vertex Detector suited to the ILC Running
3177 Conditions. 2009.
- 3178 [47] C. S. Wu, E. Ambler, R. W. Hayward, D. D. Hoppes, and R. P. Hud-
3179 son. Experimental Test of Parity Conservation in Beta Decay. *Physical*
3180 *Review*, 105:1413–1415, February 1957.